Current-Induced Torque Driven Ferromagnetic Resonance in Magnetic Microstructures

Dong Fang

Department of Physics

University of Cambridge

A dissertation submitted for the degree of

Doctor of Philosophy

Downing College, December 2010

Abstract

Current-Induced Torque Driven Ferromagnetic Resonance in Magnetic Microstructures

Dong Fang

This Dissertation explores the interaction between the magnetisation and an alternating current in a uniform ferromagnetic system. Diluted magnetic semiconductors (Ga,Mn)As and (Ga,Mn)(As,P) have been studied. Due to their strong spin-orbit coupling and well-understood band-structure, these materials are well-suited to this investigation. The combined effect of spin-orbit coupling and exchange interaction permits the alternating current to induce an oscillating current-induced torque (CIT) on the magnetisation. In the frequency range close to the natural resonance frequency of the magnetic moments (gigahertz), CIT can excite precessional motion of the magnetisation, a process known as ferromagnetic resonance (FMR).

CIT can be parameterised by an effective magnetic field. By analysing the lineshape of the measured FMR signals, the magnitude and orientation of this effective field have been accurately determined. Moreover, the current-induced fields in these ferromagnetic materials have been observed with symmetries of the Dresselhaus, and for the first time, Rashba spin-orbit coupling. A new class of device-scale FMR technique, named as CIT-FMR, has been established in this Dissertation, with the advantage of simple device structure (only a resistor is required) and scalability (measurements has been performed on devices sized from 4 μm down to 80 nm). This technique is not only limited to magnetic semiconductors, but can also be transferred to study other ferromagnetic systems such as ultrathin metal films.

Finally, the CIT-FMR technique is employed to study the magnetic anisotropy in individual (Ga,Mn)As and (Ga,Mn)(As,P) micro-devices. Devices down to 80 nm in width have been measured in (Ga,Mn)(As,P), which show strong strain-relaxation-induced anisotropy, larger than any previously reported cases on (Ga,Mn)As. Furthermore, due to the tensile-strain on the (Ga,Mn)(As,P) epilayers, the anisotropy field due to patterning-induced strain-relaxation in these devices is observed to take the opposite direction compared to that in the compressively-strained (Ga,Mn)As samples.

Preface

The experimental work presented in this Dissertation was performed under the supervision of Dr. Andrew Ferguson over the period between October 2007 and October 2010 at the Cavendish Laboratory, University of Cambridge, and the Hitachi Cambridge Laboratory, for the awarding of the degree of Doctor of Philosophy.

The research has been funded by the following organisations: Cambridge Overseas Trusts, Hitachi Cambridge Laboratory, Downing College, EU Grant FP7-214499 NAMASTE.

Declaration

This Dissertation is the result of my own work and includes nothing which is the outcome of work done in collaboration except where specifically indicated in the text. It has not been submitted in whole or in part for the award of a degree at this or any other University, and does not exceed 60,000 words in length.

Dong Fang
Downing College, December 2010

To my family

Acknowledgements

The work described in this Dissertation would not have been made possible without the help of many people, directly and indirectly, whether they know it or not. I would like to start by thanking all the people in my life, who have supported me, and have helped me to become the person that I am.

In particular, I first want to thank my supervisor, Andrew Ferguson, for giving me the opportunity to be his student and for mentoring me for the past 3 years. Andrew carries a wealth of knowledge which he enthusiastically shares with his students; I have always enjoyed discussions with him, and the special sensation which I feel after these discussions, knowing that I have learned something new again — I have learned an enormous amount from him in the past few years. On top of this, I also thank Andrew for finding the funds to put so many cool toys in the lab, and putting me in charge of them, and giving me the freedom to explore, learn, and...make mistakes (sorry again about the low-temperature amplifier that I blew up, Andrew!). In all sincerity, I always feel extremely fortunate to spend my graduate career under such a great teacher — I could not have asked for more.

I would also like to thank my workmate Hidekazu Kurebayashi. Over the past one year and a half or so, Hide has always been a source of knowledge and support, and I have always enjoyed the countless conversations that we had on things not just physics-related. On the other hand, I feel bad that Hide has to listen to all my moans (sorry Hide!). Outside the lab, Hide is a good personal friend; and I would like to extend my gratitude to Hide's family — his wife Shoko and their baby girl Mei. It has been a great pleasure watching Mei growing up.

I would also like to extend my appreciation to my colleagues from the Hitachi Cambridge Laboratory. In particular, I want to thank Jörg Wunderlich, who has an enormous amount of knowledge in the field of magnetism and spintronics, and has given me many insightful suggestions over the years. Besides, his passion for science is inspiring to everybody around him. Another special thanks goes to Kai-you Wang, who has now left Cambridge and back in China running his own group. When I first started my PhD, Kai-you helped me solve many practical problems with my experiments, and taught

me how to do 4-point measurements (I really didn't know anything when I started!), how to use the semiconductor parameter analyser, and how to design my devices — I wouldn't have gone anywhere without his help. I would also like to thank the lab manager of HCL, David Williams, for running the lab so that we can freely pursue our experiments, and also for his hospitality for inviting me to his annual house BBQs, which have always been one of the highlights of the year. I also want to thank Elisa De Ranieri, who is two years senior than me, and has always been helpful along the way.

MRC-wise, I would like to thank Henning Sirringhaus for running the group and providing us with such state-of-the-art facilities. Thanks to Radoslav Chakalov for his irreplaceable role in running the clean room, so that we can carry out our device fabrications without worry; well, we still worry about equipments breaking down, but thanks to Radoslav, we just don't have to worry about fixing them. I also want to thank Andrew Irvine, for teaching me the art of lithography, and for always being a source of expertise in nanofabrication. I would also like to extend my appreciation to the supporting staff in the group: Ron Hodierne, who does almost everything from sorting out the mails to fixing the network servers, so that our building doesn't fall apart; the (former) group secretaries Christina Simmons and Melanie Hills, whose workloads may have easily been doubled because of me, when I went on a spending spree with Andrew's funds and made countless purchase orders; and our cleaner Xiu Ping Zhang, who has been a good friend, and has made me delicious lunches.

I also want to thank the supporting staff from around the department. I'd like to specially thank Dan Cross, who has been providing me with two dewars of liquid helium a week for the past two years (it looks as if I drink them!). I also want to thank the guys in the Cavendish Mechanical Workshop: Peter Norman, who always helps me with my designs; Nigel Palfrey, who heads the student workshop and teaches me to use all the big machines in the workshop (it's a shame that I never become good at them); Brian Camps, the welding expert and always nice to chat with; and Adam Brown, who masterly crafted the coldfinger on the dipstick, one of many things he made for me.

Outside Cambridge, I would like to thank Tomas Jungwirth, Karel Výborný, and Liviu Zârbo from the Institute of Physics in Prague, for their contributions to the theoretical side of my work; Richard Campion, Arianna Casiraghi and Bryan Gallagher from the University of Nottingham, for providing us with top-quality wafers.

I would also like to thank Cambridge Overseas Trusts, Hitachi Cambridge Laboratory, and Downing College for financially supporting me during my PhD. We also acknowledge support from EU Grant FP7-214499 NAMASTE.

I could not have survived my days as a graduate student without the support of many good friends. I would like to thank Mijung Lee, for organising many (mostly drinking-related) social events in the office, and for being a wonderful hostess and organising the many more parties outside the office, and more importantly for being a great friend. I'd also like to thank Mijung's daughter Misol, who is at the extremely active age of 4, and has always been a pleasant company in and outside the lab (well of course, she comes into the lab with her mom, not just by herself). Special thanks to my good friends Gueorgui Nikiforov and Sebastian Schoefer, who have been my dinner buddies, movie buddies and travel buddies for the past few years. I also want to thank Shrivalli Bhat, for her wonderful personality and positive attitude in life, which is something I should learn. College-wise, I want to thank Helen Lightfoot and her husband Jörg Sedelmeier, for being my good friends over the past 3 years, and for letting me be the usher in their beautiful wedding (and I really loved the penguin suit!).

Special thanks to my many Chinese friends in and outside the lab (well, some of them are from Taiwan, but we are not too political here, are we?). My special thanks goes to Jui-fen Chang, who is the most hardworking person that I have ever met, and her working attitude is almost legendary. She has been a role model to me, as well as a wonderful friend. I would also like to thank Sam Owen, who started one year earlier than me and introduced me to the life at Cambridge, and has always offered me guidance and help for my work along the way. A big thank you to Jianpu Wang for his hospitality and for welcoming me to his house parties to celebrate every Chinese New Year, which makes life away from home a lot easier to cope with. Along this line I

would like to extend my thanks to Xiulai Xu, Jinjin Wang, Xiaoyang Cheng, Ni Zhao and Chuan Liu, who have made my time at Cambridge simply more enjoyable. I also want to thank my housemates Liang Zhang, Ming Han and Zhi Wang, who have made our house feel like "home", which is the first time I have felt this way since I came to study in England nearly 8 years ago. And they help push me into finishing my PhD, by annoyingly asking me about my progress on writing-up every single day.

My deepest gratitude, however, goes to my parents, who raised and nurtured me, and then (rather unwillingly) let me go to the other side of the world, so that I can have my own space and can freely explore and make my own decisions in life. And they offer guidance instead of constraints, and have supported me and loved me unconditionally along my way. No matter where I am in the world, I would never feel alone; and I love them very much.

Respect.

Contents

1 Introduction **1**

1.1 Diluted magnetic semiconductors 2

1.2 Context of this Thesis 3

1.2.1 Electrical manipulation of the magnetisation 4

1.2.2 Mapping the magnetic anisotropy in individual nano-magnets 8

2 Background **12**

2.1 III–V diluted magnetic semiconductors 12

2.1.1 (Ga,Mn)As and its basic properties 12

2.1.2 Defects in (Ga,Mn)As and their treatment 14

2.2 Magnetic anisotropy 16

2.2.1 Shape anisotropy 17

2.2.2 Magnetocrystalline anisotropy 17

2.2.3 Magnetic anisotropy in (Ga,Mn)As systems 19

2.2.4 Control of magnetic anisotropy 20

2.3 Magneto-transport 24

2.3.1 Anisotropic magnetoresistance 24

2.3.2 Anomalous Hall effect 29

2.4 Magnetisation dynamics 29

2.4.1 Motion of magnetic moments 29

2.4.2 Ferromagnetic resonance 32

2.4.3 Detection of magnetic motion 35

2.5 Spin-orbit interaction in semiconductors 38

3 On-chip driven ferromagnetic resonance on individual (Ga,Mn)As microdevices **42**
3.1 Introduction . . . 42
3.2 Devices and experimental methods . . . 43
3.2.1 Device preparation . . . 43
3.2.2 Measurement apparatus . . . 44
3.2.3 Measurement technique . . . 47
3.3 Data and analysis . . . 50
3.3.1 On-chip FMR using a waveguide . . . 50
3.3.2 Mapping the anisotropy in the nanodevices . . . 55
3.3.3 Vector magnetometry using FMR . . . 58
3.3.4 Effects of annealing . . . 58
3.4 Conclusions . . . 61
3.5 Appendix – Bond pad design . . . 62

4 Ferromagnetic resonance driven by current-induced torque in magnetic microstructures **65**
4.1 Introduction . . . 65
4.2 Devices and experimental methods . . . 66
4.3 Data and analysis . . . 68
4.3.1 Current-induced torque driven FMR . . . 69
4.3.2 Quantifying the current-induced torque . . . 71
4.3.3 Theoretical understanding on the current-induced torque 74
4.3.4 Effect of strain on the current-induced torque . . . 77
4.3.5 Effect of an electrical bias on the FMR signals . . . 80
4.4 Conclusions . . . 82
4.5 Appendices . . . 84
4.5.1 Symmetric Lorentzian component V_{sym} . . . 84
4.5.2 Calibrating the microwave current using Joule heating 87
4.5.3 Vector magnetometry on the (Ga,Mn)(As,P) devices . 87
4.5.4 Magnetic properties of the (Ga,Mn)As microdevices . . 92
4.5.5 Effects of annealing . . . 98
4.5.6 Gating experiments on ultrathin (Ga,Mn)As films . . . 103

5 Mapping the magnetic anisotropy in (Ga,Mn)(As,P) nanostructures 106

5.1 Introduction 106

5.2 Devices and experimental methods 108

5.3 Data and analysis 108

5.3.1 Realisation of FMR in 80 nm-wide devices 108

5.3.2 Mapping the magnetic anisotropy 111

5.3.3 Strain-relaxation in devices of different sizes 112

5.3.4 FMR signatures in devices of different sizes 114

5.3.5 Effects of growth-strain on H_U 116

5.3.6 Lithography-control over the magnetisation 116

5.4 Conclusions and outlook 119

5.5 Appendix – Magnetic anisotropy control with PMMA (preliminary results) 120

6 Closing remarks 128

A Derivation of the FMR lineshape 131

B Measurement apparatus 136

C Lithography recipes for the fabrication of microdevices 140

References 143

Chapter 1

Introduction

The charge and spin of electrons in solid state lay the foundation of today's information technology [1]. Integrated circuits and high-frequency devices, using the charge of electrons in semiconductors, have enjoyed great success in the field of data processing and communications, and have led to products such as computers and mobile phones which are fundamental in today's society. On the other hand, hard drives and magneto-optical disks, utilising the spin of electrons in ferromagnetic materials, have revolutionised the information storage industry, and have allowed knowledge to be spread and passed on not only on papers, but in digital formats with multimedia contents.

But what would happen if both the charge and spin of electrons can be manipulated simultaneously in one device? Spin-based electronics, or "spintronics", is such an emerging technology which exploits the spin states of electrons as well as making use of their charge states. Through the incorporation of spin degree of freedom into conventional charge-based electronics, devices which perform both real-time information processing (logic) and data storage (memory) can be realised, with the advantage of non-volatility, increased processing speed, reduced power consumption, and increased integration densities compared with conventional semiconductor/magnetic material-based electronics [2].

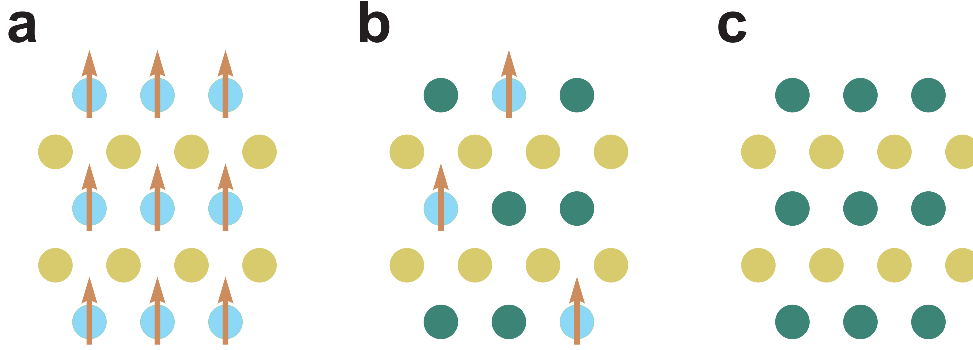

Figure 1.1: Three types of semiconductors, adapted from [1]. **a,** A magnetic semiconductor, in which a periodic array of magnetic elements is present. **b,** A diluted magnetic semiconductor (DMS), an alloy between nonmagnetic semiconductors and magnetic elements (such as manganese). **c,** A nonmagnetic semiconductor, which contains no magnetic moments.

1.1 Diluted magnetic semiconductors

Diluted magnetic semiconductors (DMSs) are created by doping a nonmagnetic semiconductor host with magnetic impurities such as manganese (Figure 1.1). These materials retain their semiconductor properties, such as sensitivity to changes in carrier concentration, and thus can be controlled by electrical gating; in addition, they exhibit ferromagnetic behaviours due to the ordering among the diluted magnetic moments mediated by the charge carriers. Because of this unity of semiconducting and ferromagnetic properties in a single material, DMSs are promising candidates for integrating the functionalities of logic and memory in one device.

Historically, magnetic semiconductors such as europium chalcogenides and semiconducting spinels have been extensively studied in the late 1960s and early 1970s [1]. However, the crystal structures of these materials are different from that of Si or GaAs; furthermore, the growth of these compounds is notoriously difficult [1].

DMSs are first realised in the late 1970s on II–VI semiconductors such as CdTe and ZnTe by doping with Mn. These compounds are relatively easy to

prepare, and the doping can reach very high level. However, because the interaction among the doped magnetic ions is predominantly antiferromagnetic exchange, these materials are usually antiferromagnetic or paramagnetic [1]. Only in the late 1990s carrier-induced ferromagnetic transition in (Cd,Mn)Te has been shown, but only at very low temperatures (T = 1.8 K) [3]. This renders these materials less attractive for applications.

The most widely studied DMS to date is the III–V group magnetic semiconductor (Ga,Mn)As, which is first successfully synthesised in 1996 [4]. Since the host semiconductor GaAs is already being used in a wide range of applications, including mobile phones (microwave transistors) and compact-disks (semiconductor lasers), there is little doubt that adding ferromagnetism would open up a wide range of new applications. In particular, the magnetisation in (Ga,Mn)As has been observed to respond to strain [5–8], electrical gating [9–12] and light [13–16], making it possible for nonmagnetic manipulation of (Ga,Mn)As nanomagnets.

1.2 Context of this Thesis

In modern computers, logic operations are performed by manipulating the charges in semiconductor devices, hence they require continuous supply of electric currents. Whereas memory operations are achieved by controlling the magnetisation orientation in nanoscale ferromagnets using a magnetic field, which is generated by a current-carrying coil (Ampère's circuital law). The magnetic memory media have the advantage of being non-volatile; however, generating a magnetic field using an electric current is a slow and energy consuming process, and this has prevented real-time information processing from being carried out in ferromagnetic devices. Moreover, the magnetic field is difficult to localise, incompatible with the downscale of magnetic elements required for achieving higher storage density.

One of the major quests in spintronics research is to find ways to manipulate the magnetisation direction in a ferromagnet without the use of an external magnetic field. Such technology would integrate the best qualities of two disparate worlds: the impressive computing power of semiconductor

logic, and the unparallel storage capacity of magnetic memory. In this Thesis, two of the fundamental issues concerning future spintronic devices are addressed, which are related to the *manipulation* and the *stability* of the magnetisation in a nanoscale ferromagnet. The experiments in this Thesis are based on III–V diluted magnetic semiconductors.

1.2.1 Electrical manipulation of the magnetisation

A big achievement towards this goal has been the discovery of spin-transfer torque (STT) [17–19], which occurs when spin-polarised currents traverse in non-collinear magnetic systems[1]. STT has been intensively studied for the past 10 years, and has been exploited to achieve current-induced magnetisation reversal [20–23] and current-induced domain-wall motion [24–27] in submicron ferromagnets. These discoveries could lead to important data storage devices, such as magnetic random access memory (MRAM) [28, 29] and racetrack memory [30, 31].

In addition, STT has been employed to drive the magnetisation into precessional motion [23, 32, 33], which could lead to novel microwave sources and resonators. Moreover, a ferromagnetic resonance (FMR) technique based on STT has also been demonstrated [34, 35], which allows characterisation on the magnetic properties of the nanomagnets. Figure 1.2 illustrates the concept of STT in a spin-valve structure.

However, what happens when a current travels through a *uniform* ferromagnetic system? Although non-collinear systems could give rise to STT, uniform ferromagnets are more favourable for applications because of their simple device structures. Recent theoretical work [37–40] suggests that spin-torque effects could also be intrinsic to ferromagnetic materials. This leads to the case of "current-induced torque" (CIT), which appears in uniform ferromagnets and provides a radically new mechanism for the manipulation of the magnetisation in these devices.

[1] A non-collinear magnetic system contains structures such as spin-valves, magnetic tunnel junctions (MTJs), or domain walls.

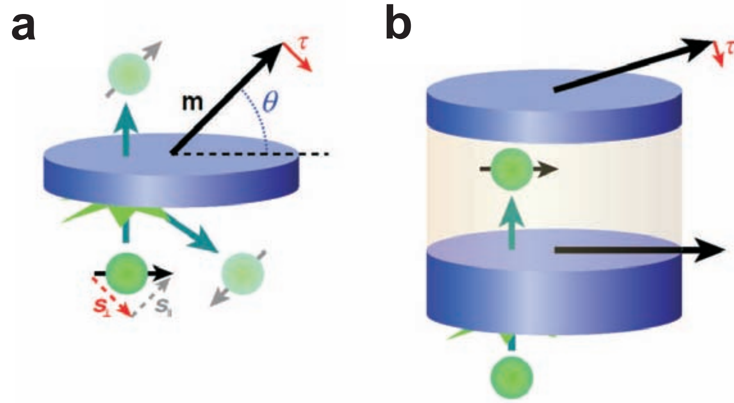

Figure 1.2: An illustration of the spin-transfer torque effect in spin-valve device structures, adapted from [36]. **a,** A single magnetic layer with a spin-polarised electron passing through it. The magnet transmits and scatters the collinear component of the spin ($s_{\parallel}$) and absorbs the transverse component ($s_{\perp}$). The angular momentum of the transverse spin $s_{\perp}$ is therefore transferred to the magnetic moments **m** in the layer and causes them to precess. **b,** The spin-polarised electrons are created when an electric current passes through the pinned layer of a spin-valve, which can then act on the magnetisation in the free layer.

The current-induced torque in uniform ferromagnets has its origin in two quantum mechanical effects: the spin-orbit interaction resulting from special relativity, and the exchange interaction between carrier spins and magnetic moments.

When a current passes through materials lacking inversion symmetry, a non-equilibrium accumulation of spins occurs due to the relativistic spin-orbit coupling. This phenomenon is called "current-induced spin polarisation" and has been observed in several nonmagnetic semiconductor devices [41–43]. Furthermore, theoretical work has pointed out that band-structure effects in semiconductors cause spin-orbit coupling to act like an effective magnetic field [44, 45], which in turn can affect the electron spins [46–49]. For example, it has been experimentally demonstrated that the oscillating effective magnetic field resulting from an oscillating current can resonantly drive the precessional motion of spins, and create electron spin resonance (ESR) in 2-dimensional electron gases (2DEG)[1] or semiconductor quantum wells [50–54]. In addition, static current-induced effective magnetic fields have also been experimentally confirmed in semiconductor heterostructures [55, 56], quantum wells [57], ultrathin metal layers [58, 59] and the interface between insulating oxides [60].

The above theoretical and experimental studies mostly focus on the current-induced spin polarisation in nonmagnetic materials. When this effect occurs in a ferromagnet, the effective magnetic field then combines with the s–d exchange interaction, which couples the conduction electron spins to the magnetisation. As a result, a current passing through a uniformly magnetised ferromagnetic layer would exert an exchange-mediated effective field on the magnetisation, thereby producing a torque, as illustrated in Figure 1.3. This current-induced torque therefore provides direct electrical means for manipulating the magnetisation in nanomagnets.

[1] To be more precise, this type of resonance experiment is referred to as "electrical dipole spin resonance" (EDSR). Since the conventional spin resonance transitions (such as in ESR) are usually from magnetic dipole transitions, whereas under the influence of spin-orbit coupling, electrical dipole transitions are allowed [50].

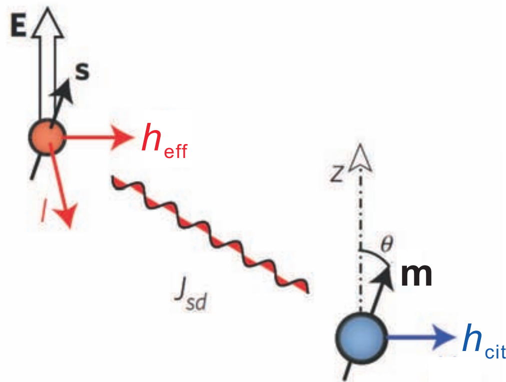

Figure 1.3: Microscopic origin of the s–d-mediated current-induced torque, adapted from [58]. Conduction electrons moving perpendicular to an electrical field **E** have their spin (**s**) tilted by the effective magnetic field ($\mathbf{h}_{\text{eff}}$), exerting a torque on the localised moments (**m**) through the exchange coupling (J_{sd}). This current-induced torque can be parameterised by a magnetic field $\mathbf{h}_{\text{cit}}$.

The first experimental demonstration of CIT-induced magnetisation reversal is reported in 2009 by Chernyshov *et al.* [39]. The model ferromagnetic semiconductor (Ga,Mn)As has been chosen for their experiment, because of its strongly spin-orbit-coupled band-structure [61]. In their experiment, the magnetisation switching behaviour in a disk-shaped device is altered by the application of a large direct current (±0.7 mA); moreover, this alteration is asymmetric and depends on the direction of the current with respect to the crystal axes, both pointing to the existence of the current-induced torque. Similar magnetisation reversal experiments have since been reported in 2010 on ultrathin ferromagnetic metals Pt/Co/AlO$_x$ [58, 59], in which the current-induced field is observed to be $\sim$ 20 times larger than that in (Ga,Mn)As [58].

Although CIT in ferromagnetic materials has been demonstrated in magnetisation reversal experiments, there has been no study on its effect on the dynamics of the magnetic motion, in contrast to the large number of ESR experiments in nonmagnetic semiconductors using an oscillating effec-

tive magnetic field [50–54], and the systematic studies of the magnetisation dynamics under the influence of STT [23, 32–35, 62, 63].

The main focus of this Thesis is the CIT-FMR experiment described in Chapter 4. It is the first experimental demonstration of an oscillating current-induced torque in ferromagnetic systems. FMR in microstructures patterned on magnetic semiconductors (Ga,Mn)As and (Ga,Mn)(As,P) are driven by a microwave frequency CIT, and coherent magnetic motion is detected electrically using a frequency mixing effect. By analysing the FMR lineshape, the magnitude and orientation of the current-induced effective field $\mathbf{h}_{\mathrm{cit}}$ have been determined with unprecedented accuracy (within 5 μT). Moreover, the effective field has been observed with signatures from different types of spin-orbit interactions (Dresselhaus and Rashba), which cannot be distinguished in the magnetisation switching experiments [39, 64].

Further measurements also reveal that depending on whether the epilayer is compressively or tensile-strained, the directions of the CIT fields change sign. And the strength of the CIT fields can also be influenced by changes in the carrier concentration (by varying Mn doping levels). In addition, as the structures are made even smaller, significant strain-relaxation occurs which reduces the magnitude of $\mathbf{h}_{\mathrm{cit}}$. These observations suggest possible methods for customising the spin-orbit coupling in future spintronic devices.

1.2.2 Mapping the magnetic anisotropy in individual nanomagnets

In modern data storage media, the digital information, encoded as 0s and 1s in binary format, is represented by the orientations of the magnetisation in nanomagnets. The magnetic anisotropy determines the stable directions of the magnetisation as well as the energy barrier that confines it. Therefore it is vital for magnetic memory units to have well-defined anisotropy, so that the binary information can be unambiguously defined, and is able to withstand the thermal fluctuations in the memory units' operational environment. Furthermore, it would be highly beneficial to be able to engineer the magnetic anisotropy to serve the application needs.

Patterning magnetic materials into nanoscale devices provides a controllable way to modify the magnetic anisotropy. For example, in magnetic metals, device patterning produces the shape anisotropy, which becomes important for devices with size less than a few microns. In DMSs, the magnetocrystalline anisotropy is strain-related, and this is greatly modified in nanoscale devices due to the strain-relaxation effect [26, 65–67].

Ferromagnetic resonance (FMR) spectroscopy is a long-standing technique for characterising magnetic systems. It has been applied since 1950s to many metallic materials (for reviews, see Ref. [68–70]) and has now been extended to the study of diluted magnetic semiconductors such as (Ga,Mn)As and (Ga,Mn)(As,P) [71–77]. Among the parameters which can be learned with this technique are the magnetocrystalline anisotropy constants, the g-factor, the Gilbert damping factor, the spin stiffness (via spin wave excitation detection), and even the homogeneity of the magnetic films [78].

So far FMR-based studies on the magnetic anisotropy in (Ga,Mn)As have focused on whole wafers, and only one publication has been on the properties of individual submicron devices [67]. This is because the conventional FMR spectroscopy lacks the sensitivity to detect the magnetic motion in small devices[1]. However being able to employ the power of FMR spectroscopy in the study of individual magnetic micro- and nanostructures is highly desirable.

Several different approaches to device-scale FMR have recently been introduced. A combination of microwave excitation and local detection is required. The excitation by a microwave magnetic field can be performed in a standard cavity [79] or a waveguide [80–82]. Alternatively a local excitation technique can be employed, for example using a current-carrying waveguide closely aligned to the magnetic nanostructure [83–87]. In addition, for samples in a spin-valve geometry, the spin-transfer torque can be used to drive the magnetisation [34, 35, 63]. Device-level detection of FMR can be achieved

[1]The magnetic anisotropy can also be determined by measuring the saturation magnetisation along different crystalline axes using a superconducting quantum interference device (SQUID). However, this technique also suffers from sensitivity issues when measuring small structures.

electrically by a frequency mixing effect based on the anisotropic magnetoresistance (AMR) [79–81, 83–87] or tunnelling magnetoresistance (TMR) [34, 63], which allows the sample itself to be the detector (see Section 2.4.3 for details). Furthermore, magnetisation precession can be detected using focused magneto-optical effects or x-rays [67, 88]. As well as these device-level measurements of FMR, scanning probe FMR techniques based on magnetic force microscopy are available [89], allowing spatial variations of magnetic anisotropy to be mapped within materials.

In Chapter 3, an all-electrical, on-chip driven FMR experiment on submicron (Ga,Mn)As stripes is described, using a method similar to that used by Costache *et al.* [83, 84]. With this technique, the magnetisation of the ferromagnet is driven by a local microwave magnetic field, which is generated electrically by a waveguide placed next to the device. The magnetic motion is also detected electrically by utilising the frequency mixing effect. The magnetic anisotropy data measured on these nano-bars corroborate the published results by Hoffmann *et al.* [67], who have employed an electrically-driven, optically-detected FMR setup. In addition, analysis on the FMR lineshape allows one to determine the orientation of the microwave excitation field, and this proves to be crucial to the understanding of the CIT-FMR experiments.

The CIT-FMR technique, established in Chapter 4, is a highly scalable method for the characterisation of individual ferromagnetic microstructures. Moreover, since the magnetisation is driven by the microwave frequency CIT which appears inside the device, no additional waveguide structure is required, greatly simplifying the fabrication process (only a rectangular mesa structure with bond pads is needed). The magnetic anisotropy in the (Ga,Mn)As micro- and nano-devices are characterised using CIT-FMR (given in Chapter 4.5.4), and the observations are consistent with earlier studies using SQUID and magneto-transport measurements [26, 65, 66].

Besides (Ga,Mn)As, a newly synthesised III–V group ferromagnetic semiconductor (Ga,Mn)(As,P) has drawn research interests in the field of semiconductor spintronics [77, 90–94]. Because of the crystal structure, the (Ga,Mn)(As,P) epilayers can be grown under tensile-strain [77], different

from the majority of the (Ga,Mn)As wafers being studied which are under compressive-strain [1, 95]. However, so far there has been no study on the magnetic properties of nano-devices patterned on (Ga,Mn)(As,P).

In Chapter 5, CIT-FMR is employed to investigate the magnetic anisotropy in individual (Ga,Mn)(As,P) micro- and nanostructures for the first time. It has been observed that the patterning-induced strain-relaxation has the reverse effect on the magnetic anisotropy in these samples, compared with (Ga,Mn)As devices under compressive-strain [26, 65–67].

Chapter 2

Background

This Thesis explores the dynamic behaviour of the magnetisation under the influence of a driving torque oscillating at frequencies close to the magnetisation's natural resonance frequency. The experiments have been performed on the diluted magnetic semiconductors (Ga,Mn)As and (Ga,Mn)(As,P) and their characteristics are introduced in Section 2.1. A property related to all ferromagnetic materials, the magnetic anisotropy, is then discussed in Section 2.2.

Methods for characterising ferromagnetic systems include dc transport measurements and magnetisation dynamics analysis, which are reviewed in Sections 2.3 and 2.4, respectively. Finally, the effect of spin-orbit coupling in semiconductors is introduced in Section 2.5.

2.1 III–V diluted magnetic semiconductors

2.1.1 (Ga,Mn)As and its basic properties

(Ga,Mn)As is created by doping the host GaAs with Mn during the crystal growth. In order to reach the high concentrations of Mn ions required for creating ferromagnetism in these materials ($\sim 1\%$), the crystal growth condition has to be driven away from its equilibrium temperature, using a so-called low-temperature molecular-beam-epitaxy technique (LT-MBE) [95].

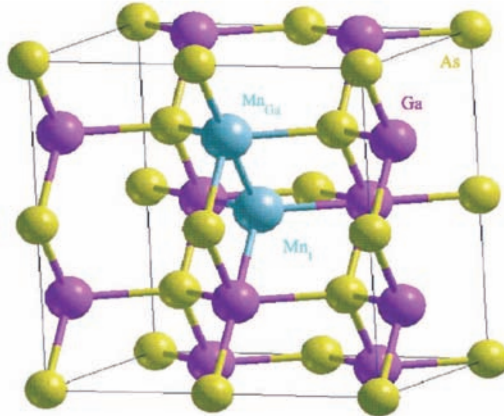

Figure 2.1: (Ga,Mn)As lattice with Mn atoms in substitutional (Mn_{Ga}) and interstitial (Mn_I) positions, adapted from [61]. The latter is a common type of defects in (Ga,Mn)As epilayers.

X-ray diffraction experiments reveal that the (Ga,Mn)As crystal has a zinc-blende structure, much like its GaAs host (Figure 2.1). This is because when Mn dopants are introduced in the crystal growth process, they tend to occupy substitutional positions at cation sites and participate in crystal bonding with As similar to the substituted Ga atoms. Substitutional Mn_{Ga} atoms provide local magnetic moments with zero angular momentum and spin $s = 5/2$. Because of the missing valence $4p$ electron, the Mn_{Ga} atoms act as acceptors providing one hole per ion [61].

In the absence of holes, the magnetic interaction among Mn has been shown to be antiferromagnetic in fully carrier compensated (Ga,Mn)As [1], which indicates that the ferromagnetic order is hole-induced. The doping level of Mn ions is extremely important, and it has been observed experimentally that ferromagnetism arises when the concentration of Mn reaches $\sim 1\%$ [96], and the system is near the Mott insulator-to-metal transition[1] [61]. At these large Mn concentrations, the localisation length of impurity-band

[1]The Mott insulator-to-metal transition happens when r_c, the average distance between Mn impurities (or between holes bound to the Mn ions), is comparable in size to the impurity effective Bohr radius $a^* = E\hbar/(m^* e^2)$, where m^* is the effective mass near the top of the valence band [61].

states is extended to a degree that allows them to mediate ferromagnetic exchange interaction between Mn moments, even though the moments are dilute.

2.1.2 Defects in (Ga,Mn)As and their treatment

The non-equilibrium growth of (Ga,Mn)As epilayers by LT-MBE causes a substantial number of meta-stable impurity states to form. Two common types of defects are Mn ions occupying the tetrahedral interstitial sites (Mn_I) rather than the substitutional Ga sites (see Figure 2.1), and As atoms on cation sites (As_{Ga}, antisite defects). The number of such unintended defects increases with higher Mn doping because of the tendency of the material towards self-compensation, even under non-equilibrium growth conditions [61]. Both impurities act as donors and can have severe impact on the electrical and magnetic properties of the ferromagnetic films. For example, the interstitial Mn_I ions contribute to local moment compensation, and cause structural changes in the crystal; whereas the antisite As_{Ga} atoms can result in hole compensation [61].

These defects, especially the interstitial Mn_I atoms, can be removed by post-growth annealing. Early studies indicate that annealing at temperatures $\sim$ 400°C reduces the number of electrically and magnetically active ions in the (Ga,Mn)As layer [97]. However, it is later found that annealing at temperatures close to the growth temperature ($\sim$ 200°C) results in the removal of Mn_I ions by out-diffusion and passivation at the sample surface, and leads to an increase in the conductivity and Curie temperature T_C of the ferromagnet film [11, 98–101]. The effect of annealing is more pronounced in (Ga,Mn)As wafers with more interstitial Mn_I ions, i.e. with higher Mn doping.

Figure 2.2a shows the effect of annealing on the magnetisation[1] M and resistivity ρ of a (Ga,Mn)As sample [100]. Temperature-dependent measurement on the spontaneous magnetisation M using superconducting quantum interference device (SQUID) demonstrates that for the as-grown sample, M

[1] M represents the magnitude of the magnetisation vector $\mathbf{M}$ in a system, i.e. $M = |\mathbf{M}|$.

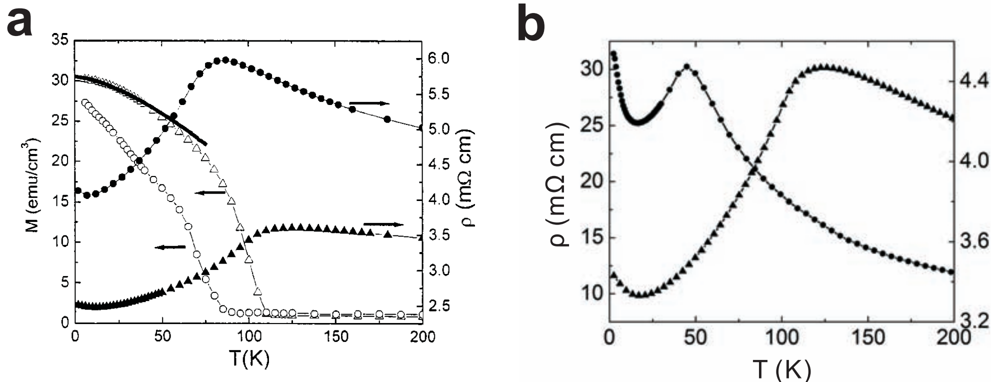

Figure 2.2: The effect of annealing on the Curie temperature of (Ga,Mn)As and (Ga,Mn)(As,P) films. **a,** The magnetisation and resistivity as a function of temperature for a (Ga_{1-x},Mn_x)As sample with $x = 0.0597$ (circles, as-grown; triangles, annealed), adapted from [100]. **b,** The temperature-dependent resistivity measured on a ($Ga_{0.94}$,$Mn_{0.06}$)($As_{0.9}$,$P_{0.1}$) sample.

vanishes for temperatures above ~ 75 K; while after being annealed at 250°C for 2 h, this temperature rises to 110 K [99]. The resistivity of the sample ρ is also found to be lowered in the annealed sample.

Figure 2.2a also demonstrates that there exists a correlation between the resistivity ρ of the (Ga,Mn)As sample and its temperature T. This can be understood as a result of the competition between the increase in phonon energy and decrease in ferromagnetic order as the sample temperature is raised. It has been confirmed that the origin of the broad peak seen in the $\rho(T)$ curve is due to a singular behaviour as $T \to T_C^+$ [102], and this singularity can be found by differentiating ρ with respect to T. It is observed in SQUID measurements that the singularity in $\partial\rho/\partial T$ coincides with T_C, especially in annealed, defect-free samples [102]. This is particularly useful for determining T_C in patterned samples, whose small dimensions usually prevent their magnetisation from being directly measured by SQUID.

In another magnetic semiconductor (Ga,Mn)(As,P), post-growth annealing treatment becomes more crucial. It has been found that the as-grown (Ga,Mn)(As,P) epilayers exhibit low T_C (below 30 K) and are electrically in-

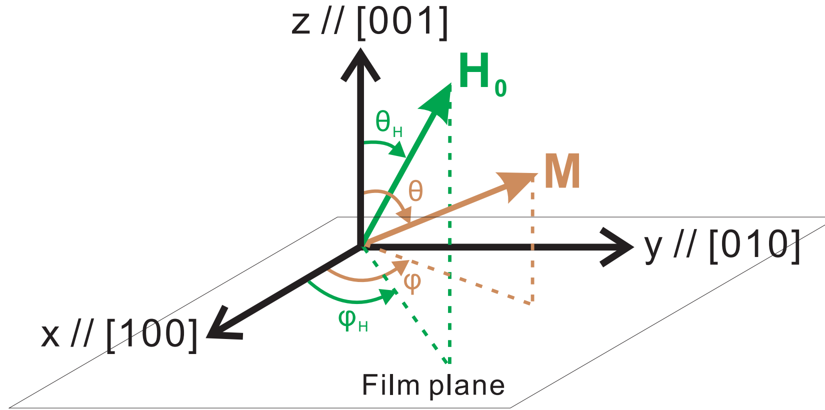

Figure 2.3: The coordinate system used for defining the magnetic anisotropy energies. Here $\mathbf{H}_0$ is the external magnetic field, and $\mathbf{M}$ is the magnetisation vector in the system.

sulating at low temperatures, both pointing towards high degrees of carrier compensation in these wafers [92]. After annealing at 180°C for 48 h, the conductivity at low temperatures dramatically increases and T_C rises above 100 K, as illustrated in Figure 2.2b: The resistivity ρ at 6 K drops by 8 times in the annealed sample, accompanied by the recovery of T_C.

2.2 Magnetic anisotropy

Magnetic anisotropy describes the preference for the magnetisation to lie in a particular direction with respect to crystallographic axes in a sample. An energy term of this kind is referred to as the magnetic anisotropy energy. In ferromagnetic semiconductors, the anisotropy can be caused by sample shape, crystalline symmetry and stress. Figure 2.3 defines a coordinate system used for describing the various anisotropy energies.

A quantitative measure of the strength of the magnetic anisotropy is the field H_i needed to saturate the magnetisation in a hard direction, and H_i is called the "anisotropy field". The anisotropy energy per unit volume (i.e. energy density) needed to saturate a magnetic material in a particular

direction is given by the following generalised equation [103]:

$$K_i = \mu_0 \int_0^{M_s} H(M)dM \xrightarrow{\text{1st order}} \mu_0 \frac{M_s H_i}{2} \tag{2.1}$$

Here M_s is the saturation magnetisation, and K_i has the unit of J/m^3. The concept of the anisotropy field H_i and its linear relation to the anisotropy energy density K_i are used throughout this Thesis.

2.2.1 Shape anisotropy

The shape anisotropy, also called magnetic dipolar anisotropy, describes the relation between the demagnetisation energy and the shape of a sample. It is caused by the long-range magnetic dipolar interactions. In a thin magnetic film, the magnetic energy density due to shape anisotropy can be written as [104]:

$$E_S = \frac{1}{2}\mu_0 M_s^2 \cos^2\theta \tag{2.2}$$

Equation 2.2 suggests that in-plane alignment of magnetic moments usually prevails in ferromagnetic thin films (i.e. $\theta = 90°$) as it leads to a lower energy state. However, for DMSs such as (Ga,Mn)As and (Ga,Mn)(As,P), perpendicular-to-plane magnetic orders have also been reported [1, 92], due to the much stronger strain-dependent magnetocrystalline anisotropy present in these materials.

2.2.2 Magnetocrystalline anisotropy

Besides the shape anisotropy, the direction of the spontaneous magnetisation in ferromagnetic systems also has preference over particular crystalline axes. This is described as the magnetocrystalline anisotropy. Two common types are the uniaxial and cubic anisotropy, with the latter sometimes referred to as biaxial anisotropy in epitaxially-grown (Ga,Mn)As and (Ga,Mn)(As,P) films.

Uniaxial anisotropy The preference of the magnetisation in a ferromagnet over a single axis is described by the uniaxial anisotropy. The energy in a system with uniaxial anisotropy is minimised when the magnetisation lies along the easy axis. For example, cobalt is a hexagonal crystal and the hexagonal axis (z-direction in Figure 2.3) is the direction of easy magnetisation. The uniaxial anisotropy energy density in cobalt (E_U) can be described by a power series [105]:

$$E_U = K_{U0} + K_{U1}\sin^2\theta + K_{U2}\sin^4\theta + K_{U3}\sin^6\theta + \dots \tag{2.3}$$

where K_{Ui} are uniaxial anisotropy energy constants. Note that K_{U0} does not carry any anisotropy properties as it is independent of the orientation of the magnetisation. $K_{U1} > 0$ indicates that the easy axis is along the hexagonal axis. Careful analysis of the magnetisation orientation curves indicates that for most purposes, it is sufficient to keep only terms up to K_{U2} [103].

Cubic anisotropy In a cubic system, such as iron, the cubic edges define the directions of easy magnetisation. There is an additional energy cost if the sample is magnetised in an arbitrary direction. The energy density associated with this, referred to as the cubic anisotropy (E_C), is described by powers of the the direction cosines of $\mathbf{M}$ along the three cubic edges (α_1, α_2, α_3). Due the the high symmetry of cubic crystals, a low-order approximation of E_C is [103]:

$$E_C = K_{C0} + K_{C1}\left(\alpha_1^2\alpha_2^2 + \alpha_2^2\alpha_3^2 + \alpha_3^2\alpha_1^2\right) + K_{C2}\left(\alpha_1^2\alpha_2^2\alpha_3^2\right) + \cdots \tag{2.4}$$

Here $\alpha_i = M_i/M_s$. It is known from experiments that higher order terms in Equation 2.4, in most cases even the K_{C2} term, are negligible [106].

When $K_{C1} > 0$, such as in Fe and Co, the first term in Equation 2.4 becomes minimum in the [100] direction, indicating that this is the magnetic easy axis; whereas for $K_{C1} < 0$, such as in Ni, the easy axis is along the [111] direction. Using the trigonometric functions of spherical coordinates (θ, φ), the coefficient of K_{C1} in Equation 2.4 reduces to [103]:

$$\sin^4\theta\cos^2\varphi\sin^2\varphi + \cos^2\theta\sin^2\theta = \frac{1}{4}(\sin^4\theta\sin^2 2\varphi + \sin^2 2\theta) \tag{2.5}$$

2.2.3 Magnetic anisotropy in (Ga,Mn)As systems

The magnetocrystalline anisotropy of bulk (Ga,Mn)As is cubic due to its zinc-blende structure [107]. The magnetic easy axes are along the three symmetrically equivalent <100> or <111> crystal directions. However, the pure bulk properties do not apply to the epitaxially-grown wafers, in which the substrate plays an important role in defining the magnetic anisotropy. In particular, the vast majority of work has been done on (Ga,Mn)As films grown on [001]-oriented substrates, and their properties are the focus of this Section.

The (Ga,Mn)As epilayers are strained in the growth direction as a result of lattice mismatch and exhibit an additional perpendicular-to-plane anisotropy. For example, for a (Ga,Mn)As film grown on a substrate with a smaller lattice constant (such as GaAs), lattice mismatch causes the ferromagnetic layer to be compressively-strained, leading to uniaxial anisotropy with an in-plane easy axis [95]. Whereas when a InGaAs buffer layer is used which has a larger lattice constant than (Ga,Mn)As, the magnetic film grown on it is tensile-strained and has a perpendicular-to-plane easy axis [1]. More recently, it has been demonstrated that by the incorporation of phosphorus atoms at the As sites, the resulting (Ga,Mn)(As,P) epilayers can become tensile-strained for P concentrations higher than 6%, leading to a perpendicular-to-plane easy axis [77, 92–94].

The in-plane anisotropy of compressively-strained (Ga,Mn)As layers is dominated by the competition between the biaxial anisotropy along the cubic edges[1] and the uniaxial anisotropy with easy axis along either the $[1\bar{1}0]$ or [110] directions [107]. In some materials an additional uniaxial anisotropy along [010] is also observed [108]. The anisotropy energies are temperature-dependent: The biaxial anisotropy scales with the magnetisation as M^4, while the uniaxial anisotropy scales as M^2. As the temperature approaches T_C and M decreases, the dominant anisotropy term changes from biaxial to uniaxial [109]. It has also been observed that low temperature annealing

[1] For (Ga,Mn)As epilayers grown on [001]-oriented GaAs substrates, the biaxial anisotropy leads to magnetic easy axes along the [100] and [010] directions.

(190°C) causes the easy axis of the uniaxial anisotropy to rotate from $[1\bar{1}0]$ to [110] direction [110].

The magnetic anisotropy can be characterised by measuring the remanent magnetisation along various crystalline orientations using SQUID. Alternatively, it can be inferred from magneto-transport measurements (see Section 2.3), from magneto-optical experiments [111], or from FMR spectroscopy (see Section 2.4).

2.2.4 Control of magnetic anisotropy

It is important from an application perspective to be able to manipulate the magnetic anisotropy, and therefore the direction of the magnetisation, of a ferromagnetic device via a *nonmagnetic* parameter. The change in magnetic anisotropy caused by lattice mismatch during the crystal growth phase, described in the previous Section, cannot satisfy the need of a spintronic device in an operational environment. Several different approaches towards device-scale control of magnetic anisotropy is reviewed in this Section.

From the large impact of growth-induced strain on the magnetocrystalline anisotropy, it is conceivable that adding mechanical strain via a piezoelectric transducer can achieve electrical control of the magnetic anisotropy in (Ga,Mn)As devices. This has been experimentally demonstrated: Upon the application of a high voltage (~ 150 V), the mechanical strain generated by a piezoelectric transducer is enough to cause rotation of the magnetisation in a (Ga,Mn)As sample attached to it [5–8]. Figure 2.4 demonstrates the effect of mechanical stress on the magnetisation switching curves measured on a (Ga,Mn)As device [7].

Since the ferromagnetism in (Ga,Mn)As is carrier-mediated, it is therefore expected that by changing the carrier (hole) concentration, the magnetic anisotropy can also be affected. Although (Ga,Mn)As behaves like a dirty metal at Mn concentrations of a few percent, the carrier density in these

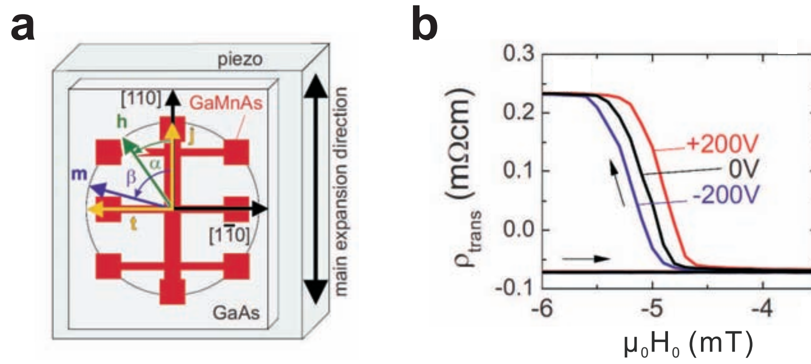

Figure 2.4: Magnetisation control using a piezoelectric transducer, adapted from [7]. **a,** Schematic of the experimental setup. The (Ga,Mn)As device is patterned into a Hall bar for transport measurements (see Section 2.3). **b,** Transverse AMR measured across the device while the external field $\mathbf{H}_0$ is swept. The curves are shifted by charging the transducer.

materials is usually 2 – 3 orders of magnitude lower than in metals[1], making them suitable for electrical gating. These experiments are first performed on (In,Mn)As and (Ga,Mn)As samples using a metal-insulator-semiconductor device structure (i.e. a field-effect transistor, or FET) [9, 10, 112, 114]. The application of an electric field causes hole depletion/accumulation in the magnetic semiconductor, changing its anisotropy and rotating the direction of the magnetisation. Furthermore, sizeable carrier change in (Ga,Mn)As with a moderate electric field has also been demonstrated in an all-semiconductor FET device, with a n-type, highly Si-doped GaAs layer acting as the gate electrode [11, 12]. Figure 2.5 demonstrates the effect of gating on a (In,Mn)As FET device [112].

The above two methods are in principle compatible with both whole wafers and individual devices. In addition, it is also noticed that in patterned (Ga,Mn)As devices, the lithographically-defined edges allow the lattice to

[1]In (Ga,Mn)As with Mn doping of a few percent, the atomic concentration of Mn is in the order of $n_{\mathrm{Mn}} \sim 10^{19} - 10^{21}$ cm^{-3} (1% of Mn corresponds to n_{Mn} of 2.2×10^{20} cm^{-3}), and the hole density is $p \sim 10^{18} - 10^{20}$ cm^{-3}. Note that n_{Mn} and p are not the same because of carrier compensation. In metals the charge density is usually 10^{22} cm^{-3} [113].

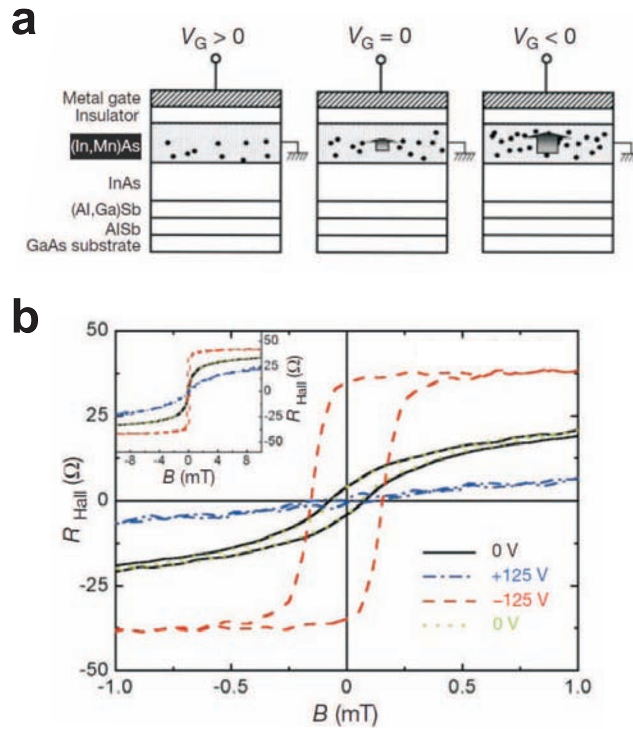

Figure 2.5: Field-effect control of the hole-induced ferromagnetism in a (In,Mn)As FET, adapted from [112]. **a,** Schematic of the role of electrical gating on the change in carrier concentration in (In,Mn)As. The arrows schematically show the magnitude of the magnetisation. **b,** The Hall resistance R_{Hall} (see Section 2.3.2) across the device under different gate biases. Application of $V_G = 0$, $+125$ and -125 V results in qualitatively different field dependence of R_{Hall}. Inset: The same curves shown at higher magnetic fields.

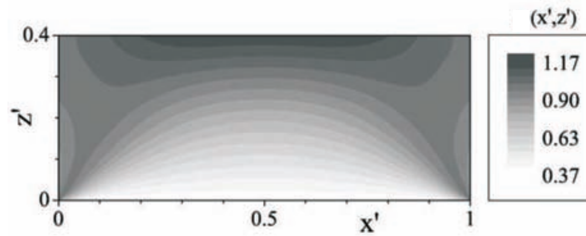

Figure 2.6: Simulation results of the spatial dependence of the strain coefficient ξ due to lattice-relaxation in a narrow bar with thickness $\div$ width $=$ 0.4 and compressive growth-strain, adapted from [115].

partially relax and thus reduce the total strain on the sample. Numerical simulations have shown that this effect occurs over a length scale of a few hundred nm [26, 66, 115], and magneto-optical Kerr microscopy has provided direct observations [67]. In bar-shaped (Ga,Mn)As samples, patterning-induced strain-relaxation introduces an additional uniaxial anisotropy, with easy axis perpendicular to the direction of strain-relaxation (i.e. along the long axis of the bar). In micrometre-wide devices, this additional anisotropy can act to rotate the magnetic easy axes from their as-grown positions [26]; in very narrow bars (submicron), this anisotropy becomes more pronounced and has been demonstrated to dominate over the intrinsic anisotropy energies, over all temperatures up to T_C [65, 67]. Figure 2.6 shows the simulation results of strain-relaxation in a compressively-strained (Ga,Mn)As stripe [115].

So far the influence of strain-relaxation on the magnetic anisotropy has only been investigated on compressively-strained (Ga,Mn)As devices. In Chapter 5, FMR experiments on individual tensile-strained (Ga,Mn)(As,P) nano-bars confirm that the growth-strain has a major impact on the strain-relaxation-induced anisotropy, leading to reversal of its easy axis.

2.3 Magneto-transport

Magneto-transport in ferromagnetic systems can be broken down into ordinary effects depending on the applied magnetic field alone, which arise from the Lorentz force acting on the charge carriers; and extraordinary effects which depends on the relative orientations between the magnetisation and the current, and originate from the spin-orbit and exchange interactions.

Two important transport effects are introduced in this Section, namely the anisotropic magnetoresistance (AMR) and the anomalous Hall effect (AHE). Their measurements provide means to detect the direction of the magnetisation vector **M**, to measure the magnitude of the magnetic field required for switching **M** from one easy axis to another (switching field), and to quantify the magnetic anisotropy constants.

Figure 2.7a sketches a Hall bar structure which is commonly used for four-probe transport measurement of AMR and AHE: While the current flows from 8 to 4, the longitudinal and transverse voltages V_{xx} and V_{xy} are measured. This allows the respective resistivity ρ_{xx} and ρ_{xy} to be calculated. Alternatively, two-probe measurement (using only contacts 8 and 4) is also commonly performed for determining the longitudinal resistivity ρ_{xx}, provided that resistance from the contacts is not important. Figure 2.7b shows a variation of the two-probe measurement, in which the current flows radially from the central contact to the edge in all directions (a Corbino disk structure). This removes the crystalline effect from the transport measurement results.

2.3.1 Anisotropic magnetoresistance

The phenomenon of magnetoresistance (MR) was discovered more than 150 years ago by Lord Kelvin, when he found experimentally that iron and nickel samples exhibit higher resistivity $\rho_{\parallel}$ when the magnetisation **M** is saturated in the direction of a current flow ($\mathbf{M} \parallel \mathbf{I}$), and lower resistivity $\rho_{\perp}$ when **M** is saturated perpendicular to the current ($\mathbf{M} \perp \mathbf{I}$). AMR is defined as the relative change in resistivity between the two configurations: AMR =

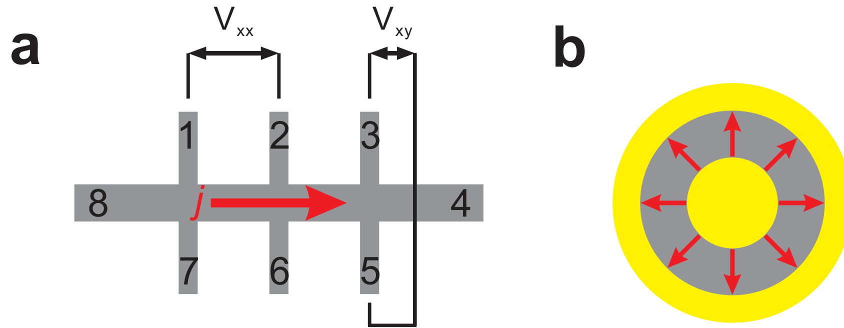

Figure 2.7: Sketches of standard device structures for transport measurements: **a,** Hall bar and **b,** Corbino disk (The yellow parts represent metal contacts).

$(\rho_{\parallel} - \rho_{\perp})/\rho_{\parallel}$. In (Ga,Mn)As it is found that $\rho_{\parallel} < \rho_{\perp}$ [116, 117], opposite to that observed in metal systems.

For an isotropic sample in a single domain state, the longitudinal and transverse resistivity ρ_{xx} and ρ_{xy} can be expressed as [116, 118]:

$$\rho_{xx} = \rho_{\perp} - (\rho_{\perp} - \rho_{\parallel}) \cos^2 \vartheta \quad (2.6)$$

$$\rho_{xy} = -(\rho_{\perp} - \rho_{\parallel}) \cos \vartheta \sin \vartheta \quad (2.7)$$

where ϑ is the angle between **M** and **I**. Note that the transverse AMR is also referred to as planar Hall effect [118].

Figure 2.8 shows the typical resistance measured on a (Ga,Mn)As Hall bar when a constant external magnetic field $\mathbf{H}_0$ is rotated in-plane with the sample. In this case the applied field $\mathbf{H}_0$ is much stronger than the saturation magnetisation M_s of the material so that $\mathbf{M} \parallel \mathbf{H_0}$ for all ϑ. The angle dependence described by Equations 2.6 and 2.7 is clearly observed.

When the single domain assumption is not applicable, the measured AMR has two contributions: spin-orbit interaction and non-cubic symmetry induced by epitaxial strain [119]. This leads to observations that the $\rho_{xx}(\vartheta)$ and $\rho_{xy}(\vartheta)$ curves not only depend on the angle between **M** and **I** (non-crystalline AMR), but also on the directions of **I** and **M** with respect to the crystal axes (crystalline AMR) [117, 120]. For systems exhibiting cubic

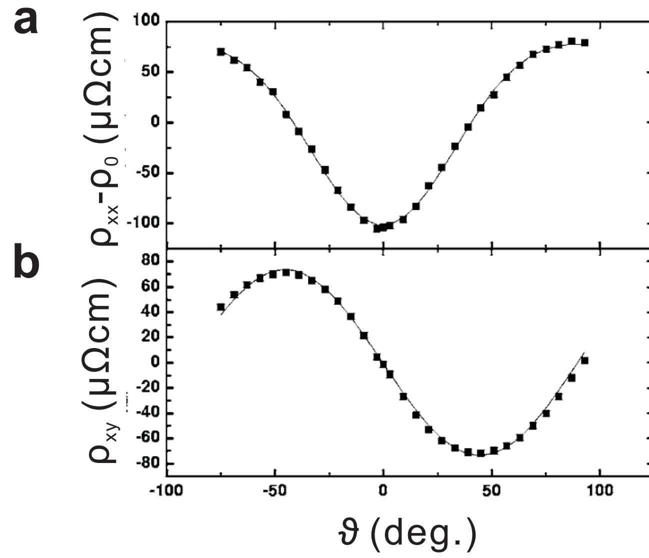

Figure 2.8: Measurements on the longitudinal and transverse resistivity on a Hall bar (3.4% Mn) in a rotating magnetic field of 0.6 T at 4.2 K, adapted from [116]. **a,** The longitudinal resistivity $\rho_{xx} - \rho_0$, where $\rho_0 = (\rho_{\parallel} + \rho_{\perp})$. The solid line is the fitted results according to Equation 2.6. **b,** The transverse resistance ρ_{xy} and fitted results according to Equation 2.7 (solid line).

[100] and uniaxial [110] anisotropy, the AMR components can be described as [120, 121]:

$$\frac{\rho_{xx}-\rho_{\text{ave}}}{\rho_{\text{ave}}} = C_I\cos 2\vartheta + C_U\cos 2\phi + C_C\cos 4\phi + C_{I,C}\cos(4\phi - 2\vartheta) \quad (2.8)$$

$$\frac{\rho_{xy}-\rho_{\text{ave}}}{\rho_{\text{ave}}} = C_I\sin 2\vartheta - C_{I,C}\cos(4\phi - 2\vartheta) \quad (2.9)$$

where ϕ is the angle between $\mathbf{M}$ and the [110] crystal direction, and ρ_{ave} is the average value of the longitudinal resistivity as the magnetic field is rotated through 360°. C_I represents the non-crystalline AMR coefficient, C_U and C_C are the uniaxial and cubic crystalline AMR coefficients respectively, and $C_{I,C}$ is a crossed non-crystalline/crystalline term. The crystalline AMR components in (Ga,Mn)As devices have been experimentally identified and extensively studied in Ref. [120–122].

Experimentally the transverse resistivity ρ_{xy} has been used to determine the magnetic anisotropy constants: In the case that the applied field is smaller than M_s, the magnetisation vector $\mathbf{M}$ does not generally follow $\mathbf{H}_0$, but instead stays in a direction which minimises the total free energy of the system. Figure 2.9 illustrates the typical results from such measurements [118].

In a (Ga,Mn)As device, the primary contributions to the total energy are the magnetocrystalline anisotropy energies. Combining Equations 2.3, 2.4 and 2.5, and considering only the in-plane anisotropy (i.e. $\theta = 90°$ in Figure 2.3), the free energy density E is given as [10, 116, 118]:

$$E = \mu_0\frac{MH_{4\parallel}}{8}\sin^2 2\varphi + \mu_0\frac{MH_{2\parallel}}{2}\sin^2(\varphi - 45°) - \mu_0 M H_0\cos(\varphi_H - \varphi) \quad (2.10)$$

Here $M = |\mathbf{M}|$; $H_{4\parallel}$ and $H_{2\parallel}$ are the first order in-plane biaxial and uniaxial anisotropy fields respectively, they are defined in terms of the anisotropy energies K_i according to $H_i = 2K_i/\mu_0 M_s$ (cf. Equation 2.1). [110] is the easy axis when $H_{2\parallel} > 0$. The third term in the expression corresponds to the Zeeman energy. The small shape anisotropy associated with the device is neglected.

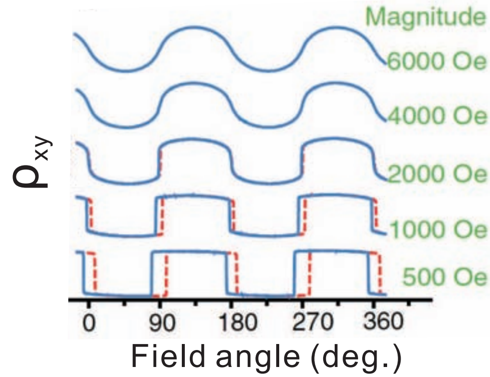

Figure 2.9: The transverse resistivity ρ_{xy} on a (Ga,Mn)As Hall bar in a group of fixed-magnitude field rotation measurements, adapted from [118]. At large $\mathbf{H}_0$, the magnetisation is saturated in the direction of the field, i.e. $\mathbf{M} \parallel \mathbf{H}_0$, and the measured $\rho_{xy}(\vartheta)$ agrees with Equation 2.7. At small $\mathbf{H}_0$ (< 1000 Oe), $\mathbf{M}$ no longer follows $\mathbf{H}_0$, instead only stays along the easy axes where the total energy is minimum, and the rotation of $\mathbf{H}_0$ causes $\mathbf{M}$ to switch from one easy axis to the next. The hysteresis loops of magnetisation switching are clearly observed (The red and blue lines are from clockwise and counterclockwise rotations respectively).

By determining the angle φ between $\mathbf{M}$ and the crystalline axis using Equation 2.7, and then imposing the conditions $\partial E/\partial\varphi = 0$ and $\partial^2 E/\partial^2\varphi > 0$ on Equation 2.10 (i.e. $\mathbf{M}$ always lies in the direction which minimises the total energy in the system), the in-plane anisotropy constants $H_{4\parallel}$ and $H_{2\parallel}$ can be determined.

2.3.2 Anomalous Hall effect

The Hall resistivity measured in a magnetic semiconductor can be described as [107]:

$$\rho_{\mathrm{Hall}} = R_{\mathrm{o}}B + R_{\mathrm{s}}M \tag{2.11}$$

where the first term is from the ordinary Hall effect with the ordinary Hall coefficient R_{o}, caused by the deflection of charge carriers by a magnetic field; the second term is from the anomalous Hall effect (AHE), which is described by the product of the magnetisation $\mathbf{M}$ and the spontaneous Hall coefficient R_{s} arising from the spin-orbit interaction.

Careful AHE measurements can be used to determine the saturation magnetisation M_s in (Ga,Mn)As samples, and this allows determination of T_C by examining the temperature-dependence of M_s [117, 123], as demonstrated in Figure 2.10.

2.4 Magnetisation dynamics

So far only the response of the magnetisation to a dc magnetic field has been discussed. It is therefore natural to ask: How does $\mathbf{M}$ respond when it is under the influence of an oscillation magnetic field, with frequency approaching the natural resonance frequency of $\mathbf{M}$?

2.4.1 Motion of magnetic moments

A classical approach to study the precession of magnetic moments in an external field is to consider a macroscopic magnetisation vector $\mathbf{M}$ which includes all individual magnetic moments (macrospin model). This is valid

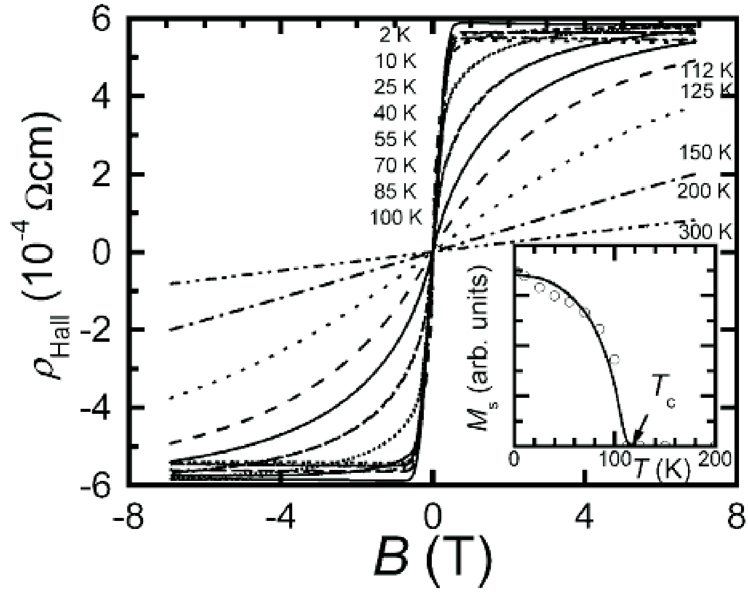

Figure 2.10: The anomalous Hall effect measurements, adapted from [107]. Magnetic field dependence of the Hall resistivity (ρ_{Hall}) in a (Ga,Mn)As device (5.3% Mn) at different temperatures. The saturation magnetisation M_s is determined for each curve. Inset: Plotting the temperature-dependence of M_s reveals the Curie temperature T_C.

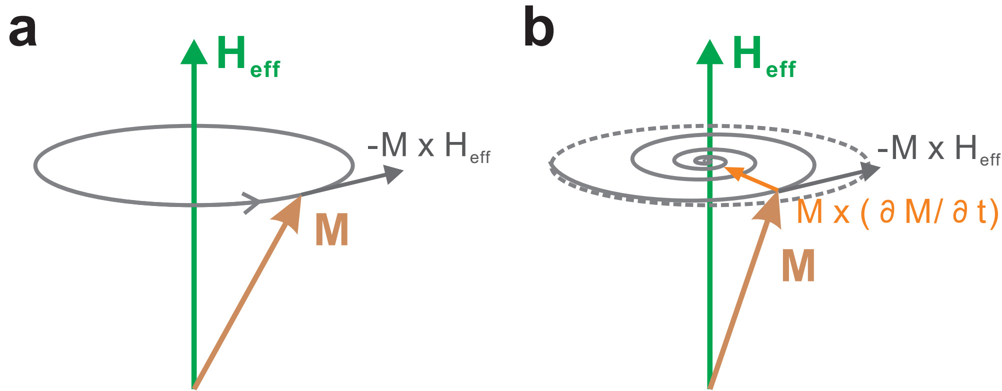

Figure 2.11: Schematic of magnetisation dynamics. **a,** The magnetisation vector **M** (brown) precesses counterclockwise around the effective magnetic field $\mathbf{H}_{\text{eff}}$ (green) following the LL equation (grey trace, described by Equation 2.12). **b,** Adding the phenomenological damping term $(\alpha/M_s)\mathbf{M} \times (\partial\mathbf{M}/\partial t)$ (orange), described in the LLG equation (Equation 2.14), causes the magnetic motion to relax towards the direction of $\mathbf{H}_{\text{eff}}$.

in ferromagnetic materials since all magnetic moments are correlated. A dynamic model for the motion of **M** was proposed by Landau and Lifshitz (LL) in 1935:

$$\frac{\partial\mathbf{M}}{\partial t} = -\gamma\mu_0\mathbf{M} \times \mathbf{H}_{\text{eff}} \tag{2.12}$$

Here $\mathbf{H}_{\text{eff}}$ is the effective magnetic field. It consists of the applied magnetic field $\mathbf{H}_0$ and the internal fields (such as anisotropy, demagnetisation, etc.), and determines the equilibrium orientation of **M**.

According to the LL model, **M** is connected to a total angular momentum which is subject to a torque, resulting in its precessional motion. However, the behaviour predicted by Equation 2.12 pictures an undamped precession with a constant cone angle, and is not consistent with experimental observations: The magnetisation always aligns with the direction of minimal energy after a finite time. Landau and Lifshitz amended this inconsistency by adding a phenomenological dissipation term:

$$\frac{\partial\mathbf{M}}{\partial t} = -\gamma\mu_0\mathbf{M} \times \mathbf{H}_{\text{eff}} - \frac{\lambda}{\gamma M_s^2}\mathbf{M} \times (\mathbf{M} \times \mathbf{H}_{\text{eff}}) \tag{2.13}$$

where $\lambda > 0$ is a phenomenological damping constant and has the dimension of frequency. In Equation 2.13 the magnitude of the magnetisation is conserved according to $|\mathbf{M}| = M_s$.

While Equation 2.13 can account for experimental observations, the most commonly used equation of motion is the Landau-Lifshitz-Gilbert (LLG) equation. It consists of the same precessional term as in the LL equation (Equation 2.12) but with a different damping term. This phenomenological dissipation term after Gilbert (1955) models a "viscous" damping and depends on the time derivative of the magnetisation. The LLG equation is written as [124]:

$$\frac{\partial \mathbf{M}}{\partial t} = -\gamma\mu_0 \mathbf{M} \times \mathbf{H}_{\text{eff}} + \frac{\alpha}{M_s}\mathbf{M} \times \frac{\partial \mathbf{M}}{\partial t} \tag{2.14}$$

where α is the phenomenological dimensionless Gilbert damping parameter.

2.4.2 Ferromagnetic resonance

Ferromagnetic resonance (FMR) is a condition in which steady-state precession of $\mathbf{M}$ occurs in a ferromagnetic system. To counter the effect of damping, the magnetisation is subject to a driving torque usually from an ac magnetic field.

FMR is closely related to two other phenomena, namely the electron spin resonance (ESR) and nuclear magnetic resonance (NMR). In these two situations, magnetic resonance occurs when the angular frequency (ω) of the ac magnetic field and the static magnetic field $\mathbf{H}_0$ satisfy the following condition:

$$\omega = -\gamma\mu_0 \mathbf{H}_0 \tag{2.15}$$

where γ is the gyromagnetic ratio of the electrons (ESR) or the nuclei (NMR). The steady-state precession of magnetic moments in an external magnetic field is known as Larmor precession.

In a ferromagnetic system, the presence of the internal magnetic field makes the condition for Larmor precession more complex. In particular, the rotational axis of $\mathbf{M}$ now lies along the direction the effective magnetic field

$\mathbf{H}_{\text{eff}}$ (Figure 2.11b), which is determined by the functional derivative of the total free energy density E with respect to $\mathbf{M}$:

$$\mathbf{H}_{\text{eff}} = -\frac{1}{\mu_0}\nabla_{\mathbf{M}} E \tag{2.16}$$

For (Ga,Mn)As epilayers under tetragonal distortion, the total free energy density[1] E is expressed as (see Figure 2.3 for the coordinate system) [74]:

$$\begin{aligned} E \ = \ & \frac{1}{2}\mu_0 M \Big\{ -2H_0[\cos\theta\cos\theta_H + \sin\theta\sin\theta_H\cos(\varphi-\varphi_H)] \\ & + M\cos^2\theta - H_{2\perp}\cos^2\theta - \frac{1}{2}H_{4\perp}\cos^4\theta \\ & - \frac{1}{2}H_{4\parallel}\frac{1}{4}(3+\cos 4\varphi)\sin^4\theta - H_{2\parallel}\sin^2\theta\sin^2\left(\varphi - \frac{\pi}{4}\right) \Big\} \end{aligned} \tag{2.17}$$

Here the first term describes the Zeeman energy; the second term is the demagnetisation energy (shape anisotropy, as in Equation 2.2); and the remaining are magnetocrystalline anisotropy energy terms, in which $H_{2\perp}$ and $H_{4\perp}$ represent the perpendicular-to-plane uniaxial and cubic anisotropy fields, respectively (cf. Equations 2.3, 2.4 and 2.5); $H_{2\parallel}$ and $H_{4\parallel}$ are the in-plane uniaxial and cubic anisotropy fields, respectively. As usual, the anisotropy fields H_i are defined in terms of the energies K_i according to $H_i = 2K_i/\mu_0 M_s$.

In the case of submicron devices, the energy from the additional uniaxial anisotropy caused by strain-relaxation (see Section 2.2.4) can be described as [67]:

$$E_U = -\frac{\mu_0 M_s H_U}{2}\sin^2\theta\sin^2(\varphi - \varphi_U) \tag{2.18}$$

where φ_U denotes the angle of the easy axis of H_U with respect to the [100] direction.

Solving the LLG equation (Equation 2.14) using the effective magnetic field $\mathbf{H}_{\text{eff}}$ allows all aspects of the magnetisation dynamics to be investigated. Ferromagnetic resonance spectroscopy therefore is an extremely powerful tool for studying the magnetic properties of ferromagnetic thin layers.

[1] Equation 2.17 is the most general expression of the total free energy density in a (Ga,Mn)As system. The expression given by Equation 2.10 is a simplified version.

The condition for Larmor precession in ferromagnets can be directly derived from the free energy density E following an approach developed by Smit and Beljers [125], also independently by Suhl [126]. For a specific orientation of the applied field (θ_H, φ_H), the resonance condition is given as the partial derivatives of E in spherical polar coordinates [69, 126]:

$$\left(\frac{\omega}{\gamma}\right)^2 = \frac{1}{M_s^2 \sin^2\theta}\left[\frac{\partial^2 E}{\partial\theta^2}\frac{\partial^2 E}{\partial\varphi^2} - \left(\frac{\partial^2 E}{\partial\theta\partial\varphi}\right)^2\right] \tag{2.19}$$

Combining Equations 2.17 and 2.19, the ferromagnetic resonance condition is given as [73, 74]:

$$\left(\frac{\omega}{\gamma}\right)^2 = \mu_0^2[(H_{\text{res}} \times a_1 + b_1)(H_{\text{res}} \times a_2 + b_2) - b_3^2] \tag{2.20}$$

Here

$$a_1 = \cos\theta\cos\theta_H + \sin\theta\sin\theta_H\cos(\varphi - \varphi_H) \tag{2.21}$$

$$\begin{aligned} b_1 = & -\left[M - H_{2\perp} + H_{2\parallel}\cos^2\left(\varphi + \frac{\pi}{4}\right)\right]\cos 2\theta \\ & + H_{4\perp}\frac{\cos 2\theta + \cos 4\theta}{2} + H_{4\parallel}\frac{\cos 4\theta - \cos 2\theta}{2}\frac{3 + \cos 4\varphi}{4} \end{aligned} \tag{2.22}$$

$$\begin{aligned} b_2 = & -(M - H_{2\perp})\cos^2\theta + H_{4\parallel}\sin^2\theta\left(\cos 4\varphi - \cos^2\theta\frac{3 + \cos 4\varphi}{4}\right) \\ & + H_{4\perp}\cos^4\theta - H_{2\parallel}\left\{\sin 2\varphi + \left[\cos\theta\cos\left(\varphi + \frac{\pi}{4}\right)\right]^2\right\} \end{aligned} \tag{2.23}$$

$$b_3 = \frac{1}{2}\cos\theta\left(\frac{3}{2}H_{4\parallel}\sin 4\varphi\sin^2\theta + H_{2\parallel}\cos 2\varphi\right) \tag{2.24}$$

It is customary to define $M_{\text{eff}} = M - H_{2\perp}$ since the two terms always appear together. Note that Equation 2.20 can be greatly simplified if the magnetisation is saturated along $\mathbf{H}_0$, i.e. $\theta = \theta_H$ and $\varphi = \varphi_H$. This can be easily achieved in (Ga,Mn)As as M_s is generally low (a few tens of mT) due to the diluted magnetic moments in the material. By measuring the angle/frequency dependence of the resonance field H_{res}, the anisotropy constants can be determined.

The strain-relaxation-induced anisotropy H_U is not included in the above equations, since its general form is rather complex and is rarely used. In Section 3.3, an expression for H_U specific to the experiments described in this Thesis is provided.

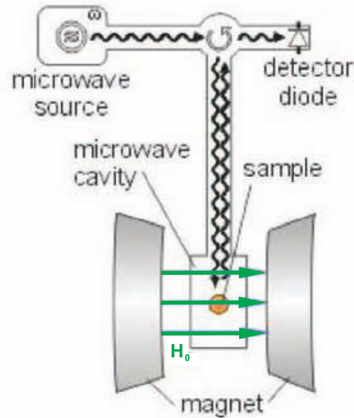

Figure 2.12: Conventional cavity-based FMR spectroscopy, adapted from [78]. The microwave radiation is transferred from the source to the sample, and the reflected wave is sent to a diode detector.

2.4.3 Detection of magnetic motion

In a conventional FMR experiment, a magnetic material is exposed to a microwave electromagnetic radiation at a fixed frequency ω typically in the gigahertz (GHz) range. By sweeping the external field $\mathbf{H}_0$, the magnetic material is driven through the resonance condition (Equation 2.20). On resonance, strong absorption of the incident radiation occurs and a peak appears in the energy absorption spectrum. Figure 2.12 shows a schematic setup of conventional FMR spectroscopy, which utilises a combined microwave waveguide/cavity to transfer the radiation from the microwave source to the sample, and subsequently transfer the reflected wave to a diode detector.

However, this energy-absorption-based FMR is not sensitive enough to be applied on micrometre-scale sample. To perform device-scale FMR, other approaches for signal detection have recently been introduced, which include magneto-optical Kerr effect [67], x-rays [88], and an electrical method based on a frequency mixing effect [34, 35, 79, 81, 83–87].

The frequency mixing effect has been employed in the experiments described in this Thesis. This technique relies on the fact that the precessing

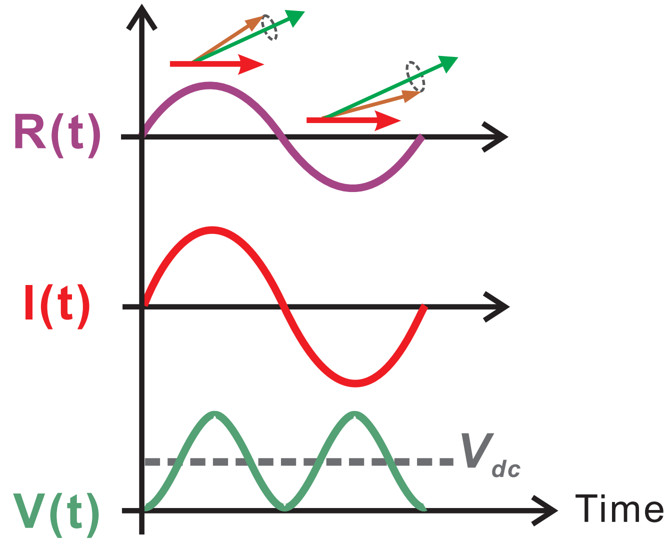

Figure 2.13: Principle of the frequency mixing effect. The precessing magnetisation **M** causes a time-dependent change $R(t)$ in the device's resistance, and the ac current $I(t)$ inside the sample also oscillates at the same frequency. Product of the two gives rise to an ac voltage component varying at double frequency and a dc voltage component (photovoltage).

magnetisation causes a time-dependent change in the sample's resistance[1] $\Delta R(t)$ from the equilibrium value R_0. The resistance oscillates at the same frequency as the driving torque, and when combined with the time-dependent current inside the device $I\cos(\omega t)$, gives rise to a dc voltage across the sample. This dc voltage V_{dc}, referred to as "photovoltage" in this Thesis, allows the magnetic motion in the micro-devices to be detected. Figure 2.13 illustrates schematically the frequency mixing effect.

The electrical detection method has a few advantages: Firstly, it only requires a voltmeter which can be integrated seamlessly into the rest of the FMR setup (as shown in the experiment setup in this Thesis). There is no requirement for additional optical or x-ray detection suite. Secondly, the

[1]The resistance change can be due to the tunnelling/giant magnetoresistance (TMR/GMR) in a MTJ/spin-valve device [34, 35], or domain wall resistance in a nanowire [127], or the AMR in a uniform magnetic structure [79, 81, 83–87].

technique is compatible with individual nanoscale devices (measurements on sub-100 nm devices have been demonstrated in Ref. [35] and also in Chapter 5), in which the energy absorption signature is too small for conventional FMR spectroscopy to detect.

If the magnetisation $\mathbf{M}$ precesses under the driving torque of a microwave frequency excitation field $\mathbf{h}_{\text{mw}} = (h_x, h_y, h_z)e^{i\omega t}$, and the current inside the sample[1] is $\mathbf{I} = (I_x, 0, 0)e^{i\omega t}$, the ferromagnetic resonance curve detected in the photovoltage spectrum V_{dc} can be described by solving the LLG equation (Equation 2.14). Its lineshape is found to be a combination of symmetric and anti-symmetric Lorentzian functions:

$$V_{\text{dc}} = V_{\text{sym}} \frac{\Delta H^2}{(H_0 - H_{\text{res}})^2 + \Delta H^2} + V_{\text{asy}} \frac{\Delta H(H_0 - \Delta H)}{(H_0 - H_{\text{res}})^2 + \Delta H^2} \tag{2.25}$$

with the amplitudes of the two components given as:

$$V_{\text{sym}}(\vartheta) = \frac{I\Delta R}{2} A_{\text{sym}} \sin(2\vartheta) h_z \tag{2.26}$$

$$V_{\text{asy}}(\vartheta) = \frac{I\Delta R}{2} A_{\text{asy}} \sin(2\vartheta)(h_x \sin\vartheta + h_y \cos\vartheta) \tag{2.27}$$

Here ϑ is the angle between the magnetisation vector $\mathbf{M}$ and the current $\mathbf{I}$. The terms A_{sym} and A_{asy} are the scalar amplitudes of the magnetic susceptibility ($A_i = \chi_i / M_s$). In the case that the magnetisation is saturated, i.e. $\mathbf{M} \parallel \mathbf{H}_0$, they can be expressed as:

$$A_{\text{sym}} = \frac{\gamma(H_{\text{res}} + b_1)(H_{\text{res}} + b_2)}{\omega \Delta H(2H_{\text{res}} + b_1 + b_2)} \tag{2.28}$$

$$A_{\text{asy}} = \frac{(H_{\text{res}} + b_1)}{\Delta H(2H_{\text{res}} + b_1 + b_2)} \tag{2.29}$$

where b_1 and b_2, defined in Equations 2.22 and 2.23, are terms containing the anisotropy energies of the system. The derivations for Equations 2.25 – 2.29 are given in Appendix A.

[1] It is assumed here that the current $\mathbf{I}(t)$ and the driving field $\mathbf{h}_{\text{mw}}(t)$ are in-phase. A phase difference (ψ) between the two terms results in an imaginary part in the expression of V_{dc}, see Appendix A.

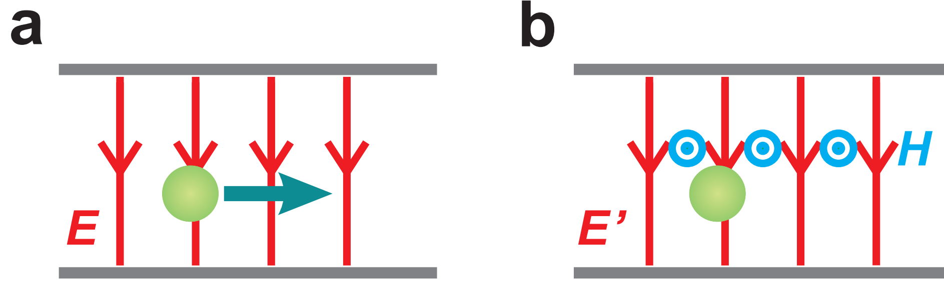

Figure 2.14: The effect of an electric field to a moving electron in: **a,** the rest frame of the electric field; and **b,** the rest frame of the electron. In the electron's own reference frame, the electric field is moving, and generates an effective *magnetic* field according to Lorentz transformation. This effective magnetic field then couples to the electron spins.

2.5 Spin-orbit interaction in semiconductors

As introduced in Section 1.2.1, spin-orbit interaction offers a pathway to spin manipulation using electric fields alone. For a semiconductor in the presence of spin-orbit coupling, the one-particle Hamiltonian can be written as [38, 50]:

$$\mathcal{H} = \mathcal{H}_{\mathrm{F}} + \mathcal{H}_{\mathrm{SO}} \tag{2.30}$$

$$\mathcal{H}_{\mathrm{F}} = \frac{p^2}{2m} + V \tag{2.31}$$

$$\mathcal{H}_{\mathrm{SO}} = \frac{\hbar}{4m^2c^2}\left[\nabla V \times \vec{p}\,\right] \cdot \vec{\sigma} \tag{2.32}$$

where $\mathcal{H}_{\mathrm{F}}$ represents the free-electron Hamiltonian and $\mathcal{H}_{\mathrm{SO}}$ described the interaction between the carrier spin and the carrier momentum. Here V is the electric potential and ∇V is the effective local electric field seen by the charge with momentum operator $\vec{p}$. $\vec{\sigma}$ is the electron spin operator. In materials with holes as charge carriers, such as (Ga,Mn)As and (Ga,Mn)(As,P), $\vec{\sigma}$ should be replaced by the total angular momentum $\vec{J}$ [39].

One can think of $\mathcal{H}_{\mathrm{SO}}$ as a consequence of special relativity, where an electric field transforms into a magnetic field in the reference frame of a moving electron and influences its spin, as illustrated in Figure 2.14.

The Hamiltonian described by Equation 2.30 is invariant under time-reversal operations. This implies that if both the electron wavevector $\vec{k}$ and its spin $\vec{s} = \vec{\sigma}/2$ reverse signs, the energy of the conduction band must stay the same, i.e. $E\left(\vec{k},\uparrow\right) = E\left(-\vec{k},\downarrow\right)$. This degeneracy is called Kramers degeneracy[1] [50]. Consider the following two cases:

- If the Hamiltonian possesses inversion symmetry, i.e. $E\left(\vec{k},\uparrow\right) = E\left(-\vec{k},\uparrow\right)$, since the inversion operation reverses $\vec{k}$ but not $\vec{s}$, it is found that $E\left(\vec{k},\uparrow\right) = E\left(\vec{k},\downarrow\right)$ for all $\vec{k}$, i.e. the bands are always spin degenerate in a system with inversion symmetry.

- If the Hamiltonian lacks inversion symmetry, the relation $E\left(\vec{k},\uparrow\right) = E\left(-\vec{k},\downarrow\right)$ still holds, but for $\vec{k} \neq \vec{0}$ the bands are no longer necessarily degenerate and spin-splitting occurs.

Dresselhaus spin-orbit interaction If a crystal has bulk inversion asymmetry (BIA), for example a zinc-blende structure such as in GaAs, Dresselhaus [44] has shown that the spin-orbit coupling is proportional to k^3 and has the following form:

$$\mathcal{H}_D = \gamma_0 \left[\sigma_x k_x \left(k_y^2 - k_z^2\right) + \sigma_y k_y \left(k_z^2 - k_x^2\right) + \sigma_z k_z \left(k_x^2 - k_y^2\right)\right] \tag{2.33}$$

where γ_0 is a parameter measuring the strength of coupling.

When such as crystal is subject to strain at the interface, this introduces structure inversion asymmetry (SIA) which yields a spin-orbit coupling term linear in k [48]:

$$\mathcal{H}_4 = C_4 \left[\sigma_x k_x(\varepsilon_{yy} - \varepsilon_{zz}) + \sigma_y k_y(\varepsilon_{zz} - \varepsilon_{xx}) + \sigma_z k_z(\varepsilon_{xx} - \varepsilon_{yy})\right] \tag{2.34}$$

Here ε_{ij} are components of the Cauchy strain tensor which are defined as:

$$\varepsilon_{ij} = \frac{1}{2}\left(\frac{\partial u_i}{\partial r_j} + \frac{\partial u_j}{\partial r_i}\right) \tag{2.35}$$

[1] The Kramers degeneracy can be broken by the application of a magnetic field, in which case the time-reversal symmetry is destroyed.

where $\vec{r}$ is the equilibrium position of an atom in the crystal and $\vec{u}(\vec{r})$ is its displacement from the equilibrium position. Note that the strain tensor is symmetric, since an anti-symmetric tensor would correspond to the rotation of the crystal.

Rashba spin-orbit interaction In addition to the Dresselhaus spin-orbit coupling (Equations 2.33 and 2.34), in asymmetric quantum wells, or in the presence of deformation, Bychkov and Rashba have derived a different form of SIA spin-splitting [45]:

$$\mathcal{H}_R = \alpha\left(\vec{k} \times \hat{\mathbf{z}}\right) \cdot \vec{\sigma} \tag{2.36}$$

where α is the Rashba coefficient and the growth direction $\hat{\mathbf{z}}$ is the symmetry-breaking axis.

In deformed crystals, the Rashba coefficient α contains the off-diagonal strain elements[1] $\{\varepsilon_{xy}, \varepsilon_{yz}, \varepsilon_{zx}\}$ (sometimes also referred to as "shear" strain components), and the Hamiltonian can be written as [48, 128, 129]:

$$\mathcal{H}_R = C_3\left[\sigma_x(\varepsilon_{zx}k_z - \varepsilon_{xy}k_y) + \sigma_y(\varepsilon_{xy}k_x - \varepsilon_{yz}k_z) + \sigma_z(\varepsilon_{yz}k_y - \varepsilon_{zx}k_x)\right] \tag{2.37}$$

The Rashba spin-orbit coupling therefore introduces an effective magnetic field perpendicular to $\vec{k}$, and its relative orientation to $\vec{k}$ remains constant in the plane normal to $\hat{\mathbf{z}}$ in contrast to the Dresselhaus term [130].

Figure 2.15 illustrates the orientations of the effective magnetic fields resulting from the linear Dresselhaus and Rashba spin-orbit interactions in a zinc-blende crystal with respect to $\vec{k}$.

[1] The off-diagonal strain components $\{\varepsilon_{xy}, \varepsilon_{yz}, \varepsilon_{zx}\}$ can be induced by an uniaxial strain along the [110] crystal axis, for example [50].

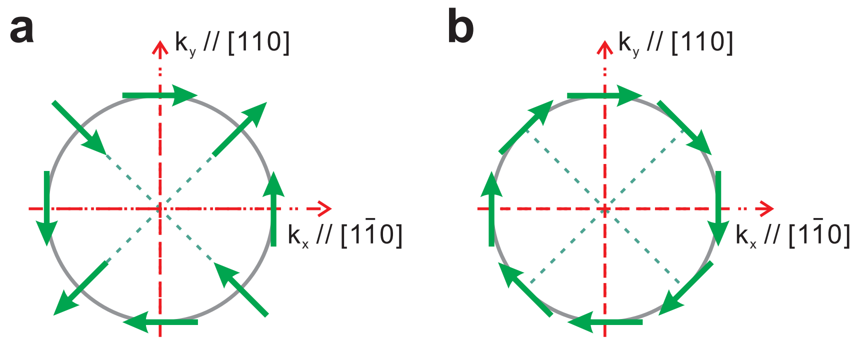

Figure 2.15: Orientations of the effective magnetic fields due to spin-orbit coupling, adapted from [54]. **a,** The directions of the effective field resulting from the linear Dresselhaus term, with respect to $\vec{k}$ on a unit circle. **b,** The orientations of the field due to the Rashba term.

Chapter 3

On-chip driven ferromagnetic resonance on individual (Ga,Mn)As microdevices

3.1 Introduction

Conventional ferromagnetic resonance (FMR) spectroscopy has been extensively utilised in the study of magnetic anisotropy in bulk (Ga,Mn)As wafers [71–76]. However, cavity-based FMR is not sensitive enough for detecting the magnetic motion in micron-scale ferromagnets.

In this Chapter, FMR experiments on individual submicron (Ga,Mn)As devices are reported. An all-electrical, device-scale FMR technique, originally developed on permalloy systems, is employed [83, 84], which uses a current-carrying waveguide to generate a local excitation field to drive the magnetic precession, and employs the frequency mixing effect (Section 2.4.3) to detect the magnetic motion.

Similar locally driven FMR experiments on individual (Ga,Mn)As nanostructures have also been reported [67], in which the magnetic motion is detected using time-resolved scanning Kerr microscopy with a spatial resolution of 500 nm. The all-electrical FMR technique presented in this Chapter, on the other hand, allows measurements on devices down to sub-100 nm in size.

3.2 Devices and experimental methods

3.2.1 Device preparation

The $(Ga_{1-x},Mn_x)As$ wafers are grown on GaAs(001) substrates with LT-MBE by Richard Campion and coworkers at the University of Nottingham. Films with Mn concentrations of 3% and 6% have been used for the experiments.

In the first step of device fabrication, e-beam lithography[1] and reactive ion etching have been used to create isolation trenches on the magnetic films, which define the microstructures. The trenches are 200 nm-wide and are etched into the GaAs substrates for approximately 150 nm. The micro-bars are patterned along either the [100] or [010] crystalline directions. They also contain two large bond pads on each end, which are covered with Cr/Au ohmic contacts (20/200 nm-thick) made from a second step of e-beam lithography and evaporation. The full recipe for the device fabrication is given in Appendix C.

A Cr/Au coplanar stripline waveguide (CPS) is lithographically placed next to the device. It is patterned on an area where the (Ga,Mn)As epilayer has been removed with reactive ion etching, leaving only the semi-insulating GaAs substrate. The CPS is designed with 50 Ω characteristic impedance[2] to match that of the microwave transmission line. Close to the sample ($\sim 2\ \mu$m), the ground and central lines of the CPS are shorted together. This way when a microwave current flows through the waveguide, a microwave magnetic field $\mathbf{h}_{\mathrm{mw}}$ is generated (Ampère's circuital law) in the vicinity of the (Ga,Mn)As microstructure, which in turn induces an oscillating Eddy current $I\cos\omega t$ inside the sample. From the position of the waveguide, it is clear that the microwave excitation is mainly out-of-plane, i.e. $\mathbf{h}_{\mathrm{mw}} = (0, 0, h_z)e^{i\omega t}$, where $\hat{z} \parallel [001]$ (Figure 3.1c). Since the device and the CPS are defined at different stages of the fabrication process, careful alignment is required to ensure that the shorted-end is as close to the micro-bar as possible, in order to maximise

[1]The e-beam lithography of the devices is performed by Andrew Ferguson.

[2]The equations for calculating the characteristic impedance in CPS and CPW can be found in Ref. [131].

the driving field. Figure 3.1a shows the scanning electron microscopy (SEM) images of a device.

3.2.2 Measurement apparatus

The sample chips are glued[1] onto carriers which are specially designed for the FMR experiments (Figure 3.2a). The sample carrier is a printed-circuit board (PCB), which is designed to contain 10 dc lines for measuring the photovoltage, and a coplanar waveguide (CPW) for coupling with a SMA connector for microwave current input. The CPW also has an open end for coupling with the coplanar stripline waveguide on the chip. The reason for the three-step transfer of microwave current (SMA $\rightarrow$ CPW $\rightarrow$ CPS) is because that the precision required for making a CPS waveguide with 50 Ω impedance is beyond the capability of PCB-tooling machines (but well within the reach of lithographical methods). The CPS waveguide on the sample chip is wire-bonded to the CPW on the carrier. Multiple bonds are made between the two waveguides in order to reduce the inductance of the bond-wires ($\sim$ 1 nH/mm), as shown in Figure 3.2b.

The FMR experiments are performed in a varying-temperature cryostat (manufactured by *Cryogenic Limited*). The samples are cooled to 6 K using He vapour with temperature variation less than 0.05 K. The cryostat is equipped with a 3-coil superconducting magnet, with each magnet able to generate a magnetic field up to 1 T. This allows 3D rotation of the applied magnetic field $\mathbf{H}_0$ during the experiment without physically disturbing the sample.

Measurements are performed using a dipstick custom made specially for this cryostat. Figure B.1 shows a photo of the dipstick. In order to minimise thermal conduction, the body of the dipstick is made of stainless steel. Inside

[1] GE Varnish (also known as IMI-7031) is used as the adhesive for attaching samples onto the carriers, due to its good thermal conductivity, compatibility with cryogenic temperatures, and ease of removal (with methanol/ethanol).

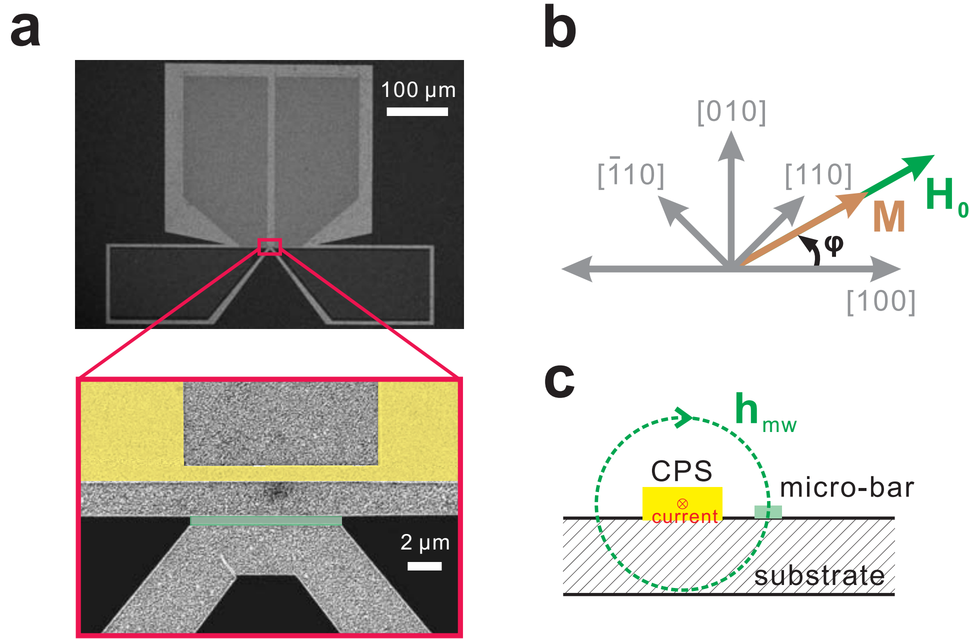

Figure 3.1: **a,** SEM images of the sample chip and an enlarged photo on the micro-bar (cyan false colour), which is 500 nm-wide and 10 μm-long. A Cr/Au coplanar stripline waveguide with 50 Ω impedance is lithographically placed next to the device (yellow false colour). It is placed directly on the semi-insulating GaAs surface. **b,** Vector diagram of $\mathbf{M}$ and the external magnetic field $\mathbf{H}_0$. φ is the angle between $\mathbf{M}$ and the [100] direction. **c,** Cross-section of a sample. A current inside the shorting wire generates a magnetic field perpendicular to the (Ga,Mn)As device, according to Ampère's law.

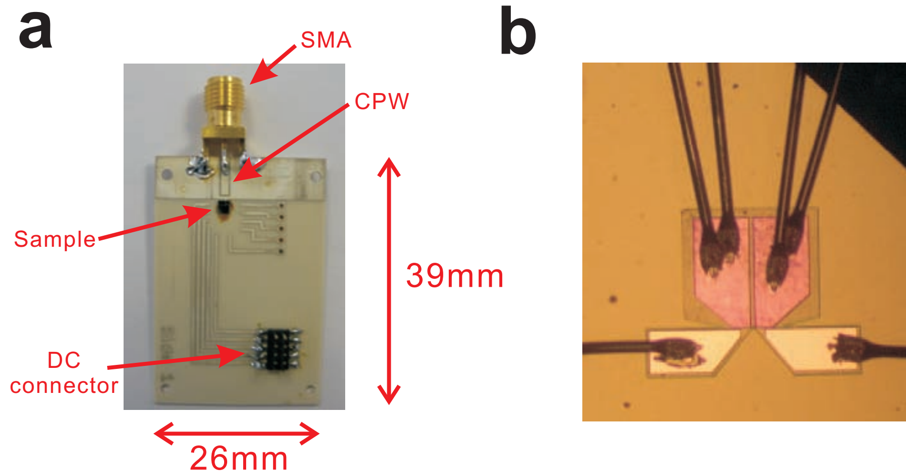

Figure 3.2: **a,** The sample carrier used in the FMR experiments. **b,** Micrograph of a prepared sample.

there are 10 constantan[1] wires for carrying dc signals, and 24 copper wires for powering the electronic components mounted on the coldfinger which is attached to the end of the dipstick. The coldfinger is made of oxygen-free copper. This material is chosen because of its softness for tooling and good thermal conductivity. The top part of the coldfinger is designed to be large enough to host a wide range of high frequency components, such as amplifiers, couplers and bias-tees. The sample carrier is mounted at the bottom of the coldfinger, together with a Hall sensor and a temperature sensor[2].

The dipstick also consists of three semi-rigid coaxial cables[3] for carrying high frequency currents. For two of the coaxial cables, both the outer sheath

[1]Constantan is a copper-nickel alloy usually consisting of 55% copper and 45% nickel. Its main feature is that its resistivity stays constant over a wide range of temperatures. The constantan wire used on this dipstick are 110 μm in diameter and has resistivity $\sim 66\ \Omega$/m (Data from retailer's website: www.cmr-direct.com).

[2]The Hall sensor is from *Lakeshore Cryotronics, Inc.* (Model number: HGCT-3020). The magnetic field can be determined by measuring the Hall voltage with a four-probe technique. The temperature sensor is also from *Lakeshore Cryotronics, Inc.* (Model number: CX-1050-SD-1.4L). A Lakeshore Temperature Controller 340 is used for monitoring and controlling the temperature in the cryostat.

[3]The model number of the semi-rigid coaxial cables is UT-85, with outer diameter ~ 2.2 mm.

and the inner lines are made of stainless steel. This helps to minimise thermal conduction along the cables. However, due to the relatively large resistance of stainless steel, the loss in these cables becomes significant at high frequencies. Hence they are most suitable for carrying ac signals in the frequency range of MHz. The third coaxial cable consists of stainless steel outer sheath and a BeCu inner line, and is used for carrying signals in the range of GHz. Its attenuation at 10 GHz is 5 dBm/m. All three cables are terminated with SMA connectors (excellent electrical performance from dc to 18 GHz).

3.2.3 Measurement technique

Figure 3.3 shows schematically the experimental setup. The magnetic motion in the sample is detected electrically by measuring the dc photovoltage across the device with a voltmeter[1]. A lock-in technique is employed to improve the signal-to-noise ratio in the measurement: The microwave current from the source is alternated between "on" and "off" states by modulation with a square wave. A lock-in amplifier is then referenced to the frequency of this modulation, therefore records the difference in photovoltage between the two states, $V = V(I_{\text{on}}) - V(I_{\text{off}})$. This way only the additional voltage caused by the FMR-enhanced AMR effect is measured. Figure 3.4 illustrates the modulation square wave and the photovoltage captured by the voltmeter, as seen on an oscilloscope.

A practical consideration related to the lock-in technique is the modulation frequency. Since the microwave current causes Joule heating in the device, on resonance, the strong absorption of microwave radiation by the sample leads to increase in its temperature and hence changes in its resistance. This is another contribution to the measured FMR photovoltage. The sample cools down when the microwave current is periodically turned off. Therefore the modulation frequency determines the rate of oscillation in the sample's temperature, and the effect of Joule heating on the FMR

[1] To be precise, the photovoltage is measured using the differential mode on a low-noise voltage preamplifier (from *Stanford Research Systems*, model SR560), which is illustrated as a voltmeter in Figure 3.3. The signal is magnified by 2000 times before it is fed to the lock-in amplifier.

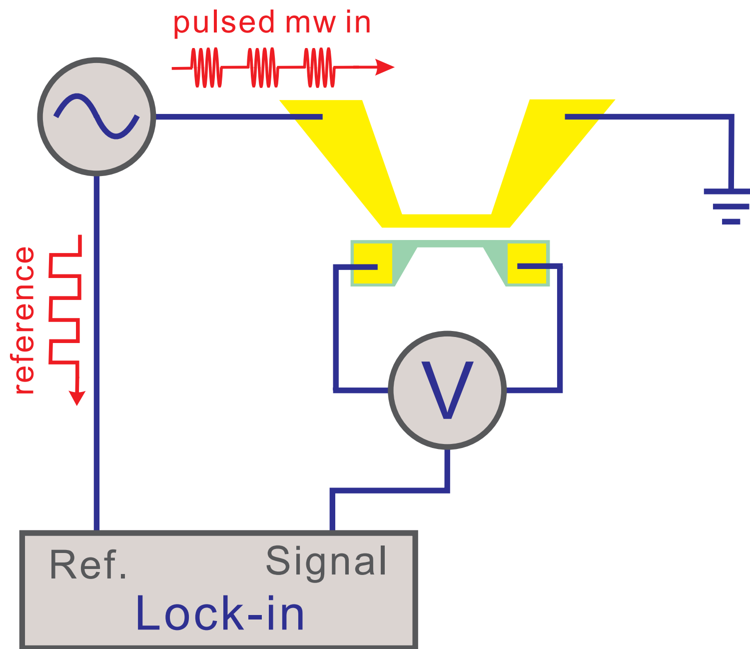

Figure 3.3: Schematic of the experimental setup (not-to-scale). A microwave current is injected into the coplanar stripline waveguide (yellow), which generates a microwave magnetic field to drive the magnetisation in the (Ga,Mn)As microstructure (cyan). A lock-in measurement technique is employed to improve the signal-to-noise ratio in the measurement.

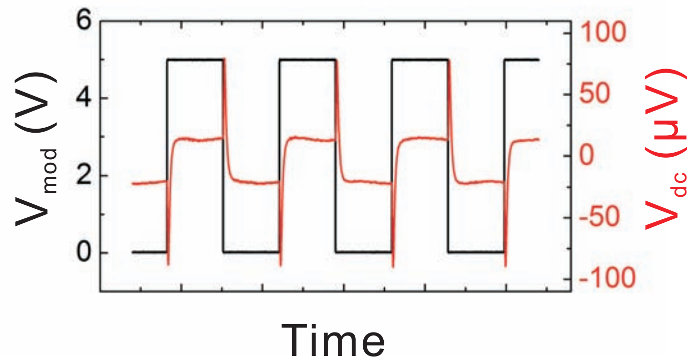

Figure 3.4: The modulation square wave (black) and the photovoltage detected by the voltmeter (red). The square wave is 5 $V_{pk\text{-}pk}$ and is offset by 2.5 V. This way the modulated microwave alternates between "on" and "off" states. The detected photovoltage oscillates at the same frequency with the modulation. Since lock-in amplifiers always detect signals as sine functions, in the case of a square wave (red curve), only the signal level in the middle of the square shape is measured, and the large spike noise seen at the beginning of each transition is discarded.

Device Name	Wafer	Condition	T_C (K)
A ($\parallel$ [010])	$(Ga_{0.97},Mn_{0.03})As$	Annealed	57/71
B ($\parallel$ [010])	$(Ga_{0.94},Mn_{0.06})As$	As-grown & Annealed	73/110
C ($\parallel$ [100])	$(Ga_{0.94},Mn_{0.06})As$	As-grown	73/110

Table 3.1: The three devices discussed in this Section. All are 500 nm-wide and 10 μm-long, and share the same bond pad design. Their orientations are shown next to the device names. The Curie temperature (T_C) at as-grown/annealed states are shown, with the annealing condition being 160°C in air for 10 h.

signal. This bolometric effect has been carefully studied on permalloy micro-bars and reported in Ref. [85]. In the experiments presented in this Chapter, a modulation frequency of 987.6 Hz has been chosen, and the level of noise signal in the measured photovoltage is found to be $\sim 0.3\ \mu$V.

3.3 Data and analysis

A total number of 5 (Ga,Mn)As micro-bars have been measured in this experiment. Consistent results among the devices have been obtained, and the typical data from three devices are presented in this Section. Their characteristics are listed in Table 3.1.

3.3.1 On-chip FMR using a waveguide

Similar to conventional FMR experiments, the microwave frequency is kept fixed and the external field $\mathbf{H}_0$ is swept. Figure 3.5a shows the photovoltage V_{dc} measured across Device A, when a driving field of 17 GHz is generated and $\mathbf{H}_0$ is swept along the $\varphi = 90^o$ direction (i.e. along [010], see Figure 3.1b). The coherent precession of Mn spins manifests as a dip clearly seen in the photovoltage spectrum, and its lineshape can be well described by Equation 2.25. The resonance field is deduced from the fitting to be $\mu_0 H_{res} = 350$ mT.

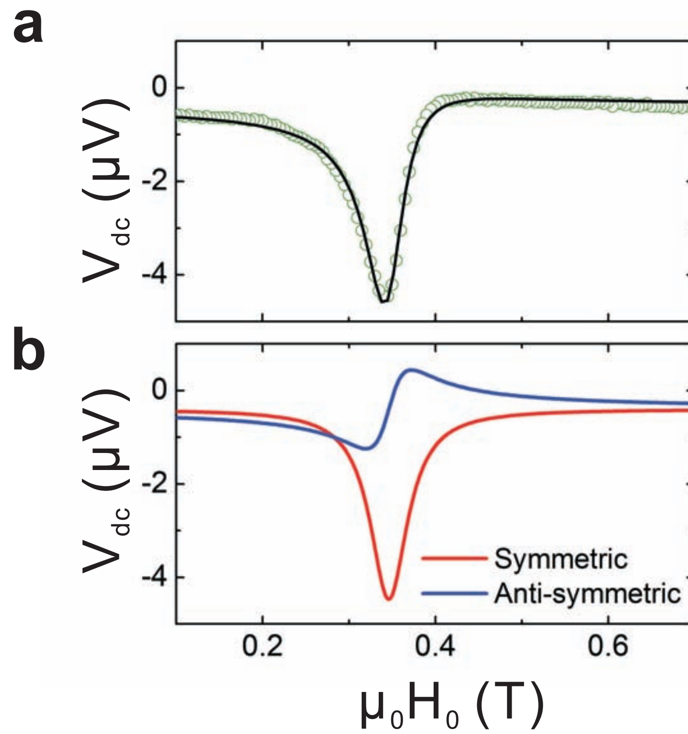

Figure 3.5: Ferromagnetic resonance observed in the photovoltage spectrum. **a,** V_{dc} measured using an excitation field at 17 GHz and $\varphi = 90^{\mathrm{o}}$ (green circles). The black solid line is the fitted results according to Equation 2.25. **b,** The symmetric and anti-symmetric Lorentzian components deduced from the fitting.

The two components of the FMR peak (symmetric and anti-symmetric Lorentzian) are shown in Figure 3.5b. They are calculated from the fitted results to Equation 2.25. For an out-of-plane driving field $\mathbf{h}_{\mathrm{mw}} = (0, 0, h_z)e^{i\omega t}$, Equation 2.26 and 2.27 predicts that the FMR peak should contain a simple symmetric Lorentzian lineshape, and $V_{\mathrm{asy}} \to 0$, and this is indeed observed. However a small anti-symmetric Lorentzian component does exist. It is attributed to the phase difference ψ between the Eddy current and the driving field, caused by non-uniformity of the device and parasitic capacitive coupling between the waveguide and the micro-bar. This effect is described in Ref. [80, 83] using the following expression:

$$V_{\mathrm{dc}} \propto V_{\mathrm{asy}} \cos\psi + V_{\mathrm{sym}} \sin\psi \tag{3.1}$$

For the FMR signal shown in Figure 3.5, the phase shift is estimated to be $\psi = -22^{\mathrm{o}}$, i.e. the current leads the driving field by 22°.

Magnetic resonance condition Different frequencies are also used to excite magnetic resonance in Device A. Figure 3.6a plots the magnetic field sweep curves for $\mathbf{h}_{\mathrm{mw}}$ at 12, 17 and 19 GHz. In each case the FMR peak is clearly visible in the photovoltage spectrum, and agrees well with Equation 2.25 (solid lines are the fitted results). The figure also demonstrates that the resonance field H_{res} increases with frequency. This can be understood by examining the condition for ferromagnetic resonance described in Equation 2.20.

Note that in this experiment, the resonance field H_{res} (a few hundreds of mT) is much larger than the saturation magnetisation of the material (a few tens of mT), hence the magnetisation vector $\mathbf{M}$ is always collinear with the applied field $\mathbf{H}_0$. Moreover, since $\mathbf{H}_0$ is only applied in-plane with the sample (i.e. $\theta = 90^{\mathrm{o}}$), the magnetic resonance condition can be simplified to:

$$\left(\frac{\omega}{\gamma}\right)^2 = \mu_0^2 (H_{\mathrm{res}} + H_1)(H_{\mathrm{res}} + H_2) \tag{3.2}$$

with

$$H_1 = M_{\mathrm{eff}} + \frac{H_{4\parallel}}{4}(3 + \cos 4\varphi) + H_{2\parallel} \cos^2\left(\varphi + \frac{\pi}{4}\right) + H_U \sin^2\varphi \tag{3.3}$$

$$H_2 = H_{4\parallel} \cos 4\varphi - H_{2\parallel} \sin 2\varphi - H_U \cos 2\varphi \tag{3.4}$$

where H_U represents the additional uniaxial anisotropy caused by patterning-induced strain-relaxation. $H_U > 0$ if its easy axis is along [010].

The frequency-dependence of $H_{\rm res}$ is fitted[1] to Equation 3.2 using a gyromagnetic constant characteristic for the Mn^{2+} spins $\gamma = 176$ GHz/T (g-factor 2). The fitted curve is shown as the red solid line in Figure 3.6b. The good agreement between the measured $H_{\rm res}(f)$ data and Equation 3.2, together with the good agreement between individual FMR peak and Equation 2.25, prove that the peaks detected in the photovoltage spectra indeed come from the coherent precession of Mn spins.

FMR linewidth The FMR linewidth ΔH (half width at half maximum) is plotted in Figure 3.6c. It is generally decomposed into a frequency-independent inhomogeneously-broadened part and an intrinsic damping-related part [74]:

$$\Delta H = \Delta H_{\rm inhomo} + \Delta H_{\alpha} = \Delta H_{\rm inhomo} + \frac{\alpha\omega}{\gamma} \tag{3.5}$$

with α being the dimensionless Gilbert damping constant. Fitting $\Delta H(f)$ to a straight line yields $\Delta H_{\rm inhomo} = 27.5$ mT and $\alpha = 0.04$. These values are comparable with an early electrical FMR study on micron-scale (Ga,Mn)As Hall bars with 2% Mn ($\Delta H_{\rm inhomo} = 20$ mT, $\alpha = 0.021$) [87].

Comparing with theoretical studies on the magnetisation relaxation in (Ga,Mn)As [132, 133], the value of the α deduced from the experimental data agrees within theoretical predications. For example, for (Ga,Mn)As wafers with 2% Mn, hole density of 1 $\rm nm^{-3}$ and quasiparticle lifetime broadening of 50 meV, α is calculated to be 0.04 [132]. In another study, $\alpha \approx 0.01$ is derived for a (Ga,Mn)As film with 5% Mn doping and full hole polarisation [133]. However, the carrier density in Device A has not been characterised,

[1]The fitted lines appeared in Figure 3.6b and Figure 3.7c are calculated by fitting to *all* the in-plane measurement data (taken at different driving frequencies and field angles) simultaneously using Equation 3.2. This is because the f-dependence of $H_{\rm res}$ can be used to accurately determine γ, while the φ-dependence of $H_{\rm res}$ reveals the magnetic anisotropy; and by combining both sets of data, all the micromagnetic parameters of the sample can be deduced.

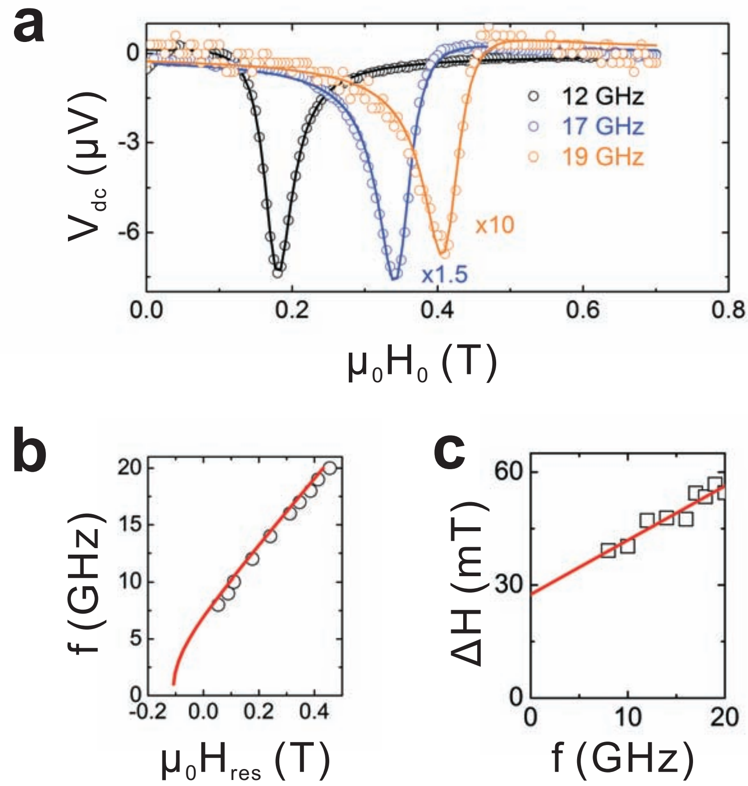

Figure 3.6: Frequency-dependence of the FMR signals. **a,** Photovoltage V_{dc} measured (circles) for $\mathbf{h}_{\mathrm{mw}}$ at 3 different frequencies (12, 17 and 19 GHz). The solid lines are fitted results. The amplitudes of the resonance peaks vary due to the frequency-dependent loss in the microwave circuit. **b,** Frequency-dependence of the resonance field H_{res} (black circles). The red solid line is the fitted results according to Equation 3.2, using a gyromagnetic constant $\gamma = 176$ GHz/T. **c,** Frequency-dependence of the FMR linewidth ΔH (black squares). The data are fitted to a straight line.

and more work is needed for a more reliable comparison between experiment and theory.

3.3.2 Mapping the anisotropy in the nanodevices

A main purpose of conventional FMR spectroscopy is to accurately determine the magnetic anisotropy constants. Here it is demonstrated that the on-chip driven FMR enables studying the *local* anisotropy in individual microdevices. Figure 3.7a plots the photovoltage spectra measured on Device A by sweeping $\mathbf{H}_0$ along different crystalline orientations ([110], [100] and [1$\bar{1}$0] directions, respectively). The magnitude of H_{res} is observed to be φ-dependent. This is understandable from Equation 3.2: Resonance in ferromagnetic systems occurs due to the effective magnetic field H_{eff}, which is a combination of the external and internal fields. As the internal field (predominantly the anisotropy field) varies with φ, so is the applied field H_{res} at which steady-state motion of $\mathbf{M}$ occurs.

Figure 3.7b shows the full photovoltage spectra from an in-plane rotational scan of $\mathbf{H}_0$. The FMR signal can be clearly recognised on top of a non-resonant background. Several characteristics of the magnetic anisotropy in this micro-device can be observed:

- The φ-dependence of H_{res} exhibits a pronounced fourfold symmetry, with minima in the [100] and [010] crystal directions. This can be explained by the intrinsic biaxial anisotropy term $H_{4\parallel}$, with easy axes along these directions.

- $H_{\mathrm{res}}(\varphi)$ also comprises a twofold symmetry, with H_{res} reaching maxima along [1$\bar{1}$0], while being smaller along [110]. This is caused by the intrinsic uniaxial anisotropy $H_{2\parallel}$, showing an easy axis along [110] and a hard axis along [1$\bar{1}$0]. $H_{2\parallel}$ usually has its easy axis along [1$\bar{1}$0], as reported in many experimental studies [10, 65, 74]; however, there have been observations on the rotation of $H_{2\parallel}$ towards [110] in annealed samples [110].

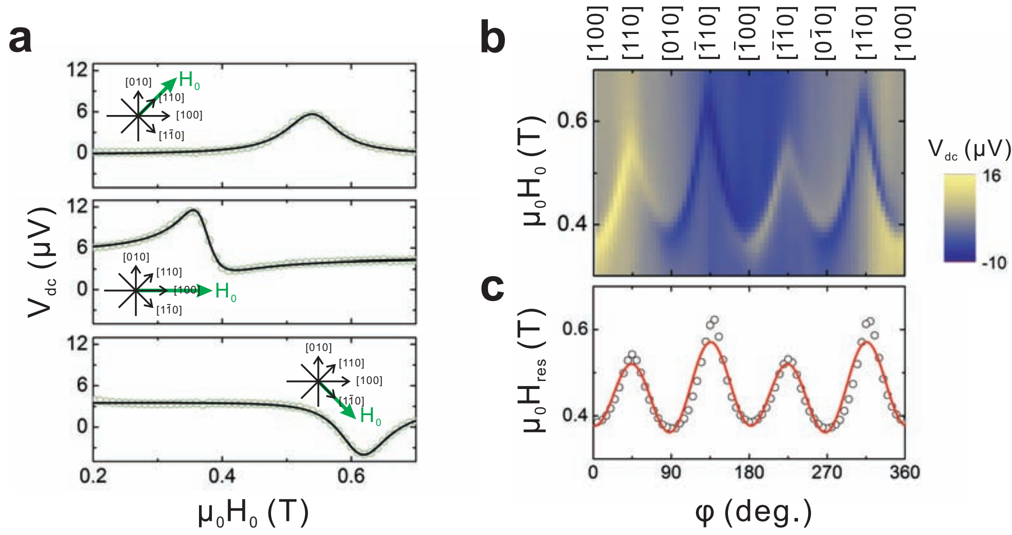

Figure 3.7: Probing the magnetic anisotropy in (Ga,Mn)As microstructures using on-chip driven FMR. **a,** V_{dc} measured when $\mathbf{H}_0$ is swept in-plane along [110], [100] and [1$\bar{1}$0], respectively. The inset pictures show the direction of the field sweep. A 18 GHz microwave field is used. **b,** The full photovoltage spectra for an in-plane rotational scan of $\mathbf{H}_0$. The colour scale represents the magnitude of V_{dc} (in μV). **c,** φ-dependence of the resonance field H_{res} (black circles). The red solid line is the fitted results according to Equation 3.2. The in-plane magnetic anisotropy constants H_i can be deduced from the fitting.

- A closer examination reveals that H_{res} along [100] is smaller than that along the [010] direction. However, according to the intrinsic biaxial anisotropy $H_{4\parallel}$, these axes should be equivalent. This indicates the existence of an additional uniaxial anisotropy H_U not present in the bulk (Ga,Mn)As epilayer. It is in fact due to strain-relaxation caused by the lithographic patterning process (Section 2.2.3). H_U has a twofold symmetry with an easy axis along the [010] direction, i.e. the direction of the micro-bar, and a hard axis along the direction of strain-relaxation. This is consistent with previous experiments on similar compressively-strained (Ga,Mn)As wafers [26, 65–67].

To deduce the in-plane magnetic anisotropy constants H_i from the FMR

results, the values of $H_{\rm res}$ are extracted by fitting to individual resonance peaks in Figure 3.7b using Equation 2.25. The φ-dependence of $H_{\rm res}$ is plotted in Figure 3.7c (black circles). A least square fitting algorithm is used to fit the experimentally obtained $H_{\rm res}$ data to Equation 3.2 (the red solid line), and the anisotropy fields are found to be: $\mu_0 H_{4\|} = 117$ mT, $\mu_0 H_{2\|} = -30$ mT, and $\mu_0 H_U = 9.3$ mT (with easy axis along the [010] direction).

One important remark for the on-chip driven FMR experiment is that the geometry of the bond pads has not been designed perfectly and this has led to two problems:

- Since the strength of the magnetic field generated by the shorted waveguide drops as $1/d^2$, where d is the distance away from the centre of the short[1] (Biot-Savart law), the large amount of magnetic moments in the bond pad region are driven by $\mathbf{h}_{\rm mw}$ with varying strengths, and their collective motion can no longer be considered as due to a single macrospin $\mathbf{M}$. This nonuniform motion of spins obscures the FMR peak detected across the device, and could lead to broadening of the linewidth ΔH.

- The magnetic anisotropy measured in the FMR experiment is an average over the entire (Ga,Mn)As device, i.e. micro-bar + bond pads. But since the bond pads exhibit bulk-like magnetic properties due to their large size, the change in magnetic anisotropy in the microstructures due to strain-relaxation can be overshadowed. The imperfect match between the experimental (black circles) and calculated (the red line) results in Figure 3.7c may be a result of this.

Since Device A only contains 3% of Mn, the compressive-strain caused by lattice mismatch is small, and the strain-relaxation-induced anisotropy H_U is negligible compared to the intrinsic anisotropy fields $H_{4\|}$ and $H_{2\|}$. For the same reason, H_U is expected to be more significant in (Ga,Mn)As

[1] According to the Biot-Savart law, the magnetic field h generated by the shorting-wire (with length L) varies as $\mu_0 h = [\mu_0 I/(2\pi d)](L/\sqrt{L^2+d^2})$. Hence it drops as 1/d for $d \ll L$, and as $1/d^2$ for $d \gg L$.

nano-devices with 6% Mn (Device B and C), as the wafer is under more compressive-strain. The measurement data are presented in the Appendix of this Chapter (Section 3.5). However, the influence from the bond pads is more pronounced in these devices. A new design is used in the subsequent experiments described in this Thesis, which resolves this issue by using symmetric bond pads fully covered with metal (Cr/Au) contacts, hence minimising their contribution to the measured signals.

3.3.3 Vector magnetometry using FMR

Following the discussions in Section 2.4.3, the lineshape of the photovoltage is determined by the direction and magnitude of the driving field. For an out-of-plane excitation field $\mathbf{h}_{\text{mw}} = (0, 0, h_z)e^{i\omega t}$, the FMR peak should have the shape of a symmetric Lorentzian function, with its amplitude changing with ϑ according to (cf. Equation 2.26):

$$V_{\text{sym}}(\vartheta) \propto \sin 2\vartheta \tag{3.6}$$

This has indeed been observed in Device A (Figure 3.8). In the experiments described in the next Chapter, this vector magnetometry method by considering the lineshape of the photovoltage is employed to analyse the direction and magnitude of an unknown driving field $\mathbf{h}_{\text{mw}}$ caused by the current-induced torque.

3.3.4 Effects of annealing

As introduced in Section 2.1.2, annealing (Ga,Mn)As wafers at moderate temperatures can remove the interstitial Mn_I defects and improve the homogeneity of the material. It has been observed in bulk (Ga,Mn)As films that annealing leads to better defined FMR signals with narrower linewidths [73, 74].

In Device B, the impacts of annealing on the inhomogeneous broadening term ΔH_{inhomo} and the Gilbert damping constant α have been investigated. Figure 3.9a compares the change in FMR lineshapes before and after the sample has been annealed, using the same excitation frequency of 17 GHz. The

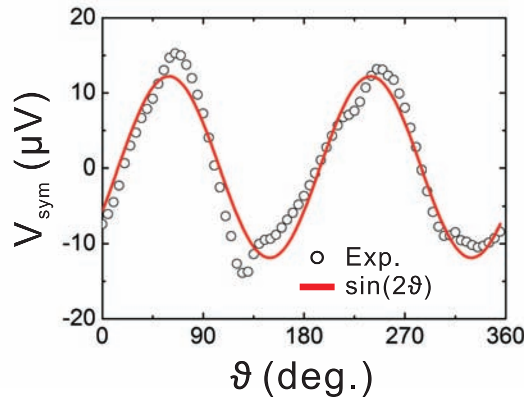

Figure 3.8: ϑ-dependence of the amplitude of the symmetric Lorentzian V_{sym} (black circles). The red solid line is fitting to a $\sin(2\vartheta)$ function. The shift which appears in the data (i.e. $V_{\mathrm{sym}}(\vartheta = 0^{\mathrm{o}}) \neq 0$) is due to sample misalignment (estimated to be $< 2^{\mathrm{o}}$) and a uniaxial crystalline AMR term C_U associated to the 3% (Ga,Mn)As wafer (for more details, see Section 4.5.3).

sharper lineshape and reduced width in the FMR signal from the annealed sample can be easily spotted. The resonance field H_{res} is also shifted, which indicates changes in the magnetic anisotropy upon annealing (discussed in details in Section 4.5.5).

Figure 3.9b quantitatively compares the frequency dependence of the FMR linewidth in the as-grown and annealed samples. Firstly, the overall FMR linewidth ΔH is smaller in the annealed device, than in the as-grown device under the same excitation frequency. Fitting the data to straight lines also reveals that the broadening due to wafer inhomogeneity $\Delta H_{\mathrm{inhomo}}$ halves upon annealing, reducing from 7.15 mT to 3.15 mT. The Gilbert damping constant α also decreases from 0.019 to 0.012[1]. All observations confirm that annealing helps to improve sample homogeneity and leads to more uniform precession of Mn ions.

[1]The Gilbert damping constant α in Device B is found to be smaller than that in Device A, even in the as-grown state. This is because the FMR linewidth scales approximately inversely with the carrier (hole) concentration p of the material, i.e. $\Delta H \approx p^{-1}$ [76].

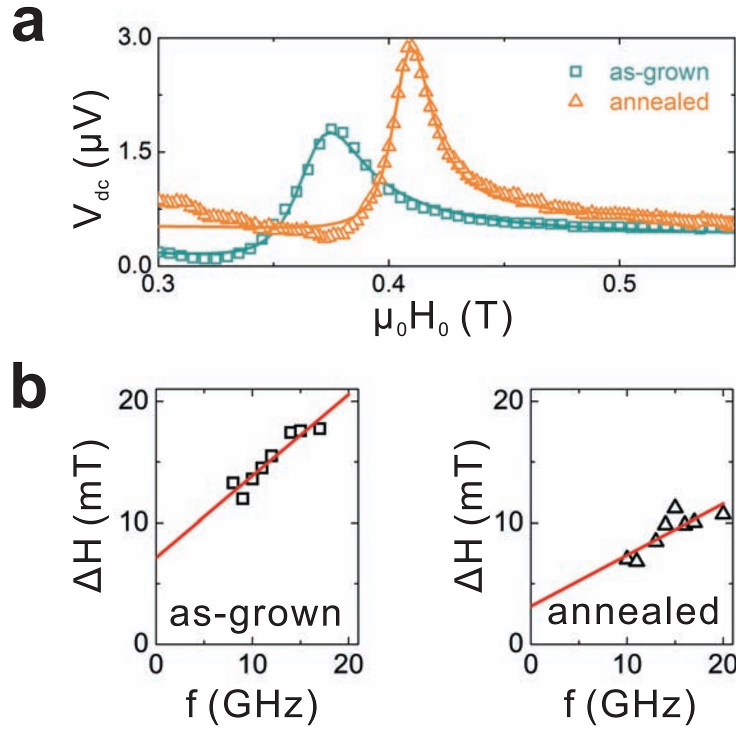

Figure 3.9: **a,** The FMR peak measured on Device B before and after it has been annealed (cyan squares and orange triangles, respectively), using the same excitation frequency of 17 GHz. The solid lines are fitted data according to Equation 2.25, from which the FMR linewidth can be determined. **b,** Comparison of the frequency-dependence of ΔH between the as-grown and annealed states of the device (black squares and triangles, respectively). The data are fitted to straight lines to extract $\Delta H_{\mathrm{inhomo}}$ (intercept) and α (gradient).

3.4 Conclusions

In this experiment, an all-electrical, on-chip driven FMR technique has demonstrated. It allows investigation on the magnetic properties of individual (Ga,Mn)As microstructures. In particular, the additional uniaxial anisotropy caused by patterning-induced strain-relaxation is observed, which has an easy axis perpendicular to the direction of strain-relaxation.

Furthermore, FMR in these microdevices gives rise to a dc photovoltage due to an AMR frequency-mixing effect, whose amplitude reflects the characteristics of the microwave driving field (orientation and magnitude). It has been confirmed that the observed angle-dependence of the FMR amplitude agrees with the mathematical predictions for an out-of-plane driving field. This vector magnetometry technique is used in the following Chapter to investigate an unknown excitation field.

However, the true FMR peaks and the magnetic anisotropy of the microstructures are obscured by the magnetic elements in the bond pad region. This issue is addressed in the experiments in the following Chapters (see also Section 3.5).

3.5 Appendix – Bond pad design

Figure 3.10a shows the photovoltage spectra from an in-plane rotational scan on Device C, together with a schematic of the device geometry. FMR measurements exhibits a profound fourfold symmetry in $H_{\text{res}}(\varphi)$ corresponding to the intrinsic biaxial anisotropy $H_{4\parallel}$ (82 mT). Fitting to the resonance field H_{res} using Equation 3.2 reveals that there is also an additional uniaxial anisotropy due to patterning-induced strain-relaxation, $\mu_0 H_U = -8$ mT, where the negative sign implies that H_U has an easy axis along the [100] direction, i.e. the long axis of the micro-bar.

However, the magnitude of H_U is much smaller than those reported in other studies on similar (Ga,Mn)As devices, due to the bulk anisotropy from the large bond pads of Device C, as suggested in Section 3.3.2. For example, Hoffmann *et al.* have measured devices on a (Ga,Mn)As wafer with 6% Mn (50 nm-thick film) and have observed $K_U = 1.8 \times 10^4$ erg/cm^3 (equivalent to $\mu_0 H_U = 47.6$ mT) on a 400 nm-wide bar [67]. For narrower bars (200 nm-wide), Hümpfner *et al.* and Wenisch *et al.* show that $\mu_0 H_U$ in (Ga,Mn)As epilayers with lower Mn concentrations (4% and 2.5% respectively) is a few tens of mT (25 and 45 mT respectively) [65, 66].

To illustrate the impact of the bond pads on the overall magnetic anisotropy, measurement data from a micro-bar with a new bond pad geometry are also presented here. The new bond pads are squared-shaped, so that their resistance is exactly 1/20 the resistance of the micro-bars (which contain 20 squares). The size of the metal contacts (Cr/Au) are also enlarged to cover almost the entire bond pads. Furthermore, the magnetisation precession is driven by a more uniform[1] $\mathbf{h}_{\text{mw}}$. Figure 3.10b shows the new geometry together with the results from a rotational field scan on such a device.

The magnetic anisotropy in the device with new bond pad geometry clearly exhibits a superposition of fourfold and twofold symmetry (due to

[1]FMR in this device is driven by the current-induced torque (CIT) instead of the torque from a local microwave magnetic field. The CIT-FMR technique is the focus of Chapter 4.

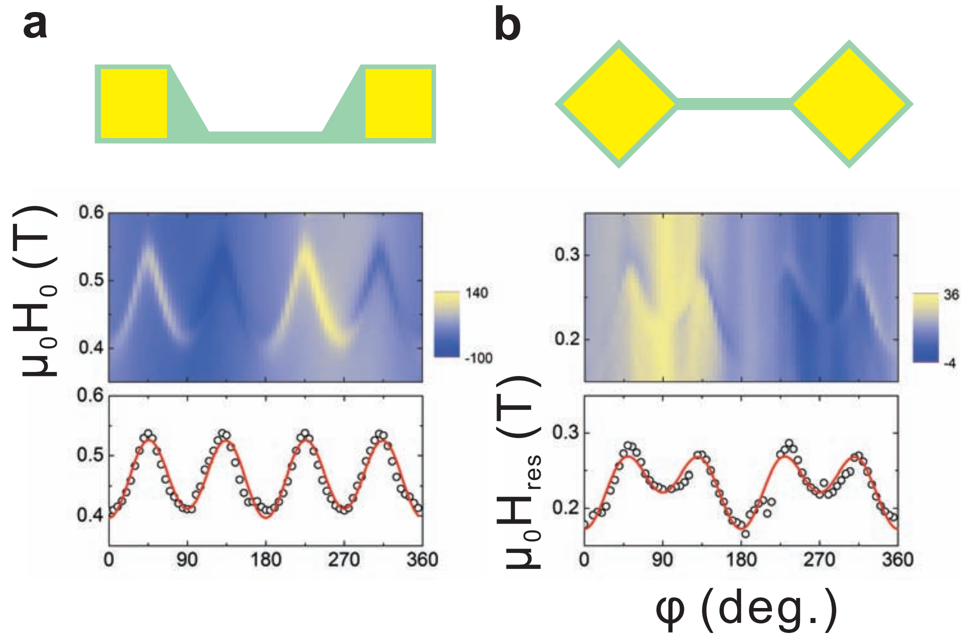

Figure 3.10: Magnetic anisotropy measured from FMR experiments in two micro-bars with different bond pad geometries. Both devices are patterned on the same ($Ga_{0.94}$,$Mn_{0.06}$)As wafer (as-grown) and are both along the [100] crystalline direction. The two devices have identical dimensions (500 nm-wide, 10 μm-long), but with different bond pad designs: **a,** The geometry of Device C and its magnetic anisotropy profile; **b,** A new device design and the magnetic anisotropy measured on such a device. The schematics are not-to-scale. In each case, the resonance field H_{res} (black circles) is fitted with Equation 3.2 (red solid lines).

$H_{4\parallel}$ and H_U, respectively), with $\mu_0 H_{4\parallel} = 43$ mT and $\mu_0 H_U = -28$ mT, consistent with earlier studies [65–67]. This demonstrates that the bond pads in the first design have obscured the true magnetic anisotropy in the microbars. The second device geometry has since been adopted in the following chapters.

Chapter 4

Ferromagnetic resonance driven by current-induced torque in magnetic microstructures

4.1 Introduction

Torques exerted on a ferromagnet by static or alternating magnetic fields induce magnetisation switching or ferromagnetic resonance (FMR) which are fundamental phenomena utilised in magneto-electronic applications as well as basic studies of magnetic systems. As introduced in Chapter 1, a major aim in spintronics research is to find replacement for the role of the magnetic field in these processes.

The discovery of spin-transfer torque (STT) offers such an opportunity [17–19]. STT is a collective quantum phenomenon in which a spin-polarised electric current acts on spatially varying magnetisation via exchange interaction and, in a simplified picture, can be viewed as a macroscopic angular momentum transfer effect. Similar to the phenomenon itself, the detection of the spin-transfer torque is commonly performed by magneto-transport effects, such as the tunnelling magnetoresistance (TMR), which rely on the ferromagnetic exchange interaction and non-uniformity of the magnetic structure.

In a uniformly magnetised system, the current-induced torque (CIT) is a result of the internal exchange field combined with a microscopic non-collinearity of individual electron spins which originates from the relativistic spin-orbit coupling. When an electric current traverses through materials with a specific broken symmetry[1] in their spin-orbit coupled band-structure, a non-equilibrium spin polarisation of the carriers occurs [42, 49, 134]. It produces a transverse component of the internal exchange field and a torque is applied to the magnetisation vector [38, 40].

In this Chapter, a microwave frequency CIT is realised in magnetic microstructures and is utilised to electrically drive FMR. For detection the anisotropic magnetoresistance (AMR) effect is employed, which, similar to CIT, is a combined exchange and spin-orbit coupling phenomenon present in uniform ferromagnets. The III–V diluted magnetic semiconductors (Ga,Mn)As and (Ga,Mn)(As,P) are particularly favourable systems for observing and exploring CIT-FMR because of their compatibility with advanced semiconductor micro-fabrication techniques, because the carrier bands have strong spin-orbit coupling and strong exchange interaction with the localised magnetic moments, and because the system can be described by a common, model semiconductor Hamiltonian.

4.2 Devices and experimental methods

Device preparation 25 nm-thick (Ga_{1-x},Mn_x)As and (Ga_{1-x},Mn_x)(As_{1-y},P_y) wafers have been used in this experiment. They are prepared using LT-MBE by Richard Campion, Arianna Casiraghi and coworkers at the University of Nottingham. (Ga,Mn)As wafers with different Mn concentrations have been used (3%, 6% and 12%), and the (Ga,Mn)(As,P) wafers contain 6% Mn and 10% P.

Devices of two different sizes are fabricated: 40 μm $\times$ 4 μm and 10 μm $\times$ 0.5 μm (Figure 4.1b and 4.1c). In the first fabrication step, the micro-bars are defined on the ferromagnetic films with isolation trenches (200 nm-wide,

[1] The two types inversion asymmetry exploited in these experiments are bulk inversion asymmetry (BIA) and structural inversion asymmetric (SIA).

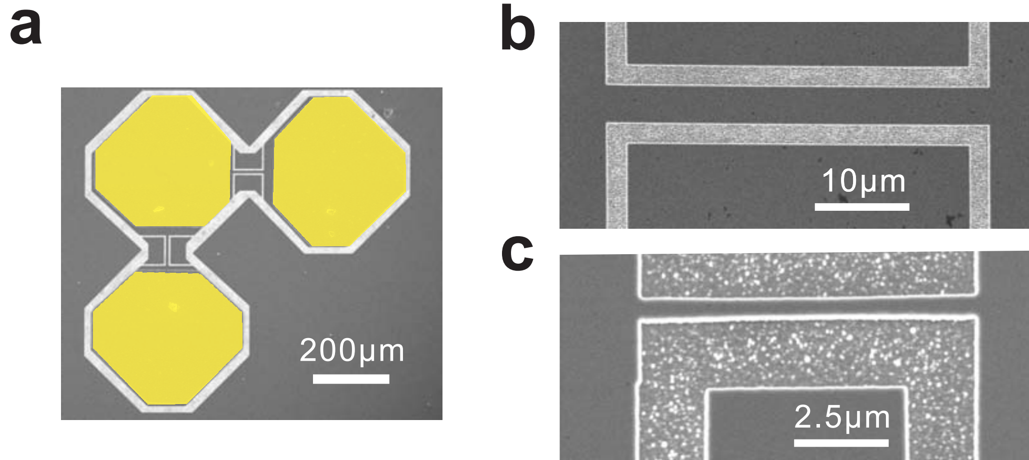

Figure 4.1: SEM images of the devices used in this experiment. a, The SEM image of a sample chip, which contains two micro-bars patterned 90°-apart. The Cr/Au ohmic contacts are highlighted in yellow false colour. **b** and **c,** SEM graphs of individual 4 μm- and 500 nm-wide bars.

$\sim$ 150 nm-deep), created with e-beam lithography and reactive ion etching. The Cr/Au (20/200 nm-thick) ohmic contacts are made in a second step of photolithography and evaporation. The full recipe for the device fabrication is given in Appendix C. Each sample chip contains two micro-bars, patterned 90°-apart along different crystallographic axes and sharing a common signal input. Figure 4.1a shows a SEM image of a typical sample.

Measurement technique A schematic of the experimental setup is shown in Figure 4.2a. The same sample carrier shown in Figure 3.2 is used. The device is wire-bonded between the open-circuit coplanar waveguide and a low-frequency connection which also provides a microwave ground (with parasitic capacitance $\sim$ pF). Due to the large impedance mismatch[1], most of the incident signal is reflected, however a small microwave current $I\cos(\omega t)$ still flows through the sample (a few tens of μA). Within the ferromagnet, the oscillating current-induced torque causes the magnetisation $\mathbf{M}$ to precess,

[1] A 4 μm-wide bar has nominal resistance $\sim$ 10 kΩ, whereas the microwave transmission line and coplanar waveguide have characteristic impedance of 50 Ω.

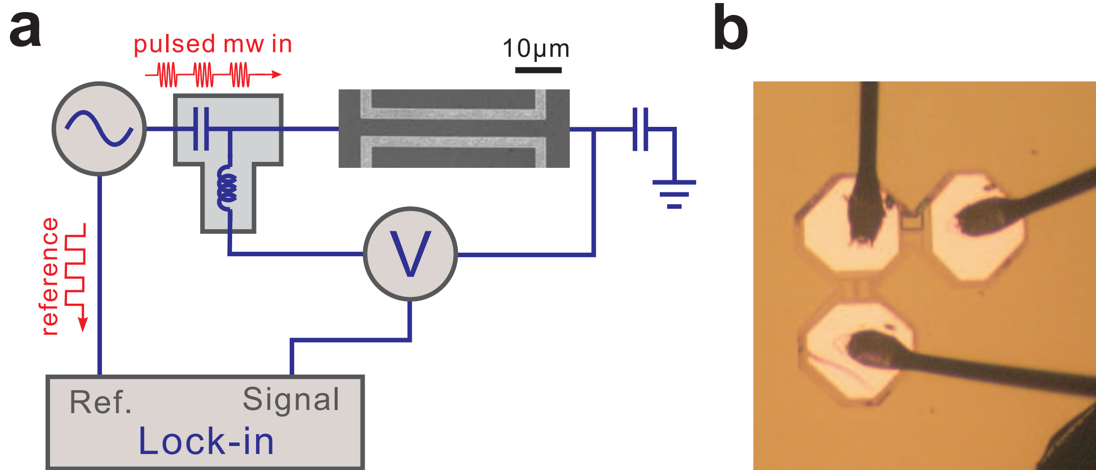

Figure 4.2: **a,** Schematic of the CIT-FMR experiment setup (not-to-scale). **b,** Micrograph of a prepared sample.

which leads to time-dependent change in the resistance. This, when combined with the microwave current inside the device, produces a measurable dc photovoltage from the frequency mixing effect (Section 2.4.3).

The lock-in measurement technique introduced in Section 3.2.3 is also employed in the CIT-FMR experiments. A bias-tee is used to isolate the low-frequency modulated photovoltage (987.6 Hz) from the microwave frequency voltage from the signal generator (GHz). The potential difference across the device is measured with a voltage preamplifier (differential mode, the signals are amplified by 500 times). The measurements are carried out in the same cryogenic system described in Chapter 3, at a constant temperature of 6 K.

4.3 Data and analysis

A total number of 61 devices have been measured, and consistent observations have been made. Representative data are presented in this Section.

4.3.1 Current-induced torque driven FMR

Magnetic resonance signal Figure 4.3a shows the photovoltage measured across a (Ga,Mn)As micro-bar (4 μm-wide, $[1\bar{1}0]$ direction), as the external field $\mathbf{H}_0$ is swept while a fixed-frequency microwave current $I\cos\omega t$ is applied. V_{dc} measured at different microwave frequencies are shown. In each case, a well-defined peak can be recognised from the photovoltage spectrum, which can be well-fitted by the solution of the LLG equation (Equation 2.25). The resonance field H_{res}, and amplitudes of the Lorentzian functions V_{sym} and V_{asy} are then determined from the fittings.

Figure 4.3b plots the frequency-dependence of the resonance field H_{res}. Fittings to Equation 3.2 suggest that $H_{\mathrm{res}}(f)$ can be well-described by the ferromagnetic resonance condition. A gyromagnetic constant γ characteristic for Mn^{2+} spins 176 GHz/T (g-factor 2) is used for the fitting. This, together with the good agreement between the observed peaks and the fitted results from Equation 2.25, confirms that the observed peaks in Figure 4.3a are due to the coherent precession of Mn spins. Figure 4.4 illustrates the CIT-FMR process.

Comparing the lineshapes of the FMR signals in Figure 4.3a and those from the previous FMR experiment (Figure 3.6a), it is clearly recognised that the FMR peaks in Figure 4.3a are dominated by an anti-symmetric Lorentzian function, which is the signature of an in-plane driving field according to Equation 2.27. Further analysis described later in this Chapter confirms this observation.

Since the CIT-FMR experiment is performed over a wide range of frequencies, the inhomogeneous ($\Delta H_{\mathrm{inhomo}} = 1.5$ mT) and frequency-dependent (0.28 mT/GHz) contributions to the damping are also determined (Figure 4.3c). The Gilbert damping is found to be $\alpha = 0.008$ for this device (see Equation 3.5), consistent with theoretical predications [132, 133].

Mapping the magnetic anisotropy Conventional FMR spectroscopy is usually employed to measure the magnetic anisotropy. Here this functionality is also demonstrated using the CIT-FMR technique. In Figure 4.3d the

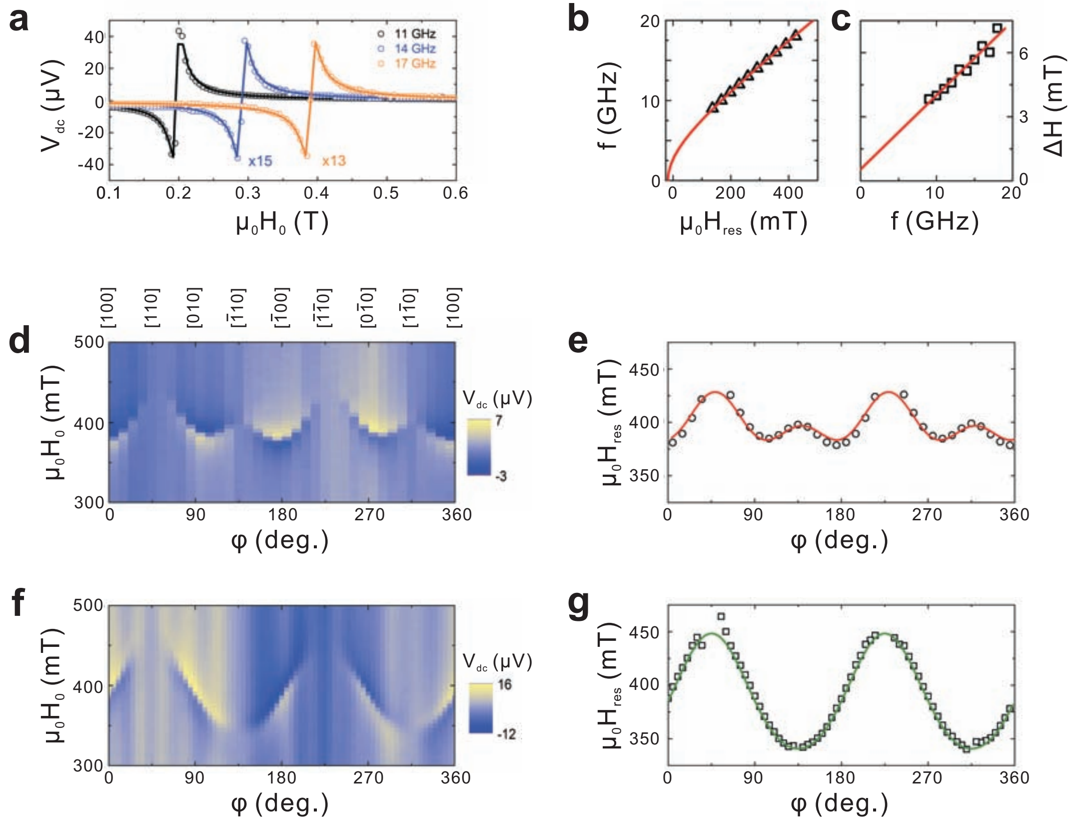

Figure 4.3: Microwave current-induced torque driven FMR. **a,** $V_{\rm dc}$ measured on a 4 μm-wide bar using $I\cos(\omega t)$ at 11, 14 and 17 GHz (circles). The resonance peaks are clearly observed and can be well-described by Equation 2.25 (the solid lines are fitted results). The difference in the signal strength at different ω is caused by the frequency-dependent attenuation of the microwave circuit. **b,** The resonance field $H_{\rm res}$ as a function of the microwave frequency (black triangles). The red line is the fitted results to Equation 3.2. **c,** Frequency-dependence of the FMR linewidth ΔH (black squares). The data are fitted to a straight line to extract information on the inhomogeneous broadening $\Delta H_{\rm inhomo}$ and Gilbert damping constant α. **d,** $V_{\rm dc}$ measured from in-plane rotational scans of $\mathbf{H}_0$. The colour scale represents the magnitude of the photovoltage. **e,** Angle-plot of $H_{\rm res}$ (black circles), which is extracted by fitting to each FMR peak using Equation 2.25. The red line is a fitted curve to Equation 3.2 for calculating the anisotropy fields. **f,** $V_{\rm dc}$ measured for in-plane rotational scans of $\mathbf{H}_0$ on a 500 nm-wide bar. **g,** Angle-plot of $H_{\rm res}$ for the 500 nm-wide bar with fittings.

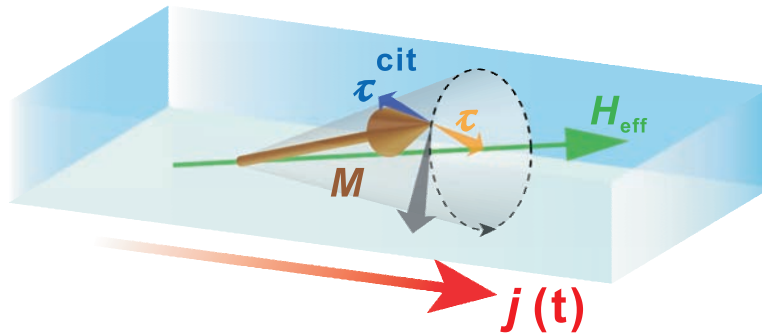

Figure 4.4: Concept of the current-induced torque driven ferromagnetic resonance (CIT-FMR). The current-induced torque (τ^{cit}) counters the effect of damping (τ^{α}), and leads to steady-state precession of the magnetisation: $\partial\mathbf{M}/\partial t = -\mathbf{M} \times \mathbf{H}_{\text{eff}}$.

data from an in-plane rotational scan of $\mathbf{H}_0$ are shown, which reveal both uniaxial ($H_{2\|}$), along the $[1\bar{1}0]$ direction, and biaxial ($H_{4\|}$) contributions to the anisotropy. By analysing the peak positions (Figure 4.3e) these values are found to be $\mu_0 H_{2\|} = 18.7$ mT and $\mu_0 H_{4\|} = 17.4$ mT.

The CIT-FMR technique is also used to measure a 500 nm-wide bar patterned in the same direction (Figures 4.3f and 4.3g), giving $\mu_0 H_{2\|} = 68.2$ mT and $\mu_0 H_{4\|} = 5.7$ mT. The enhanced uniaxial term along the bar demonstrates the effect of patterning-induced strain-relaxation on the magnetic anisotropy [26, 65–67]. This measurement shows the scalability of the CIT-FMR technique down towards the nanoscale.

4.3.2 Quantifying the current-induced torque

The key parameters of interest in this study are the direction and magnitude of the field $\mathbf{h}_{\text{cit}}$ producing the torque. These quantities can be deduced from the angle dependence of the FMR amplitudes V_{sym} and V_{asy}, which is described in Equations 2.25, 2.26 and 2.27 (Section 2.4.3). The measurement data analysed in this Section are from the 4 μm-wide devices.

Since no component of V_{sym} is observed to behave as $\sin(2\vartheta)$ within the

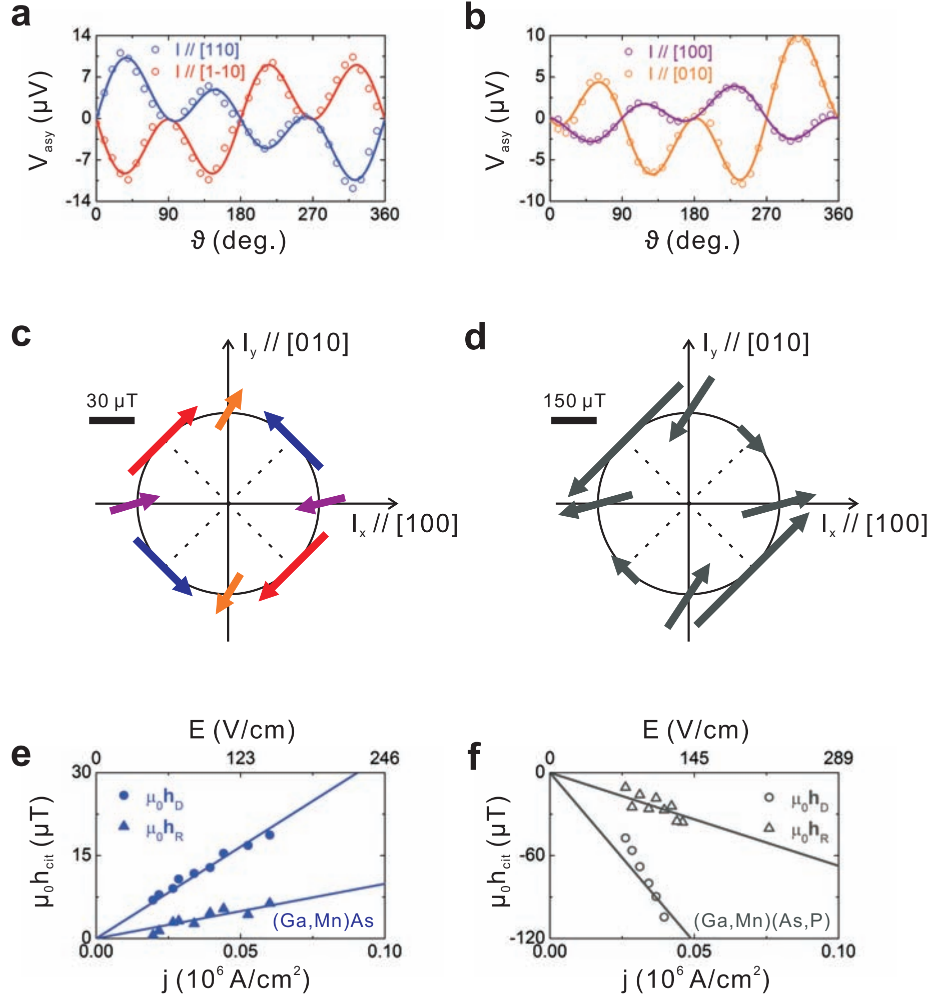

Figure 4.5: Characterisation of the current-induced field in (Ga,Mn)As and (Ga,Mn)(As,P) devices. **a–b,** Anti-symmetric Lorentzian amplitudes V_{asy} measured on a group of 4 μm-wide (Ga,Mn)As bars (circles), patterned along different crystalline directions. The solid lines are fitted results to Equation 2.27. **c,** Plot of the magnitude and direction of the current-induced field $\mathbf{h}_{\mathrm{cit}}$ measured in the (Ga,Mn)As micro-bars, scaled for a current density $j = 10^5$ A/cm^2. **d,** Similar plot for $\mathbf{h}_{\mathrm{cit}}$ measured in the 4 μm-wide (Ga,Mn)(As,P) devices. **e–f,** Current density dependence of $\mathbf{h}_{\mathrm{R}}$ (Rashba) and $\mathbf{h}_{\mathrm{D}}$ (Dresselhaus) in both (Ga,Mn)As and (Ga,Mn)(As,P) samples. A second horizontal scale is included for the electric field, calculated from the device resistance.

error of the measurements[1], it is concluded that the driving field $\mathbf{h}_{\mathrm{cit}}$ is predominantly in-plane. The discussions therefore focus on the amplitude of the anti-symmetric Lorentzian V_{asy}.

Figure 4.5a shows the angle dependence of V_{asy} for the (Ga,Mn)As device patterned in the $[1\bar{1}0]$ direction. By fitting to Equation 2.27, it is recognised that $V_{\mathrm{asy}}(\vartheta)$ comprises a $-\sin(2\vartheta)\cos(\vartheta)$ term, indicating that the driving field is perpendicular to $\mathbf{I}$, i.e. $\mathbf{h}_{\mathrm{cit}} = (0, -h_y, 0)e^{i\omega t}$. In a [110] device (Figure 4.5a) the amplitude of V_{asy} also depends on $\sin(2\vartheta)\cos(\vartheta)$ but has opposite sign, indicating that the driving field has reversed, i.e. $\mathbf{h}_{\mathrm{cit}} = (0, h_y, 0)e^{i\omega t}$. For the micro-bar along [100] (Figure 4.5b), the V_{asy} curve is a superposition of $\sin(2\vartheta)\sin(\vartheta)$ and $\sin(2\vartheta)\cos(\vartheta)$ functions. This implies that the driving field consists of components both parallel and perpendicular to $\mathbf{I}$, i.e. $\mathbf{h}_{\mathrm{cit}} = (-h_x, -h_y, 0)e^{i\omega t}$, with $h_x > h_y$. Similar observation is also made in a [010] sample, but with the field orientation: $\mathbf{h}_{\mathrm{cit}} = (h_x, -h_y, 0)e^{i\omega t}$.

Taken together these results indicate two contributions to the current-induced driving field with different symmetry, $\mathbf{h}_{\mathrm{cit}} = \mathbf{h}_{\mathrm{R}} + \mathbf{h}_{\mathrm{D}}$. The fields $\mathbf{h}_{\mathrm{R}}$ and $\mathbf{h}_{\mathrm{D}}$ have angular dependence on $\mathbf{I}$ reminiscent of the angular dependence of Rashba and Dresselhaus spin-orbit fields in the momentum space, respectively [44, 45] (cf. Figure 2.15). This is most clearly seen by plotting the dependence of the magnitude and direction of the resultant fields on the electric current (micro-bar) orientation (Figures 4.5c). From samples patterned in the [010] and [100] directions it is found that there exists a field $\mathbf{h}_{\mathrm{R}}$ always perpendicular to $\mathbf{I}$, having the symmetry of the momentum-dependent Rashba spin-orbit interaction. It is also evident that $\mathbf{h}_{\mathrm{R}}$ is present in the [110] and $[1\bar{1}0]$ micro-bars where it acts to either enhance or reduce the resultant $\mathbf{h}_{\mathrm{cit}}$. The main term, $\mathbf{h}_{\mathrm{D}}$ with symmetry of the Dresselhaus spin-orbit interaction, is parallel to $\mathbf{I}$ in the [010] and [100] directions, and perpendicular to $\mathbf{I}$ in the [110] and $[1\bar{1}0]$ directions.

The strength of $\mathbf{h}_{\mathrm{D}}$ is found to be linear with current density (Figure 4.5e) and its magnitude, scaled to $j = 10^5$ A/cm^2, is $\mathbf{h}_{\mathrm{D}} = 33$ μT. Note that the current density is determined by a bolometric effect, using the resistance to

[1] The ϑ-plots for the amplitude of the symmetric Lorentzian (V_{sym}) measured on these devices are presented in Section 4.5.1.

compare the heating effect of an unknown microwave current to a known direct current (see Section 4.5.2). The magnitude of $\mathbf{h}_{\mathrm{R}}$ is 10 μT at $j = 10^5$ A/cm^2 and this weaker component of the CIT field is also linear with current density (Figure 4.5e). These values of $\mathbf{h}_{\mathrm{D}}$ and $\mathbf{h}_{\mathrm{R}}$ are evaluated from a device in the [100] direction where $\mathbf{h}_{\mathrm{D}}$ and $\mathbf{h}_{\mathrm{R}}$ are orthogonal and can be separately determined.

4.3.3 Theoretical understanding on the current-induced torque

These observations are further analysed theorectically in collaboration with Karel Výborný, Liviu Zârbo and Tomas Jungwirth at the Institute of Physics, Czech Republic.

Microscopically, $\mathbf{h}_{\mathrm{D}}$ and $\mathbf{h}_{\mathrm{R}}$ can be linked to the term $\mathcal{H}_{\mathrm{C4}}$ in the effective Hamiltonian describing (Ga,Mn)As [39, 40, 61, 129, 135]:

$$\mathcal{H} = \mathcal{H}_{\mathrm{KL}} + \mathcal{H}_{\mathrm{exch}} + \mathcal{H}_{\mathrm{C4}} \tag{4.1}$$

Here $\mathcal{H}_{\mathrm{KL}}$ is the inversion symmetric part of the host GaAs semiconductor Hamiltonian, $\mathcal{H}_{\mathrm{exch}}$ describes the exchange interaction between carrier (hole) spins and local Mn moments, and the $\mathcal{H}_{\mathrm{C4}}$ term is due to broken inversion symmetry and the presence of strain (ε_{ij}).

Using the four-band Kohn-Luttinger Hamiltonian model [136], the inversion symmetric part $\mathcal{H}_{\mathrm{KL}}$ is written as:

$$\mathcal{H}_{\mathrm{KL}} = \frac{\hbar^2}{2m}\left[\left(\gamma_1 + \frac{5}{2}\gamma_2\right)k^2 - 2\gamma_3(\vec{k}\cdot\vec{J}\,)^2 + 2(\gamma_3 - \gamma_2)\sum_i k_i^2 J_i^2\right] \tag{4.2}$$

where $\gamma_1 = 6.98$, $\gamma_2 = 2.06$ and $\gamma_3 = 2.93$ are three independent Luttinger parameters, $\vec{J}$ is the carrier total angular momentum, and $\vec{k}$ is the wavevector.

The carrier (hole) – local moment exchange term reads:

$$\mathcal{H}_{\mathrm{exch}} = \frac{1}{3}h\mathbf{e}_M\cdot\vec{J} \tag{4.3}$$

where $h = J_{\mathrm{pd}}n_{\mathrm{Mn}}s_{\mathrm{Mn}}$ (J_{pd} is the exchange constant, n_{Mn} is the density of Mn local moments and $s_{\mathrm{Mn}} = 5/2$) and $\mathbf{e}_M$ is the magnetisation unit vector.

Finally, the term due to broken inversion symmetry and strain $\mathcal{H}_{\mathrm{C4}}$ is written as (cf. Equations 2.34 and 2.37):

$$\mathcal{H}_{\mathrm{C4}} = C_4[\varepsilon_{zz}(J_y k_y - J_x k_x) + \text{c.p.}] + C_4[\varepsilon_{xy}(J_x k_y - J_y k_x) + \text{c.p.}] \tag{4.4}$$

Here c.p. denotes cyclic permutations in $\{x, y, z\}$, which refer to components along the cubic axes of the crystal; and $C_4 \approx 0.5$ eVnm for the GaAs host [135]. The $\mathbf{h}_{\mathrm{D}}$ and $\mathbf{h}_{\mathrm{R}}$ components of $\mathbf{h}_{\mathrm{cit}}$ originate from the first and second bracket term in the $\mathcal{H}_{\mathrm{C4}}$ Hamiltonian (Equation 4.4), respectively.

The form of the strain tensor ε_{ij} therefore determines the $\mathbf{h}_{\mathrm{D}}$ and $\mathbf{h}_{\mathrm{R}}$ fields. For epitaxially-grown (Ga,Mn)As and (Ga,Mn)(As,P) films, the strain tensor reads [115]:

$$\varepsilon_{ij} = \begin{pmatrix} e_0 & 0 & 0 \\ 0 & e_0 & 0 \\ 0 & 0 & -2\dfrac{c_{12}}{c_{11}}e_0 \end{pmatrix} \tag{4.5}$$

Here the growth-strain is defined as $e_0 = (a_s - a_0)/a_0$, where a_s and a_0 are the lattice constants of the substrate and the magnetic film, respectively. Typical magnitudes are $e_0 \sim 10^{-4} - 10^{-2}$ [115]. The parameters c_{11} and c_{12} are the elastic moduli [137]. For positive (negative)[1] e_0, Equation 4.5 therefore describes an expansion (contraction) along the [100] and [010] crystal axes, accompanied by a contraction (expansion) along the [001] axis.

It is also clear from Equation 4.5 that the off-diagonal strain components (such as ε_{xy}) which yield the $\mathbf{h}_{\mathrm{R}}$ field are not physically present in the crystal structure of (Ga,Mn)As epilayers. This strain has been introduced, however, in previous studies to model the in-plane uniaxial anisotropy $H_{2\parallel}$ present in (Ga,Mn)As [26, 50, 110, 115]. It can be represented by a tensor:

$$\varepsilon_{ij} = \begin{pmatrix} 0 & \kappa & 0 \\ \kappa & 0 & 0 \\ 0 & 0 & 0 \end{pmatrix} \tag{4.6}$$

In this "intrinsic" shear strain, positive (negative) κ corresponds to turning a square into a diamond with the longer (shorter) diagonal along the [110]

[1] For epilayers under compressive-strain, such as (Ga,Mn)As grown on GaAs [95], $e_0 < 0$. For tensile-strained epilayers, such as (Ga,Mn)As grown on a relaxed InGaAs buffer [95] or (Ga,Mn)(As,P) [77], $e_0 > 0$.

axis. The fitted values of the intrinsic shear strain are typically several times smaller than the diagonal, growth-induced strain [115]. This is consistent with the observed smaller magnitude of $\mathbf{h}_\mathrm{R}$ than $\mathbf{h}_\mathrm{D}$ in the measurements (Figure 4.5e).

The $\mathcal{H}_{\mathrm{C4}}$ origin of the CIT is confirmed with measurements on 4 μm-wide bars patterned on the $(Ga_{0.94},Mn_{0.06})(As_{0.9},P_{0.1})$ epilayer, which has an opposite sign of e_0 compared with the $(Ga_{0.94},Mn_{0.06})As$ film [77, 92]. Consistently, the observed field $\mathbf{h}_\mathrm{D}$ also changes sign (Figure 4.5d and 4.5f).

The specific form of the the current-induced field $\mathbf{h}_{\mathrm{cit}}$ has also been derived by Karel Výborný and Liviu Zârbo. In the linear response regime of the experiment, it is written as [40]:

$$\mathbf{h}_{\mathrm{cit}} = -\frac{eEJ_{\mathrm{pd}}}{\mu_B}\tau \int \frac{d^3k}{(2\pi)^3} \sum_n \langle \vec{s}\,\rangle_{n,\mathbf{k}} \langle v_I \rangle_{n,\mathbf{k}} \delta(\varepsilon_{n,\mathbf{k}} - \varepsilon_F) \tag{4.7}$$

where τ is the transport relaxation time, $\langle \vec{s}\,\rangle_{n,\mathbf{k}}$ denotes the expectation value of the carrier spin, $\langle v_I \rangle_{n,\mathbf{k}}$ the velocity component along the current direction, $\varepsilon_{n,\mathbf{k}}$ are the eigenenergies of the Hamiltonian $\mathcal{H}$, and ε_F is the Fermi energy.

Therefore $\mathbf{h}_{\mathrm{cit}}$ is proportional to the applied electric field E (as demonstrated in Figure 4.5e and 4.5f), to the carrier – local moment exchange constant J_{pd} (≈ 55 meVnm^3 in (Ga,Mn)As [61]), to the transport relaxation time τ ($\hbar/\tau \approx 100$ meV [61]), and to the non-equilibrium spin-density due to the displaced Fermi surface given by the integral in Equation 4.7. For carrier density $p \approx 1$ nm^{-3}, the calculated CIT field (by Liviu Zârbo) at $E = 10^3$ V/cm is $|\mathbf{h}_\mathrm{D}| \approx 60$ μT, which is consistent with the experimental values.

A consequence of the $E\tau$-dependence of CIT revealed by Equation 4.7 is that a certain current density j would induce a smaller torque in a sample with higher carrier density[1] p. This can explain the different magnitude of

[1] According to the two expressions for current density: $j = \sigma E$ and $j = pev_d = pe\mu E$, where p is the carrier density, v_d is the drift velocity, and μ is the mobility, the electrical conductivity is found to be $\sigma = pe\mu \propto pe\tau$, where τ is the transport relaxation time and is approximately linearly proportional to the mobility μ. As a result, the current density $j = \sigma E \propto peE\tau$. i.e. at fixed j, the quantity $E\tau$ scales inversely with increasing carrier density p.

$\mathbf{h}_\mathrm{D}$ measured in (Ga,Mn)As and (Ga,Mn)(As,P) micro-bars (Figure 4.5e and 4.5f): the two materials are annealed at different conditions (190°C for 20 h for the (Ga,Mn)As wafer and 180°C for 48 h for the (Ga,Mn)(As,P) wafer) and even have different conductivity (typical resistance of 4 μm-wide bars is R_{xx} = 10 kΩ and R_{xx} = 11.5 kΩ for (Ga,Mn)As and (Ga,Mn)(As,P), respectively). However, the carrier density in the two wafers has not been measured, hence it is difficult at this stage to quantitatively described the different $\mathbf{h}_\mathrm{D}$ measured in the two materials.

4.3.4 Effect of strain on the current-induced torque

To further investigate the effect of strain on $\mathbf{h}_\mathrm{cit}$, two more experiments are performed on: (i) 500 nm-wide nano-bars fabricated on the (Ga,Mn)As and (Ga,Mn)(As,P) epilayers, in which strong strain-relaxation occurs due to lithographic patterning; (ii) 4 μm-wide micro-bars fabricated on (Ga,Mn)As epilayers with various Mn doping (3%, 6% and 12%), and thus different growth-strain.

Effect of strain-relaxation on CIT Figure 4.6a compares the magnitudes of $\mathbf{h}_\mathrm{D}$ and $\mathbf{h}_\mathrm{R}$ measured in both wide (4 μm) and narrow (500 nm) (Ga,Mn)As structures. Both fields exhibit linear dependence on j. However, it is observed that $\mathbf{h}_\mathrm{D}$ and $\mathbf{h}_\mathrm{R}$ are weaker in the 500 nm-wide samples. This can be understood qualitatively by considering the role of strain-relaxation. The first term in Equation 4.4 can be rearranged to become:

$$\mathcal{H}_{\mathrm{C4}} = C_4[(\varepsilon_{yy} - \varepsilon_{zz})J_x k_x + \mathrm{c.p.}] \tag{4.8}$$

In 4 μm-wide bars with minimal strain-relaxation, $\varepsilon_{yy} - \varepsilon_{zz} = e_0$. Now consider strain-relaxation in a nano-bar patterned along [100], i.e. the strain relaxes along [010], thus reducing $\varepsilon_{yy} - \varepsilon_{zz}$ and the total Hamiltonian in the system. Therefore for the same current density j, $\mathbf{h}_\mathrm{cit}$ becomes smaller in more strain-relaxed samples.

The influence of strain on $\mathbf{h}_\mathrm{cit}$ is further illustrated by the tensile-strained micro-bars patterned on $(\mathrm{Ga}_{0.94},\mathrm{Mn}_{0.06})(\mathrm{As}_{0.9},\mathrm{P}_{0.1})$ epilayers (Figure 4.6b):

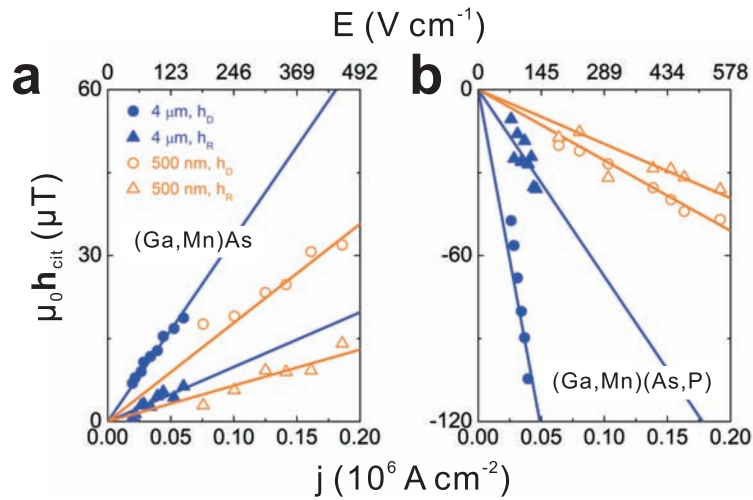

Figure 4.6: Magnitude of the current-induced field in 4 μm and 500 nm-wide bars. **a,** j- and E-dependence of $\mathbf{h}_\mathrm{D}$ and $\mathbf{h}_\mathrm{R}$ fields (circles and triangles respectively), measured on the 4 μm and 500 nm-wide $(Ga_{0.94},Mn_{0.06})As$ devices (blue and orange coloured respectively). The data are fitted to straight lines. **b,** Similar j- and E-dependence graphs for $\mathbf{h}_\mathrm{cit}$ measured in the $(Ga_{0.94},Mn_{0.06})(As_{0.9},P_{0.1})$ devices.

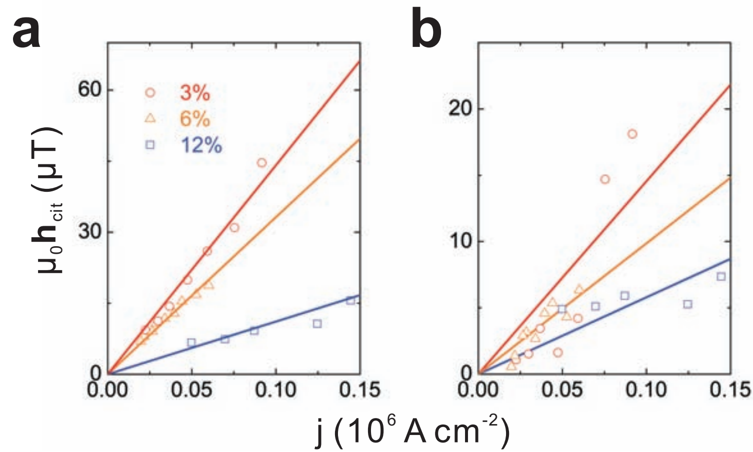

Figure 4.7: Current-induced field in 4 μm-wide (Ga,Mn)As structures with different Mn concentrations. **a,** j-dependence of $\mathbf{h}_\mathrm{D}$ in 4 μm-wide bars with 3%, 6% and 12% Mn. The data are fitted to straight lines. **b,** j-dependence of $\mathbf{h}_\mathrm{R}$ measured in the same devices.

Both $\mathbf{h}_\mathrm{D}$ and $\mathbf{h}_\mathrm{R}$ change sign compared with the compressively-strained (Ga,Mn)As devices; furthermore, $\mathbf{h}_\mathrm{cit}$ can still be reduced by introducing strain-relaxation via lithographic patterning.

Effect of Mn doping levels on CIT (Ga,Mn)As devices with different Mn levels (3%, 6% and 12%, respectively, in as-grown wafers) have also been studied in the experiment. Figure 4.7 presents the results measured on a group of 4 μm-wide bars fabricated from the different films.

Figure 4.7a shows that $\mathbf{h}_\mathrm{D}$ is linear in j. Moreover, the same current density is observed to induce the largest $\mathbf{h}_\mathrm{D}$ in samples with 3% Mn, and the induced field decreases with increasing Mn concentration. This is counter-intuitive at first glance: Samples with 12% Mn should have the largest growth-strain e_0 due to lattice mismatch, therefore Equation 4.8 predicts that $\mathbf{h}_\mathrm{cit}$ should be the strongest in these materials; whereas experimental observations suggest the opposite.

This apparent contradiction can be understood by considering the effect of increasing Mn concentration on the electrical properties of the magnetic

semiconductor. Since the carrier density p is higher in (Ga,Mn)As films with higher Mn doping, the quantity $E\tau$ in these samples becomes lower at a fixed current density j. As Equation 4.7 clearly suggests, the current-induced field scales linearly with $E\tau$, it is therefore not surprising for the (Ga,$Mn_{0.12}$)As micro-bar to have the lowest $\mathbf{h}_{\mathrm{cit}}$ among the three devices.

Similar to $\mathbf{h}_{\mathrm{D}}$, the field $\mathbf{h}_{\mathrm{R}}$ due to the Rashba spin-orbit coupling is also found to be lower in samples with higher Mn levels. In all 3 devices, $\mathbf{h}_{\mathrm{R}}$ is smaller than $\mathbf{h}_{\mathrm{D}}$, consistent with theoretical findings that the diagonal strain elements $\varepsilon_{xx,yy}$ dominate over the off-diagonal strain ε_{xy} [115].

4.3.5 Effect of an electrical bias on the FMR signals

It has been demonstrated in spin-valves and tunnel junctions, that a dc spin-polarised current can induce magnetic motion via the spin-transfer torque effect [23]. Furthermore, it has been observed that STT from the dc current can induce different types of magnetic excitation [23, 32, 33], and, when combined with a STT-FMR technique [34, 35], allows the spin-transfer "torkance"[1] to be accurately determined [63].

In the final experiment, both a direct and microwave frequency current are injected into a (Ga,Mn)As bar, and the photovoltage is measured[2] while sweeping $\mathbf{H}_0$. Preliminary analysis has revealed that the dc current alters the lineshape of the FMR signal, and this effect depends on the magnitude and direction of the current.

Figure 4.8a shows the evolution of the FMR peak as the dc bias current is varied. At $I_{\mathrm{dc}} = 0$, the FMR peaks is predominantly anti-symmetric resulting from the in-plane driving field. Upon the application of a dc current, the FMR lineshape is significantly altered and a large symmetric component V_{sym} appears. The magnitudes of both V_{sym} and V_{asy} are calculated from fittings according to Equation 2.25 and are plotted in Figure 4.8b. Bias currents

[1] The torkance is defined as $d\tau/dV$, where V is the dc bias voltage on the spin-valve or tunnel junction.

[2] Two high-pass filters with 100 Hz cut-off frequency are connected to each end of the voltmeter, so that only the modulated photovoltage (at 987.6 Hz) is measured. Without the filters, the large dc bias would overload the voltmeter.

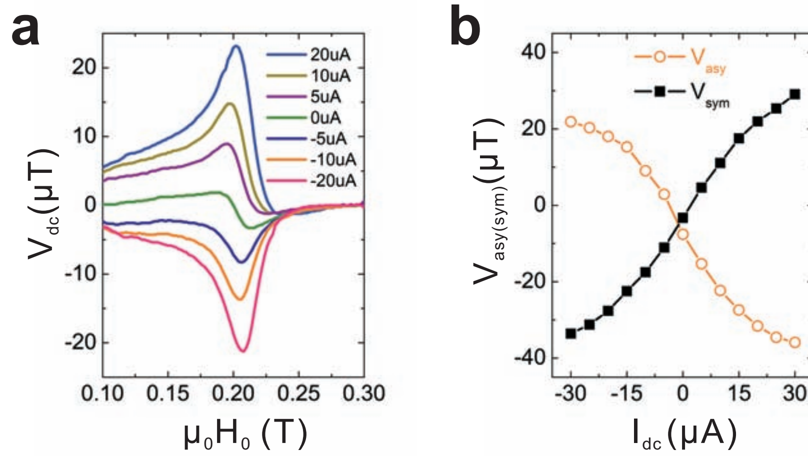

Figure 4.8: Effect of a direct current on the CIT-FMR signal. **a,** The modulated photovoltage V_{dc} measured under different bias currents. The FMR peak is clearly visible in each spectrum. A large current-dependent background is subtracted from V_{dc} before it is plotted. **b,** The bias-dependence of the symmetric and anti-symmetric Lorentzian components $V_{\mathrm{sym,asy}}$, deduced from fittings of each FMR peak in **a** according to Equation 2.25. The measurements are performed on a 350 nm-wide bar patterned on an as-grown $(Ga_{0.94},Mn_{0.06})As$ wafer. $\mathbf{H}_0$ is swept along $\vartheta = 225^{\mathrm{o}}$.

$I_{\rm dc}$ up to ± 30 μA have been applied, which corresponds to bias voltage of ± 2.55 V (the device has nominal resistance ~ 85 kΩ).

It has been observed in previous FMR experiments on permalloy that a dc bias current alters the amplitude of the FMR signal [80, 84, 85], due to a bias-dependent term in the time-varying current $I(t)$:

$$I(t) = I_{\rm mw} \cos \omega t + I_{\rm dc} \left(R(t)\right) \tag{4.9}$$

Here the first term in the expression of $I(t)$ is the microwave current inside the device; and the second term is caused by the oscillating resistance in the sample, and hence also varies at frequency ω. Following Ohm's law, this contribution to the FMR signal should scale linearly with $I_{\rm dc}$. This is indeed observed in Figure 4.8b, and the small nonlinearity at large biases (± 20 μA) can be attributed to heating. Furthermore, according to Ref. [80], the DC bias current creates FMR signals with symmetric Lorentzian lineshape (Figure 4.8b), with the amplitude $V_{\rm sym}$ varies as $\cos 2\vartheta$. It is therefore important in the next stage of the experiment to measure the ϑ-dependence of the observed $V_{\rm sym}$ component.

In addition to altering the FMR amplitude, a direct current can also generate a dc effective magnetic field $\mathbf{h}_{\rm cit}^{\rm DC}$, and this has been observed to shift the resonance position $H_{\rm res}$ in ESR experiments [57]. However, this effect is not observed in the present device due to its large resistance and the considerable amount of heating generated by the current. In order to induce an observable shift in $H_{\rm res}$, according to Figure 4.6, a dc bias current of 1 mA is required to generate $\mathbf{h}_{\rm cit}^{\rm DC}$ on the order of 2 mT in a 500 nm-wide (Ga,Mn)As bar[1].

4.4 Conclusions

In this Chapter, the first experimental demonstration of an oscillating current-induced torque (CIT) in uniform ferromagnetic systems is reported. Ferromagnetic resonance has been created in microstructures patterned on diluted

[1]In a 4 μm-wide device, a dc bias current of 5 mA is required to generated $\mathbf{h}_{\rm cit}^{\rm DC} \approx 2$ mT.

magnetic semiconductors (Ga,Mn)As and (Ga,Mn)(As,P), using a microwave frequency CIT, and detected electrically via frequency mixing between the microwave current and the anisotropic magnetoresistance (AMR).

The magnitude and direction of the magnetic field leading to CIT have been measured. The results confirm that the current-induced field switches sign depending on the growth-strain of the wafer (compressive or tensile); furthermore, its magnitude can be controlled by lithography-induced strain-relaxation, or by varying the carrier densities. These observations suggest possible methods for customising the spin-orbit coupling in future spintronic devices.

Finally, the experiments described in this Chapter have established a new type of scalable, all-electrical FMR technique (CIT-FMR) which provides an unprecedented method to study the nature of CIT and to perform magnetic characterisation on ferromagnetic microstructures, which are not limited to magnetic semiconductors, but can also be ferromagnetic metal thin films.

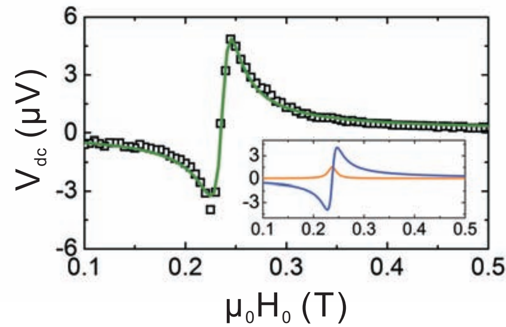

Figure 4.9: A photovoltage spectrum measured in CIT-FMR experiment showing the FMR peak (squares), together with its fitted results according to Equation 2.25 (green solid line). Inset: The symmetric (orange) and anti-symmetric (blue) Lorentzian components of the FMR peak, with amplitudes given as V_{sym} and V_{asy} respectively.

4.5 Appendices

4.5.1 Symmetric Lorentzian component V_{sym}

Figure 4.9 illustrates the two Lorentzian components (V_{sym} and V_{asy}) which make up a FMR signal detected in the photovoltage spectrum. For an in-plane driving field, it is expected that the FMR lineshape should be perfectly anti-symmetric and $V_{\mathrm{sym}} \to 0$, according to Equation 2.27. On the other hand, for a perpendicular-to-plane driving field as in the experiments described in Chapter 3, one expects the FMR peak to be perfectly symmetric and $V_{\mathrm{asy}} \to 0$.

However, in most real FMR experiments, the lineshape of the resonance signal is rarely perfect and usually contains a superposition of symmetric and anti-symmetric Lorentzians. Among the published literatures, several parallel explanations exist for the origin of this observed complex FMR lineshape:

- In device-scale FMR experiments on permalloy and iron samples, the

complex resonance peak is explained by the phase difference[1] (ψ) between the microwave current and the driving field [80, 81, 83], in which case the symmetric Lorentzian contains a $\sin\psi$ term whereas the anti-symmetric Lorentzian contains a $\cos\psi$ term.

- In conventional cavity-based FMR experiments, an anti-symmetric component in the energy absorption spectrum (which should in theory be perfectly symmetric) has been attributed to non-collinearity between $\mathbf{M}$ and $\mathbf{H}_0$ [78], caused by the large magnetocrystalline anisotropy in (Ga,Mn)As.

- In spin-transfer torque (STT) driven FMR experiments on magnetic tunnel junctions (MTJs), the appearance of a complex FMR lineshape is interpreted as arising from a strong perpendicular component of the driving torque (or "field-like" term as opposed to the STT term) [34]. However, later experiments on similar device structures attribute this complexity to a superposition of two normal modes from the different ferromagnetic layers of the MTJ [36, 63]. Moreover, in STT-FMR experiments on spin-valves, the asymmetric FMR lineshape caused by large microwave driving current is attributed to nonlinear oscillation effects [35].

- Besides the explanations mentioned above, inhomogeneity in the driving field and non-uniformity of the device would almost certainly play a role in creating the complex FMR signals.

Examining the various possible causes for the complex FMR lineshape shown in Figure 4.9, two explanations are most plausible: (i) The driving field has a component in the z-direction: $\mathbf{h}_{\text{cit}} = (h_x, h_y, h_z)e^{i\omega t}$, or (ii) There

[1]Some possible causes for the phase shift include: (i) The Eddy current inside the sample originates from both inductive and capacitive coupling, with a phase difference of $\pi/2$ between the two terms, and the total effective current can be understood as possessing a phase shift with respect to the varying resistance. (ii) The starting point of magnetisation precession, which occurs as the resonance condition is satisfied, and the starting point of the microwave current, which occurs as the microwave source is turned on, are not necessarily synchronised, giving rise to a phase difference.

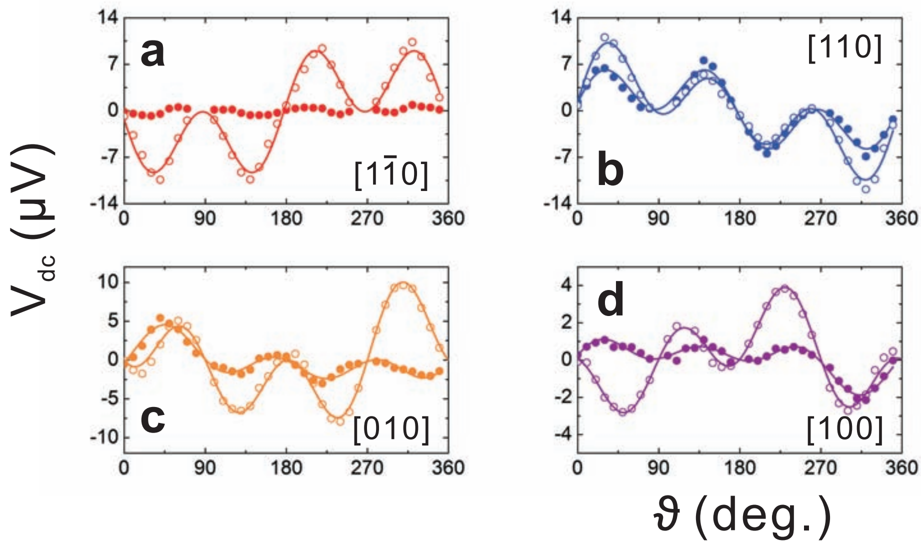

Figure 4.10: Amplitudes of the symmetric and anti-symmetric Lorentzian parts V_{sym} and V_{asy} measured on a group of 4 μm-wide (Ga,Mn)As bars (solid and hollow circles, respectively), patterned along different crystalline directions. The solid lines are fitted results to Equation 2.27.

exists a phase difference ψ between the microwave current $I\cos\omega t$ and the driving field $\mathbf{h}_{\text{cit}}$.

Figure 4.10 compares the amplitudes of the symmetric and anti-symmetric Lorentzians in a group of 4 μm-wide (Ga,Mn)As bars. No lineshape with $\sin 2\vartheta$ symmetry can be assigned to the $V_{\text{sym}}(\vartheta)$ function within experimental errors, hence an out-of-plane component of $\mathbf{h}_{\text{cit}}$ is ruled out as the cause of the symmetric Lorentzian in the measured FMR signals. Therefore it is concluded that the current-induced field $\mathbf{h}_{\text{cit}}$ is in-plane ($h_z = 0$), and the complex shape of the FMR signals is due to the phase difference ψ, which can be determined from the ratio between V_{sym} and V_{asy} according to Equation 3.1. For example, for the [100]-bar shown in Figure 4.10, it is estimated that the driving field leads the current by 12$^{\text{o}}$. Similar observations have also been made on the 500 nm-wide (Ga,Mn)As devices and on the (Ga,Mn)(As,P) micro-bars.

4.5.2 Calibrating the microwave current using Joule heating

The power of the microwave used in the CIT-FMR experiments is 20 dBm from the signal generator. This is reduced by many dB when it reaches the sample, due to frequency-dependent losses in the microwave circuit and strong reflection at the transmission line/device interface. However, in order to calculate the magnitude of the current-induced field $\mathbf{h}_{\mathrm{cit}}$, the strength of the microwave current inside the sample $I \cos \omega t$ needs to be accurately determined. This is achieved using the bolometric effect.

The resistance of the magnetic semiconductors (Ga,Mn)As and (Ga,Mn)(As,P) is strongly temperature-dependent (Figure 4.11a). Therefore by comparing the resistance change caused by Joule heating due to both a known direct current and the microwave, the level of the microwave current inside the sample can be determined (Figure 4.11b). Note that the direct current corresponds to the effective value of $I \cos \omega t$, i.e. its root-mean-square (rms) value.

The calibrated microwave current I_{mw} is plotted against the microwave voltage V_{mw} in Figure 4.11c, in which V_{mw} is the rms voltage output into the 50 Ω transmission line. The ohmic behaviour exhibited by the $I_{\mathrm{mw}} - V_{\mathrm{mw}}$ data confirms the validity of the calibration method.

4.5.3 Vector magnetometry on the (Ga,Mn)(As,P) devices

Photovoltage from in-plane scans Figure 4.12 shows the ϑ-dependence of the photovoltage amplitude V_{asy}, measured on the 4 μm-wide (Ga,Mn)(As,P) bars patterned along the [1$\bar{1}$0], [110], [010] and [100] crystalline directions. The $V_{\mathrm{asy}}(\vartheta)$ curves are reversed compared to those measured in the (Ga,Mn)As samples (Figure 4.5a and b), implying that the directions of $\mathbf{h}_{\mathrm{D}}$ and $\mathbf{h}_{\mathrm{R}}$ have changed signs due to the tensile-strained nature of the (Ga,Mn)(As,P) wafer.

It is noticed that in the [100] and [010] bars, the V_{asy} curve is shifted and $V_{\mathrm{asy}}(\vartheta = 0^{\mathrm{o}}) \neq 0$. This can be explained by a large uniaxial crystalline term C_U along [110] in the magnetoresistance of the (Ga,Mn)(As,P) devices

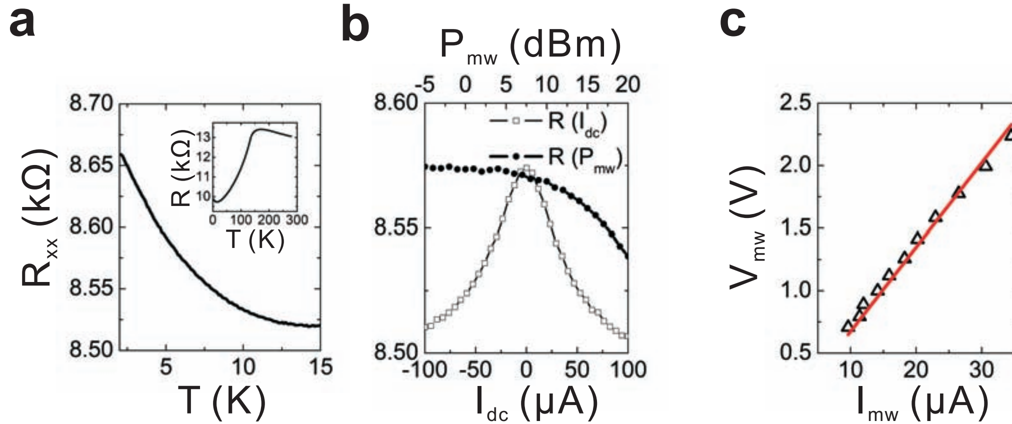

Figure 4.11: Deducing the microwave current using Joule heating. **a,** The temperature dependence of a device's longitudinal resistance $R_{xx}(T)$, in the temperature range where the measurements are carried out (6 K). Inset: The sample resistance measured over the entire temperature range 2.5 – 270 K. **b,** The change in sample resistance caused by Joule heating from both a known direct current $R(I_{\mathrm{dc}})$ and the microwave current, which is recognised only by the output power from the signal generator $R(P_{\mathrm{mw}})$. Typical loss on the microwave cabling is estimated to be $\sim$ 20 dB. **c,** The calibrated $I_{\mathrm{mw}} - V_{\mathrm{mw}}$ curve (triangles), where V_{mw} is the rms voltage output into the 50 Ω transmission line. The calibration errors are smaller than the size of the triangles in the graph ($\sim$ 0.3 μA), and are caused by uncertainties in finding the exact value of the direct current corresponding to each microwave power. The $I - V$ plots exhibits ohmic behaviour (The red solid line is a linear fit).

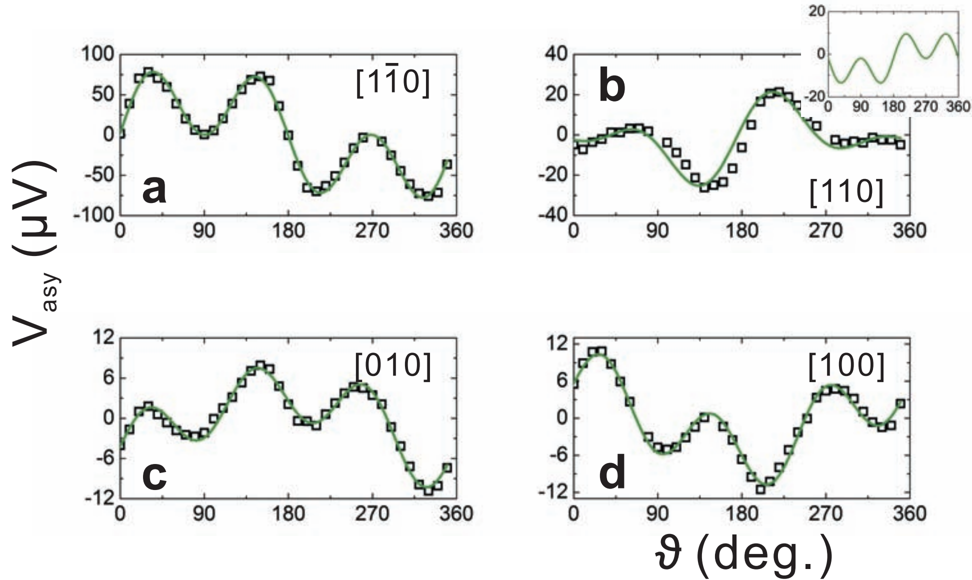

Figure 4.12: The photovoltage amplitude V_{asy} measured on 4 μm-wide (40 μm-long) (Ga,Mn)(As,P) bars, patterned along the [1$\bar{1}$0], [110], [010] and [100] crystalline directions, respectively (black squares). The green solid lines are the fitted results to either a $\sin(2\vartheta)\cos(\vartheta)$ function (**a** and **b**), or a superposition of $\sin(2\vartheta)\cos(\vartheta)$ and $\sin(2\vartheta)\sin(\vartheta)$ functions (**c** and **d**). Note that there exists a relatively large $\sin(2\vartheta)$ contribution to the $V_{\text{asy}}(\vartheta)$ measured on the [110] bar (**b**), possibly caused by an out-of-plane Oersted field. After removing this contribution, the remaining data exhibits a clear $\sin(2\theta)\cos(\theta)$ curve (inset to **b**).

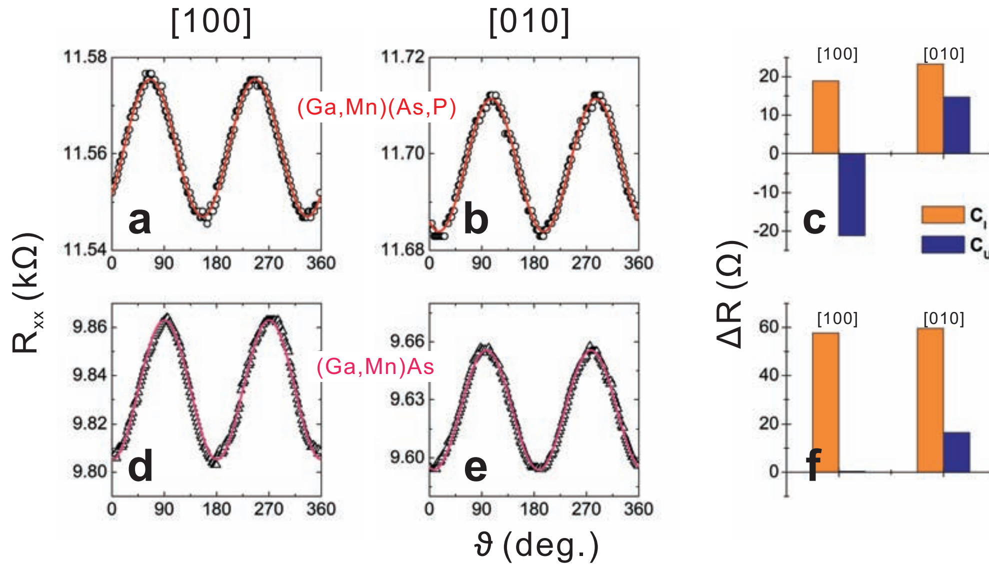

Figure 4.13: The longitudinal resistance measured on 4 μm-wide (Ga,Mn)(As,P) and (Ga,Mn)As bars. **a,** $R_{xx}(\vartheta)$ measured on the [100] bar (black circles). The red line is the fitted results according to Equation 2.8, taking into account of both non-crystalline (C_I) and uniaxial crystalline (C_U) AMR components. The measurement is performed by rotating a saturation field of 0.8 T and measuring with a probing voltage of 10 mV. **b,** $R_{xx}(\vartheta)$ measured on the [010] bar. **c,** The AMR coefficients C_I and C_U in the [100] and [010] micro-bars determined from fittings. **d − f,** The longitudinal resistance measured in similar 4 μm-wide (Ga,Mn)As devices, with the fitted C_I and C_U terms.

(cf. Equation 2.8). Figure 4.13 compares the longitudinal resistance R_{xx} measured on (Ga,Mn)(As,P) and (Ga,Mn)As micro-bars in rotating field experiments. The large C_U term in (Ga,Mn)(As,P) devices can be clearly recognised, which is caused by the tensile-strain in the wafers.

Photovoltage from out-of-plane scans Besides in-plane rotational scans of $\mathbf{H}_0$, out-of-plane field sweep measurements are also carried out on the

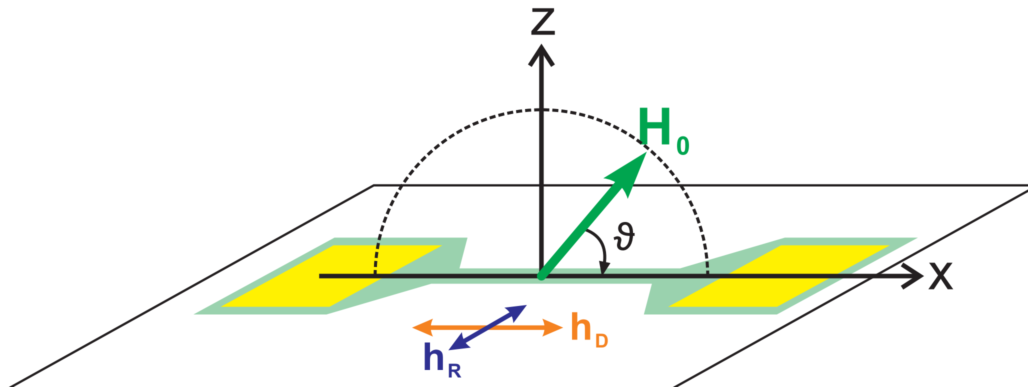

Figure 4.14: Principle of an out-of-plane rotational scan experiment. For a micro-bar patterned along the [100]/[010] direction, the component of the current-induced field $\mathbf{h}_{\mathrm{cit}}$ due to the Rashba spin-orbit interaction $\mathbf{h}_{\mathrm{R}}$ (blue arrow) now becomes perpendicular to the plane of rotation, whereas the one due to the Dresselhaus interaction $\mathbf{h}_{\mathrm{D}}$ (orange arrow) remains in-plane.

(Ga,Mn)(As,P) devices[1]. Figure 4.14 illustrates the experimental concept of an out-of-plane rotational scan. For a micro-bar patterned along the [100] or [010] direction, the component of the current-induced field due to the Rashba spin-orbit coupling $\mathbf{h}_{\mathrm{R}}$ becomes perpendicular to the plane of field rotation, whereas the one due to the Dresselhaus interaction $\mathbf{h}_{\mathrm{D}}$ remains in-plane.

The photovoltage amplitudes from the out-of-plane rotational scan on a [100]-bar are plotted in Figure 4.15a–b. The graphs clearly show that the two components of the driving field, $\mathbf{h}_{\mathrm{R}}$ and $\mathbf{h}_{\mathrm{D}}$, are now decomposed and mapped separately into the symmetric and anti-symmetric Lorentzian parts of the FMR signals, respectively. The amplitude of the symmetric Lorentzian $V_{\mathrm{sym}}(\vartheta)$ clearly shows a $\sin(2\vartheta)$ lineshape, which confirms the existence of an perpendicular-to-plane driving field ($\mathbf{h}_{\mathrm{R}}$); whereas the anti-symmetric Lorentzian part is caused by an in-plane driving field ($\mathbf{h}_{\mathrm{D}}$), exhibiting $\sin(2\vartheta)\sin(\vartheta)$ dependence (in-plane and along the direction of the

[1]The out-of-plane rotational scans are only possible on (Ga,Mn)(As,P) devices using the current apparatus. For compressively-strained (Ga,Mn)As devices, the resonance field H_{res} can be greater than 1 T in out-of-plane directions, as shown in Ref [74], hence is too large for the superconducting magnets on this cryostat to generate.

bar).

In comparison, for an out-of-plane rotational scan on a $[1\bar{1}0]$ bar, only a perpendicular-to-plane driving field is present since $\mathbf{h}_{\mathrm{R}}$ and $\mathbf{h}_{\mathrm{D}}$ are collinear along this direction. Figure 4.15c shows that $\mathbf{h}_{\mathrm{cit}}$ leads to predominantly symmetric FMR peaks with $V_{\mathrm{sym}}(\vartheta) \propto \sin 2\vartheta$. The anti-symmetric part of the FMR peaks (Figure 4.15d) in this device is much smaller, and is due to the phase difference ψ between the current and the driving field. These observations are consistent with the derivations given in Section 2.4.3 and Appendix A.

By comparing the amplitude of V_{asy} shown in Figure 4.12d and Figure 4.15a–b, it is clear that both in-plane and out-of-plane measurements can be used for deducing the current-induced fields $\mathbf{h}_{\mathrm{R}}$ and $\mathbf{h}_{\mathrm{D}}$. Note that V_{asy} appears to be smaller in the out-of-plane scans (Figure 4.12d), since a 17 GHz microwave current is used in these experiments, which suffers higher loss in the coaxial cable than the 10 GHz current used on the in-plane rotational scans. Similar observations can also be made by comparing the in-plane and out-of-plane scan data on the $[1\bar{1}0]$ micro-bar (Figure 4.12a and Figure 4.15c).

4.5.4 Magnetic properties of the (Ga,Mn)As microdevices

Magneto-transport measurements Figure 4.16 shows the results from transport measurements on 4 μm-wide (Ga,Mn)As micro-bars with 3%, 6% and 12% Mn. Using the temperature-derivative of the longitudinal resistance R_{xx} [102], the Curie temperatures in the three materials are found to be 73, 132 and 169 K respectively. The results from the AMR measurements[1] (Figure 4.16b) are used to determine ΔR required for calculating the current-induced field $\mathbf{h}_{\mathrm{cit}}$ (as shown in Figure 4.7). The non-crystalline AMR term is observed to be dominant in all three devices.

[1] Note that AMR is defined as $(R_{xx}-R_{\mathrm{ave}})/R_{\mathrm{ave}}$, where R_{ave} is the average longitudinal resistance in the rotational measurement.

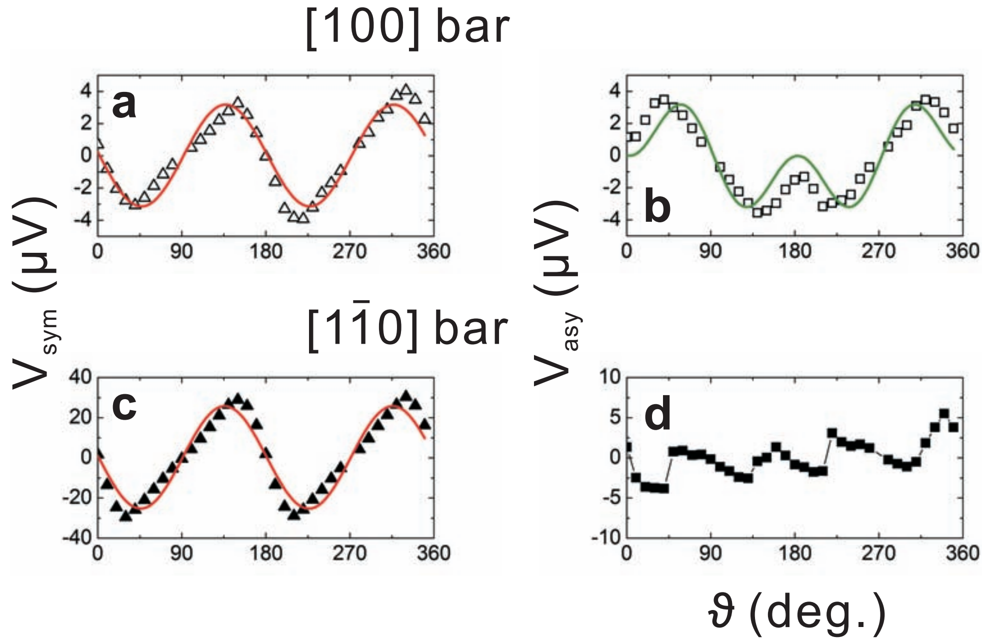

Figure 4.15: **a,** The photovoltage amplitude V_{sym} from an out-of-plane rotational scan experiment on a 4 μm-wide (Ga,Mn)(As,P) bar, patterned along the [100] direction (hollow triangles). The red solid line is the fitted result to a $\sin(2\vartheta)$ function. **b,** The amplitude of the anti-symmetric Lorentzian V_{asy} measured on the same device (hollow squares). The red solid line is the fitted results to a $\sin(2\vartheta)\sin(\vartheta)$ function. **c – d,** $V_{\text{sym}}(\vartheta)$ and $V_{\text{asy}}(\vartheta)$ curves from an out-of-plane scan on a [1$\bar{1}$0] bar (solid triangles and squares respectively), together with fittings to a $\sin(2\vartheta)$ function (red solid line).

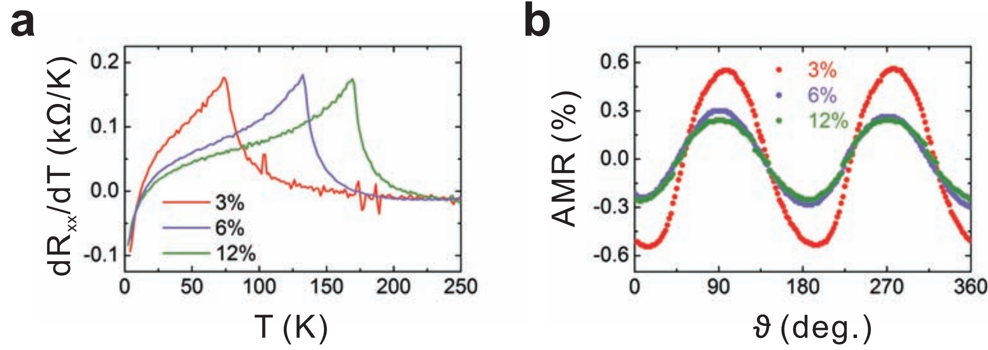

Figure 4.16: Transport measurements on (Ga,Mn)As micro-bars with different Mn concentrations (3%, 6% and 12%). **a,** The temperature derivative dR_{xx}/dT in the three devices, giving $T_C = 73$, 132 and 169 K respectively. **b,** Longitudinal AMR measured in the three devices. All samples are 4 μm-wide and are fabricated on annealed wafers (190°C in air for 20 h).

Effect of growth-strain on the magnetic anisotropy The magnetic anisotropy in the (Ga,Mn)As and (Ga,Mn)(As,P) microstructures are also investigated using CIT-FMR. The anisotropy in tensile-strained (Ga,Mn)(As,P) devices is found to be significantly different from that in the compressively-strained (Ga,Mn)As samples, and is investigated in details in Chapter 5.

Figure 4.17 plots the photovoltage spectra from in-plane rotational scans of $\mathbf{H}_0$, as well as the fitted resonance peak positions H_{res}, measured on a group of 4 μm-wide (Ga,Mn)As samples with different Mn doping. The large device size ensures that strain-relaxation plays an insignificant role in defining the magnetic anisotropy. The data demonstrates that as the level of Mn doping increases, the magnetic anisotropy changes from predominantly biaxial along [100]/[010] (fourfold symmetry due to the zinc-blende crystal structure) to uniaxial along [$1\bar{1}0$] (twofold symmetry due to strain).

The in-plane anisotropy constants H_i and the effective magnetisation M_{eff} are deduced by fitting $H_{\text{res}}(\varphi)$ to Equation 3.2 and are listed in Table 4.1. (Ga,Mn)As wafers with higher Mn dopings are under more compressive-strain, due to the larger lattice mismatch with the GaAs substrates. This in turn leads to larger $H_{2\perp}$ field, which is reflected by the increase of M_{eff} with

	$\mu_0 M_{\text{eff}}$ (mT)	$\mu_0 H_{4\parallel}$ (mT)	$\mu_0 H_{2\parallel}$ (mT)
3%	373	150.7	6.6
6%	478	21.7	27.2
12%	517	5.2	61.2

Table 4.1: The in-plane anisotropy fields H_i and the effective magnetisation M_{eff}, determined using the CIT-FMR technique, in (Ga,Mn)As microdevices with different Mn levels. All three devices are 4 μm$\times$40 μm and are patterned along the [010] crystalline direction.

Mn levels ($M_{\text{eff}} = M_s - H_{2\perp}$).

Observation of patterning-induced strain-relaxation in narrow structures Numerical calculations have shown that strain-relaxation is spatially nonuniform and usually takes place on a length scale of several hundred nanometres [26, 115]. This effect has been observed to play an important role in defining the magnetic anisotropy in submicron (Ga,Mn)As devices [65–67]. The magnetic anisotropy profiles on the 500 nm-wide bars, mapped with the CIT-FMR technique, corroborate the findings from earlier studies.

Figure 4.18a–d plot the resonance field H_{res} detected on a group of 500 nm-wide (Ga,Mn)As bars (6% Mn). In the [100] and [010] bars (Figure 4.18a and 4.18b), the existence of the strain-relaxation-induced term H_U strongly distorts the magnetic anisotropy profile of bulk wafers (as in Figure 4.17d), and causes asymmetry in H_{res} between the [100] and [010] directions. In the [110] and [1$\bar{1}$0] bars (Figure 4.18c and 4.18d), H_U is collinear with the intrinsic uniaxial anisotropy $H_{2\parallel}$, and acts to either enhance or reduce the magnetic energy in the [110]/[1$\bar{1}$0] directions.

From the figures, it is also concluded that H_U has its easy axis along the direction of the bar, i.e. perpendicular to the direction of lattice relaxation. This is consistent with earlier studies using SQUID, magnetotransport and FMR measurements [26, 65–67]. Table 4.2 lists the anisotropy constants H_i in these devices deduced from fittings.

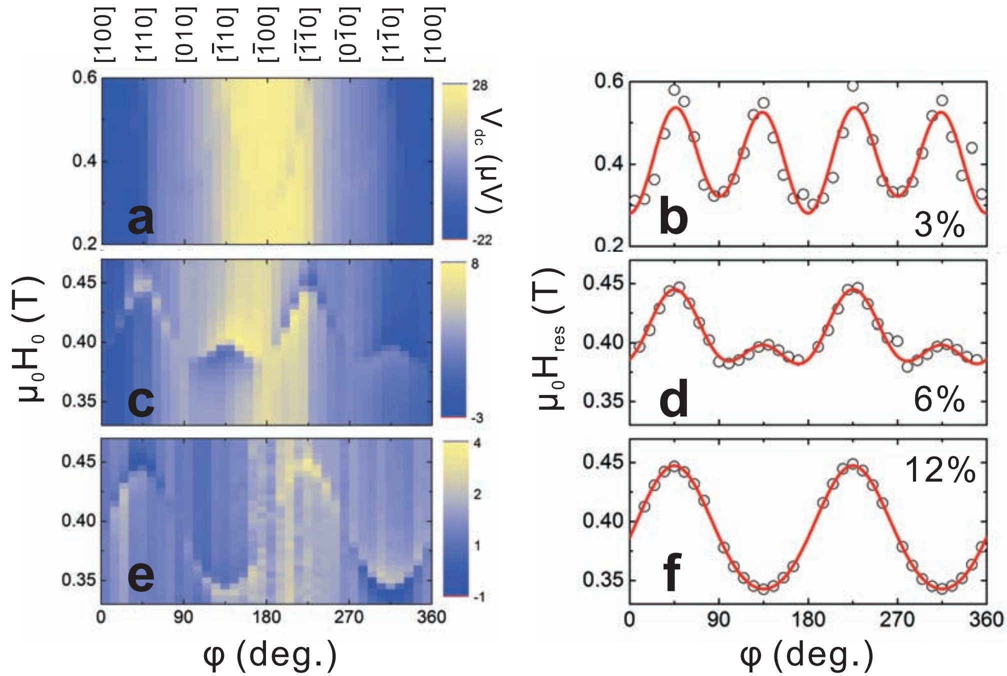

Figure 4.17: Magnetic anisotropy profiles in (Ga,Mn)As microstructures with different Mn concentrations. **a − b,** The photovoltage spectra from in-plane rotational scans on a 4 μm-wide device with 3% Mn, together with the φ-dependence of the resonance field $H_{\rm res}$ (black circles). The red solid line is the fitted results according to Equation 3.2. **c − d,** Similar measurements on a micro-bar with 6% Mn. **e − f,** Measurements on a micro-bar with 12% Mn. All three devices are 4 μm × 40 μm and are patterned along the [010] crystalline direction.

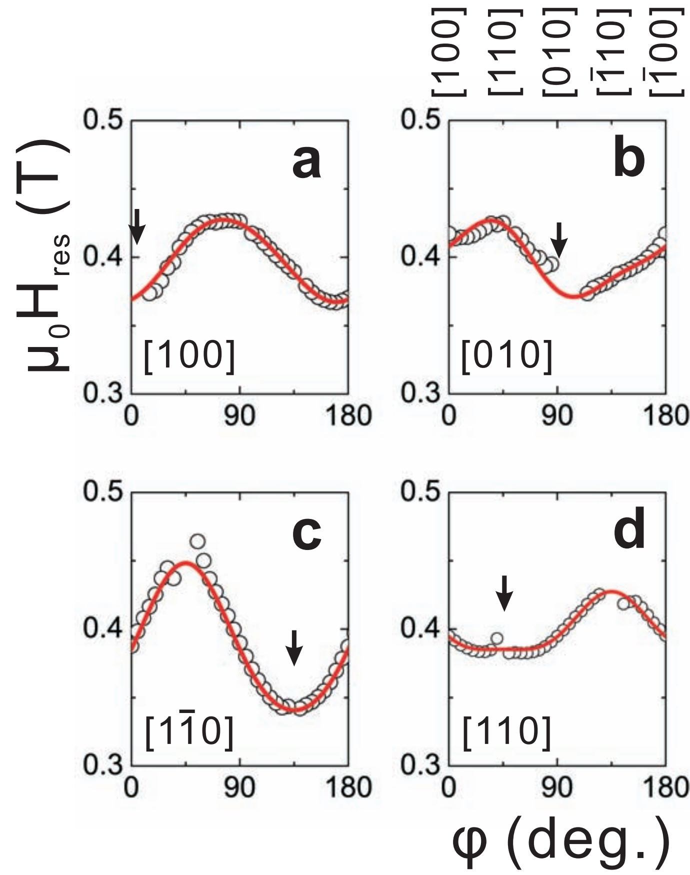

Figure 4.18: Magnetic anisotropy profiles on a group of 500 nm-wide ($Ga_{0.94}$,$Mn_{0.06}$)As bars, patterned along [100], [010], [1$\bar{1}$0] and [110] crystalline directions. The black circles are experimental data, and the red solid lines are fitted results according to Equation 3.2. The black arrows mark the directions of the nano-bars.

	$\mu_0 H_{4\parallel}$ (mT)	$\mu_0 H_{2\parallel}$ (mT)	$\mu_0 H_U$ (mT)
[100]	1.9	13.8	-32.6
[010]	8.0	23.3	18.9
$[1\bar{1}0]$	5.7	62.8	‡
[110]	7.7	-24.8	‡

Table 4.2: In-plane magnetic anisotropy constants in a group of 500 nm-wide (Ga,Mn)As bars (6% Mn), patterned along different crystalline directions. The strain-relaxation-induced anisotropy $H_U > 0$ when its easy axis is along the [010] direction; and it is not separately deduced in the $[1\bar{1}0]$ and [110] bars since it is collinear with $H_{2\parallel}$.

4.5.5 Effects of annealing

Magnetic anisotropy Finally, the effects of annealing on the magnetic anisotropy and $\mathbf{h}_{\mathrm{cit}}$ are investigated. Figure 4.19 compares the magnetic anisotropy profiles of a 500 nm-wide ($Ga_{0.94}$,$Mn_{0.06}$)As bar before and after it has been annealed. The anisotropy changes from a superposition of twofold and fourfold symmetry in the as-grown sample (due to H_U and $H_{4\parallel}$ respectively), to a pronounced twofold symmetry (due to H_U) after annealing (160°C in air for 10 h). Similar measurements are also performed on the other micro-bar from the same sample chip, and the effective magnetisation M_{eff} and anisotropy fields H_i are compared in Table 4.3. The changes in magnetic anisotropy upon annealing are summarised as follows:

- The effective magnetisation M_{eff} increases after annealing. This agrees with observations from early FMR experiments on (Ga,Mn)As bulk wafers (8% Mn) [73, 74]. It is due to an increase in the perpendicular uniaxial anisotropy $H_{2\perp}$, which can be attributed either to the improvement of the sample homogeneity or (more likely) to an increase of the hole concentration after the removal of interstitial Mn_I ions by the annealing process [74].
- The in-plane biaxial anisotropy $H_{4\parallel}$ is dramatically reduced by annealing. This is due to decrease in lattice mismatch in the annealed

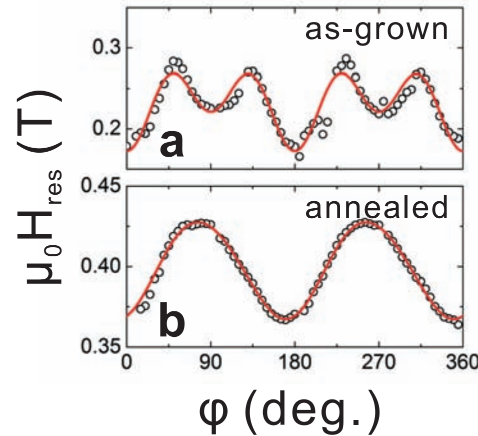

Figure 4.19: Magnetic anisotropy profiles of a 500 nm-wide (Ga,Mn)As bar (6% Mn), before (**a**) and after (**b**) it has been annealed at 160ºC in air for 10 h. The device is patterned along the [100] axis. In the figures, the black circles are the experimental data, and the red solid lines are fitted results using Equation 3.2.

(Ga,Mn)As epilayer, as revealed by XRD studies [138], and hence reduction in the compressive-strain.

- The weak intrinsic in-plane uniaxial anisotropy $H_{2\|}$ grows after annealing. This observation is related to a type of spin reorientation transitions, in which $H_{2\|}$ rotates its easy axis from $[1\bar{1}0]$ direction to [110] direction upon annealing. This effect is first noticed in SQUID measurements [110] and later corroborated by FMR experiments [74].

- Annealing also influences the strain-relaxation-induced anisotropy H_U. This is understandable as both the strain and hole concentration are changed upon annealing. However, the two nano-bars exhibit opposite response to the annealing process, and further investigations are therefore required.

Angle dependence of the FMR lineshape Even more intriguing is the impact of annealing on the FMR lineshape. In Figure 4.20, ϑ-dependence of

		$\mu_0 M_{\text{eff}}$ (mT)	$\mu_0 H_{4\parallel}$ (mT)	$\mu_0 H_{2\parallel}$ (mT)	$\mu_0 H_U$ (mT)
[100] bar	as-grown	416.9	43	0.4	-28.2
	annealed	534.2	1.9	13.8	-32.6
[010] bar	as-grown	397.7	44.2	7.9	30
	annealed	500.6	8	23.3	18.9

Table 4.3: The effective magnetisation M_{eff} and in-plane anisotropy fields H_i in two (Ga,Mn)As bars (500 nm-wide) before and after annealing (160°C in air for 10 h). $H_U > 0$ indicates that its easy axis is along the [010] direction.

the anti-symmetric component V_{asy} before and after annealing are compared. The same 500 nm-wide ($Ga_{0.94}$,$Mn_{0.06}$)As bars are used.

In the as-grown sample, the $V_{\text{asy}}(\vartheta)$ function contains a complex lineshape which cannot be simply explained using the equations derived in Section 2.4.3. Furthermore, $V_{\text{asy}}(\vartheta)$ in both [010] and [100] bars (Figure 4.20a and 4.20c) displays similar lineshape. Figure 4.21 investigates the contribution from the crystalline AMR coefficients to the $V_{\text{asy}}(\vartheta)$ lineshape. It is found that a large cubic crystalline term is required in order to properly fit to the experimental data, with $C_C \geq C_I$ (see Figure 4.21b inset), which is not present in the longitudinal resistance R_{xx} measured on this device (Figure 4.21a inset). This confirms that AMR is not the cause of the observed $V_{\text{asy}}(\vartheta)$ curve. Consistent observations have been made among several as-grown devices along the [100]/[010] directions, and this has become a great mystery in the early stages of the CIT-FMR project.

Upon annealing, the lineshape of the $V_{\text{asy}}(\vartheta)$ function changes significantly, and can now be well-described by an in-plane driving field $\mathbf{h}_{\text{cit}} = (h_x, h_y, 0)e^{i\omega t}$, with h_x switching sign between the [010] and [100] bars. The AMR coefficients are largely reduced upon annealing, with C_I: 3.2% $\rightarrow$ 0.57%, C_U: 0.6% $\rightarrow$ 0.1% and C_C: 0.36% $\rightarrow$ 0.023%. However, this cannot account for the drastic change in the shape of the $V_{\text{asy}}(\vartheta)$ function. Instead, it is attributed to the improvement in sample homogeneity by the removal of Mn_I defects. This demonstrates the complexity of the current-induced torque in as-grown, inhomogeneous ferromagnets.

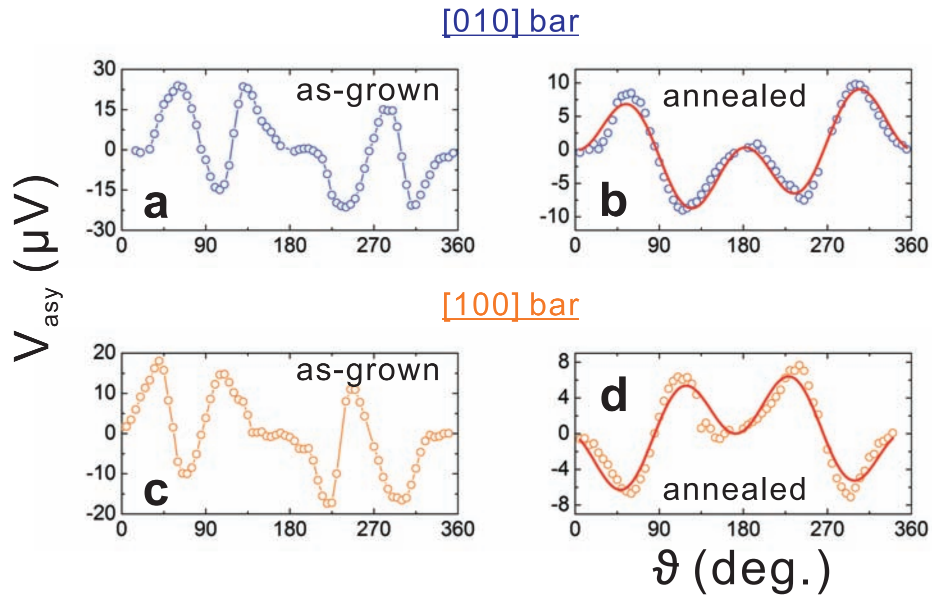

Figure 4.20: The amplitudes of the anti-symmetric Lorentzian $V_{\mathrm{asy}}(\vartheta)$ measured before and after annealing, on the [010] bar (**a** and **b**, blue circles) and the [100] bar (**c** and **d**, orange circles). The red solid lines are fitted results to a $A_1 \sin(2\vartheta)\cos(\vartheta) + A_2 \sin(2\vartheta)\sin(\vartheta)$ function with variables A_1 and A_2.

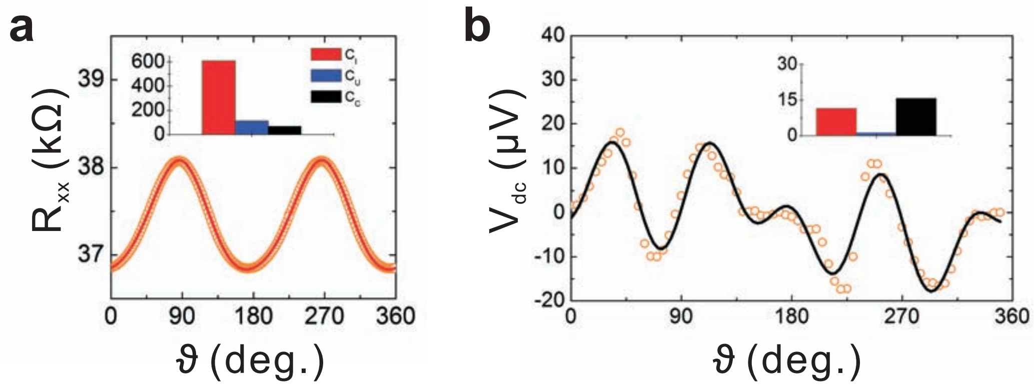

Figure 4.21: The AMR components and their contributions to the longitudinal resistance and the FMR lineshape, measured on the as-grown [100] bar (500 nm-wide). **a,** The longitudinal resistance R_{xx} measured in a field rotation experiment with $\mu_0 H_0 = 0.8$ T (circles: experimental data, red line: fittings using Equation 2.8). Inset: Values (in Ω) of the non-crystalline and first order crystalline (uniaxial and cubic) AMR coefficients C_I, C_U and C_C. C_I is found to be the dominant contribution to the $R_{xx}(\vartheta)$ function. **b,** ϑ-dependence of V_{asy} (orange circles), and the black solid line is the fitted results taking into account of both the non-crystalline and crystalline terms in the R_{xx} expression. Inset: Contributions (in μV) from the non-crystalline, uniaxial and cubic crystalline terms to $V_{\text{asy}}(\vartheta)$. Contrary to the values found from **a**, a large cubic crystalline term is required to describe the lineshape of $V_{\text{asy}}(\vartheta)$, which does not exist in the measured $R_{xx}(\vartheta)$ data.

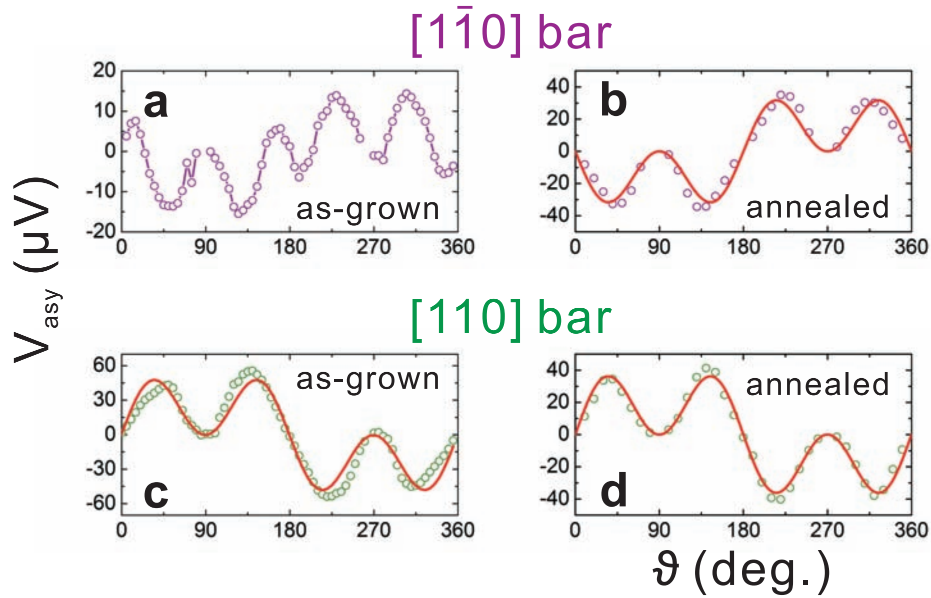

Figure 4.22: $V_{\text{asy}}(\vartheta)$ measured before and after annealing, on a 500 nm-wide [1$\bar{1}$0] bar (**a** and **b**, purple circles) and a [110] bar (**c** and **d**, green circles). The red solid lines are fitted results to $\sin(2\vartheta)\cos(\vartheta)$ functions.

The effects of annealing on [110] and [1$\bar{1}$0] nano-bars are also studied and compared in Figure 4.22. It is recognised that $\mathbf{h}_{\text{cit}}$ also possesses complexity in the as-grown [1$\bar{1}$0] bar, and the measured $V_{\text{asy}}(\vartheta)$ curve cannot be described by a simple $\sin(2\vartheta)\cos(\vartheta)$ function (Figure 4.22a). In the [110] device, on the other hand, the V_{asy} curve is already well-defined in the as-grown sample, implying an excitation field $\mathbf{h}_{\text{cit}} = (0, h_y, 0)e^{i\omega t}$ (Figure 4.22c). Nevertheless, the removal of defects with low temperature annealing is also observed to improve the behaviour of $\mathbf{h}_{\text{cit}}$ in both devices (Figure 4.22b and 4.22d).

4.5.6 Gating experiments on ultrathin (Ga,Mn)As films

Besides the main experiments described in this Chapter, attempts have also been made on studying both $\mathbf{h}_{\text{cit}}$ and magnetic anisotropy in gated (Ga,Mn)As devices, with Au/dielectric/(Ga,Mn)As structures. These experiments are still on-going, and limited results have been obtained so far.

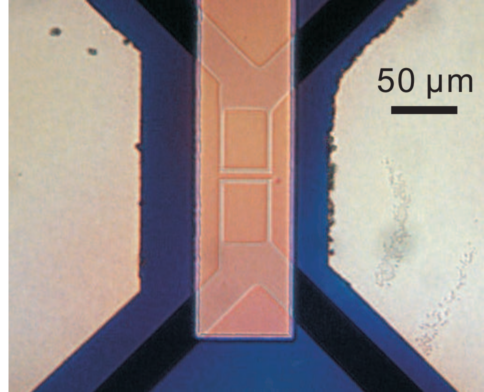

Figure 4.23: Micrograph of the gated (Ga,Mn)As device. The rectangular channel in the centre of the graph is the 40 μm $\times$ 4 μm device, with metal contacts on each end (Cr/Au, light yellow colour). The AlO_x dielectric has a distinct blue colour. The brown-coloured rectangular stripe covering the device channel is the gate electrode (Cr/Au).

The ($Ga_{0.94}$,$Mn_{0.06}$)As films used in this study are either 5 nm- or 7 nm-thick. These wafers have very low carrier concentration while still exhibit ferromagnetism, making them ideal for electrical gating experiments [10, 12, 139].

Two types of dielectric have been used. The first is a ferroelectric material, copolymer polyvinylidene fluoride with trifluoroethylene P(VDF-TrFE). It is recently employed in a (Ga,Mn)As–FET structure and has been demonstrated to change the Curie temperature and magneto-transport properties of (Ga,Mn)As upon charging [139]. However, when applying CIT-FMR on (Ga,Mn)As devices coated with ferroelectric P(VDF-TrFE), no resonance signals can be detected. This is possibly due to P(VDF-TrFE) having a small dielectric constant, hence causing the microwave current to leak into the gate electrode instead of flowing into the sample.

The second type of dielectric is aluminium oxide AlO_x, which is deposited onto the (Ga,Mn)As wafer using atomic layer deposition (ALD) with a nominal thickness of 40 nm (Figure 4.23). Measured at 46 K, charging the gate electrode to $V_g = \pm 20$ V leads to change in the sample resistance by 10%,

from 110 kΩ at +20 V to 91 kΩ at −20 V (data measured by Hidekazu Kurebayashi and Philip Chow [140]). This small change in resistance suggests that the gate voltage is unable to significantly accumulate/deplete the charge carriers. As a result, no change in the magnetic anisotropy has been measured between $V_g = \pm 20$ V within the experimental error. In the contrary, a recent study by Chiba *et al.* [10] has revealed resistance change of more than one order of magnitude using a gate electric field of ±12 V at $T = 2$ K, in a 4 nm-thick $(Ga_{0.9},Mn_{0.1})As$ device with 31 nm ZrO_2 dielectric.

Future CIT-FMR experiments using AlO_x dielectric will therefore focus on thinner devices, in which significant resistance change can be induced by electrical gating.

Chapter 5

Mapping the magnetic anisotropy in (Ga,Mn)(As,P) nanostructures

5.1 Introduction

(Ga,Mn)(As,P) is a new member of the (III,Mn)V diluted magnetic semiconductor family, first synthesised in 2007 [90]. Since the phosphorus atoms are smaller than the arsenic atoms, the (Ga,Mn)(As,P) wafers become tensile-strained for P concentrations higher than $\sim 6\%$, leading to out-of-plane magnetic anisotropy[1] [77]. The corresponding perpendicular-to-plane easy axis is beneficial for studies such as current-induced domain wall motion [24] and gating-controlled ferromagnetism [9, 10, 12], in which case the magnetisation switching and domain wall movement can be directly detected using Kerr microscopy [142, 143] and the anomalous Hall effect [9, 142]. However, the more conventional (Ga,Mn)As can only become tensile-strained if it is grown on a relaxed InGaAs buffer [95], and this could result in high density of line defects, causing incoherent magnetisation switching due to multiple

[1] (Ga,Mn)As layers grown directly on GaAs substrates are compressively-strained due to lattice mismatch, and this leads to in-plane magnetic easy axes for Mn concentrations $> 2\%$, unless the carrier density is very low [141].

nucleation and domain wall pinning sites [144, 145]. Therefore the tensile-strained (Ga,Mn)(As,P) provides a good test-bench to study magnetisation reversal processes.

Properties of (Ga,Mn)(As,P) bulk wafers have so far been studied, and change in magnetic anisotropy by varying the phosphorus doping concentration at the crystal growth stage has been especially investigated [77, 92–94]. In the case of (Ga,Mn)As, various methods for manipulating the magnetic anisotropy have been established, such as carrier depletion/accumulation via electrostatic gating [9–12], applying mechanical stress [5–8], or inducing strain-relaxation by lithographic patterning [26, 65–67]. It is an aim to investigate these effects also in the novel (Ga,Mn)(As,P) system.

In this Chapter, CIT-FMR has been applied to (Ga,Mn)(As,P) nanostructures as small as $80 \times 1000 \times 25$ nm^3, and the first systematic study of the effect of strain-relaxation on the magnetic anisotropy in these samples is reported. The strong spin-orbit and exchange interactions in (Ga,Mn)(As,P) provide the prerequisites for CIT-FMR, and the following insights have been achieved:

- The tensile-strain-relaxation in patterned (Ga,Mn)(As,P) bars generates an additional in-plane uniaxial anisotropy perpendicular to the bar direction, which becomes the dominant term in very narrow bars (80 nm-wide). This effect is found to be larger than previously reported in strain-relaxed (Ga,Mn)As patterned devices [65–67].

- The strain-relaxation-induced anisotropy in bars patterned from compressively-strained material (in this case, (Ga,Mn)As wafers with the same nominal Mn concentration as the (Ga,Mn)(As,P) epilayers) has the opposite sign.

- The patterning process can also affect the magnetic easy axis of the epilayers, tilting it from the out-of-plane position to partially in-plane.

5.2 Devices and experimental methods

25 nm-thick ($Ga_{0.94}$,$Mn_{0.06}$)As and ($Ga_{0.94}$,$Mn_{0.06}$)($As_{0.9}$,$P_{0.1}$) wafers have been used in this experiment. They are prepared using LT-MBE by Richard Campion, Arianna Casiraghi and coworkers at the University of Nottingham.

Figure 5.1a shows a SEM image of a 80 nm-wide, 1 μm-long bar device. It is fabricated by patterning isolation trenches on the (Ga,Mn)(As,P) epilayers. The microwave frequency current-induced torque is used to drive magnetisation precession in these devices, and signal detection is achieved using the frequency mixing effect (Section 3.2.3). The lock-in technique is employed to increase the measurement sensitivity, using a modulation frequency[1] of 23.7 Hz. A schematic of the experimental setup is shown in Figure 5.1b.

5.3 Data and analysis

A total number of 26 (Ga,Mn)(As,P) nanodevices with various sizes and along different crystalline directions have been measured using CIT-FMR. Consistent results have been attained and are summarised in this Section. Note that all devices have been annealed at 180°C in air for 48 h. This is because the as-grown (Ga,Mn)(As,P) wafers (10% P) are electrically insulating at low-temperatures [92].

5.3.1 Realisation of FMR in 80 nm-wide devices

Figure 5.2a shows the photovoltage spectra measured on a 80 nm-wide device (patterned along $[1\bar{1}0]$), for field sweeps along different crystalline directions (green circles), using a microwave frequency of 10 GHz. In each case, the FMR peak is clearly recognisable on the photovoltage spectrum, and can be fitted using the solution of the LLG equation (Equation 2.25). The positions of the resonance H_{res} vary due to the magnetic anisotropy.

[1]When performing lock-in measurements, only the signal in-phase with the reference frequency, i.e. the X-channel on the lock-in amplifier, is recorded. It is therefore necessary for the modulated photovoltage to be mostly in-phase with the reference frequency. For the (Ga,Mn)(As,P) devices, a modulation frequency of 23.7 Hz meets this requirement.

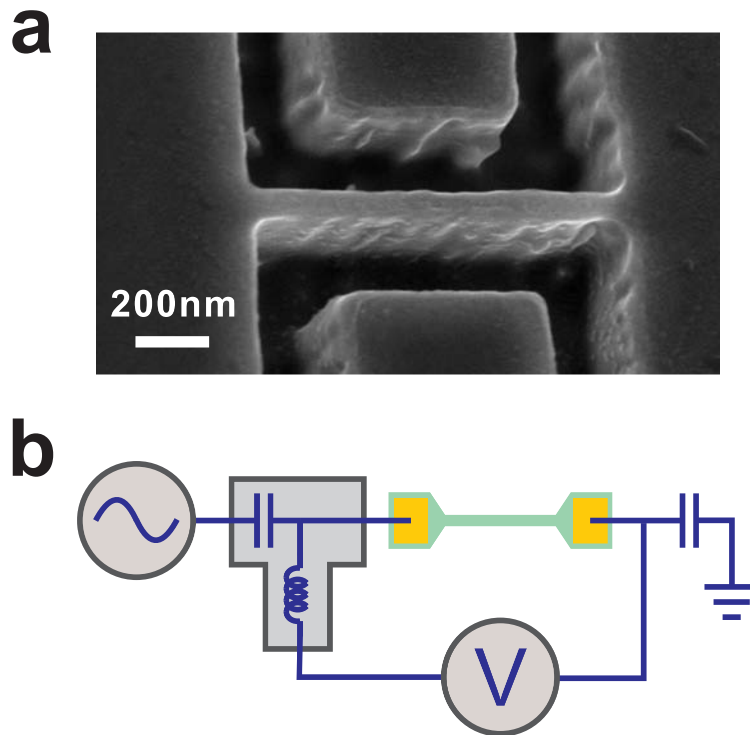

Figure 5.1: **a,** A SEM image of a 80 nm-wide (Ga,Mn)(As,P) bar. **b,** Schematic of the CIT-FMR setup (not-to-scale).

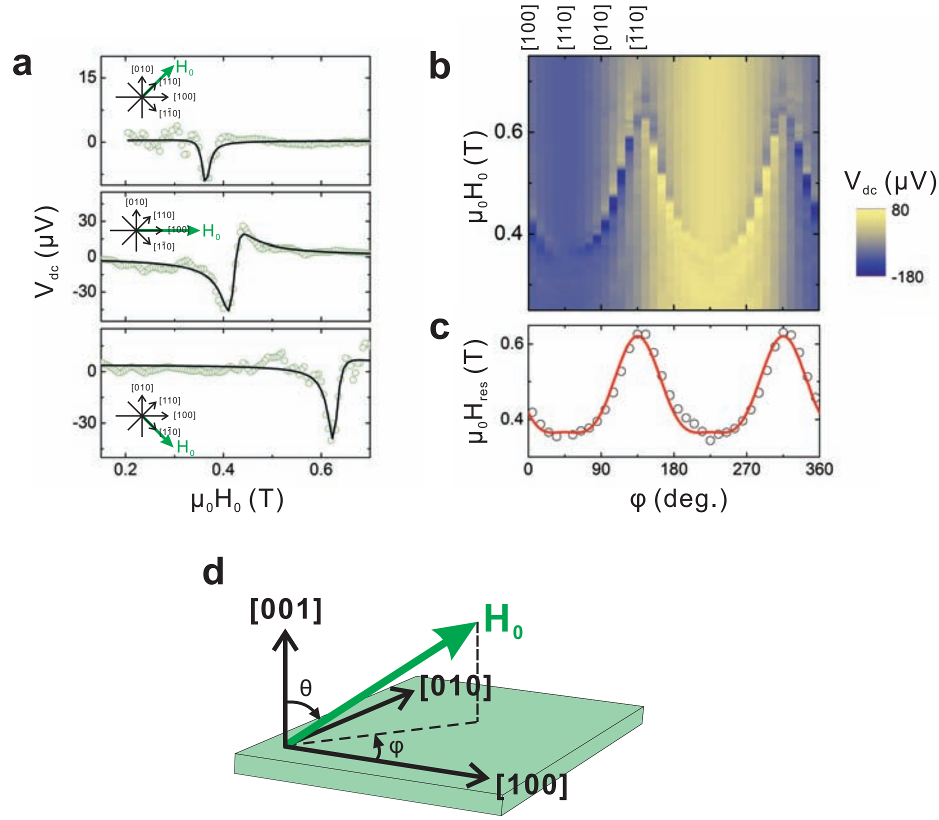

Figure 5.2: Photovoltage spectra measured on a 80 nm-wide sample (patterned along the [1$\bar{1}$0] axis). **a,** V_{dc} measured for $\mathbf{H}_0$ swept along different crystalline directions ([110], [100] and [1$\bar{1}$0] respectively, as indicated by the inset of each graph), using a 10 GHz current. The green circles are the measurement data, and the black solid lines are fitted results to Equation 2.25. **b,** Full photovoltage spectra for an in-plane rotational scan. The colour scale represents the magnitude of V_{dc} (in μV). **c,** The φ-dependence of the resonance field H_{res} (black circles). The red solid line is the fitted results to Equation 2.20. **d,** The geometry used in the experiment.

Figure 5.2b presents the full photovoltage spectra for an in-plane rotational scan of $\mathbf{H}_0$ ($\theta = 90^{\circ}$ as in Figure 5.2d). The FMR peak is clearly observed on top of a non-resonant background. The φ-dependence of H_{res} is plotted in Figure 5.2c (black circles). By fitting the data using Equation 2.20 (red solid line), and combined with data from the out-of-plane rotational scan (see Figure 5.6b), the magnetic anisotropy in this device is found to be[1]: $\mu_0 H_{2\perp} = -134$ mT, $\mu_0 H_{4\perp} = -80$ mT, $\mu_0 H_{2\|} = -189$ mT and $\mu_0 H_{4\|} = 72$ mT. Hence the nano-bar exhibits large in-plane uniaxial anisotropy, with its easy axis along the [110] direction, i.e. perpendicular to the long axis of the bar. Furthermore, since the saturation magnetisation in this material is $\mu_0 M_s = 50$ mT (measured by Arianna Casiraghi using SQUID), the large resonance field ($\mu_0 H_{\mathrm{res}} > 350$ mT) ensures that the $\mathbf{M}$ is always fully saturated along the direction of the applied field $\mathbf{H}_0$.

5.3.2 Mapping the magnetic anisotropy

The magnetic anisotropy in other 80 nm-wide bars patterned along different crystallographic orientations has also been investigated using CIT-FMR. The angular plots of H_{res} for [010] and [100] bars are presented in Figure 5.3a (blue and green circles respectively, in-plane scans). The plot reveals a dominant uniaxial anisotropy H_U generated by the patterned-induced strain-relaxation, with easy axis perpendicular to the bar orientation, on top of the intrinsic uniaxial ($H_{2\|}$) and biaxial ($H_{4\|}$) terms of the unpatterned film. The anisotropy profiles $H_{\mathrm{res}}(\varphi)$ can be well fitted using Equation 3.2 (solid lines in Figure 5.3a), and the deduced anisotropy constants H_i in the two devices are compared in Figure 5.3b. It demonstrates that H_U is nearly an order

[1]An iterative fitting method is adopted [74]: Firstly the in-plane $H_{\mathrm{res}}(\varphi)$ data are analysed and fitted to Equation 2.20 using $\gamma = 176$ GHz/T ($g = 2$). This gives approximate values of M_{eff}, $H_{4\|}$ and $H_{2\|}$, which are then used as starting parameters to carry out a weighted nonlinear least square fit to the $H_{\mathrm{res}}(\varphi)$ data from out-of-plane scans (as in Figure 5.6b), allowing the two parameters γ and $H_{4\perp}$ to vary. Using the γ value obtained by this procedure as the input parameter for the next iteration, new values of M_{eff}, $H_{4\|}$ and $H_{2\|}$ are obtained by fitting to the in-plane data. These two steps are repeated until optimal fitting is achieved and all five parameters (M_{eff} , $H_{4\perp}$, $H_{4\|}$, $H_{2\|}$, and γ) converge and remain unchanged in subsequent iterations.

	[100] bar	[010] bar	[110] bar	[1$\bar{1}$0] bar
$\mu_0 H_{4\parallel}$ (mT)	-68	-87	92	72
$\mu_0 H_{2\parallel}$ (mT)	58	30	286	-189
$\mu_0 H_U$ (mT)	250	-270	‡	‡

Table 5.1: In-plane anisotropy constants H_i in the 80 nm-wide bars patterned along different crystallographic orientations on (Ga,Mn)(As,P) epilayers. In the [110] and [1$\bar{1}$0] bars, H_U is collinear with $H_{2\parallel}$.

of magnitude stronger than the intrinsic anisotropy terms $H_{4\parallel}$ and $H_{2\parallel}$. By definition, $H_U > 0$ if its easy axis is along the [010] crystalline direction.

Figure 5.3c compares the anisotropy in all four 80 nm-wide bars (along [100], [110], [010] and [1$\bar{1}$0] crystalline axes), and the in-plane anisotropy constants H_i are summarised in Table 5.1. In very narrow bars, the growth-strain caused by lattice mismatch is fully relaxed, making H_U the dominant term [66]. This is demonstrated by the 80 nm-wide devices, all of which exhibit strong uniaxial anisotropy with easy axes always perpendicular to the corresponding bar orientations. In devices along the [110] and [1$\bar{1}$0] axes, the direction of H_U coincides with the intrinsic uniaxial anisotropy $H_{2\parallel}$, and it is therefore either enhanced or reduced by $H_{2\parallel}$.

5.3.3 Strain-relaxation in devices of different sizes

The magnetic anisotropy in samples of different sizes has been systematically investigated using the CIT-FMR technique. In Figure 5.4a–c, the anisotropy profiles in bars of widths 80, 500 and 4000 nm are compared (all devices are patterned along the [010] axis on the (Ga,$Mn_{0.06}$)(As,$P_{0.1}$) wafer). Recent numerical calculations show that the strain-relaxation is spatially nonuniform and takes place on a length scale of several hundred nanometres [26]. Therefore it is not surprising that the effect of strain-relaxation on the magnetic anisotropy becomes smaller with increasing bar width. Figure 5.4d compares the values of H_U among the three devices. In the 4 μm-wide bar, H_U is very

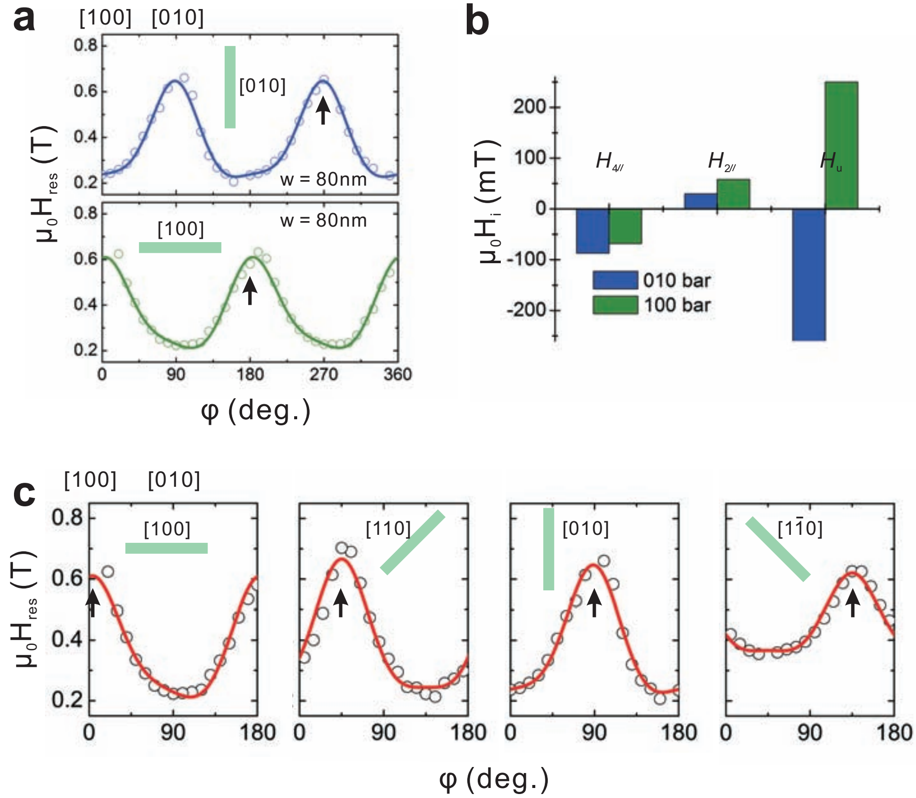

Figure 5.3: The magnetic anisotropy in 80 nm-wide (Ga,Mn)(As,P) bars measured using CIT-FMR. **a,** Polar plots for H_{res} measured in two 80 nm-wide devices patterned along the [010] and [100] axes (blue and green circles respectively). The orientations of the devices are shown in the inset, and are marked by black arrows in the main graphs. The solid lines are fits of Equation 3.2. **b,** The in-plane anisotropy constants $H_{4\|}$, $H_{2\|}$ and H_U for the two devices, deduced from fittings. **c,** The anisotropy profiles in all four 80 nm-wide bars, patterned along [100], [110], [010] and [1$\bar{1}$0] axes.

small (10 mT) and the device exhibits near bulk-like magnetic anisotropy (a superposition of twofold and fourfold symmetry due to $H_{2\|}$ and $H_{4\|}$).

The findings are quantitatively consistent with other published results performed on (Ga,Mn)As devices under compressive-strain, but also provide some new insights. For example, Hoffmann *et al.* have measured devices on a (Ga,Mn)As wafer with 6% Mn concentration (50 nm-thick film), and have observed $K_{\mathrm{U}} = 1.8 \times 10^4$ erg/cm^3 (equivalent to $\mu_0 H_U = 47.6$ mT) on a 400 nm-wide bar [67]; while the 500 nm-wide (Ga,Mn)(As,P) bar measured in this study reveals similar value with $\mu_0 H_U = -50$ mT[1]. For narrower bars (200 nm-wide), Hümpfner *et al.* and Wenisch *et al.* have shown that $\mu_0 H_U$ in (Ga,Mn)As devices with lower Mn concentrations (4% and 2.5% respectively) are a few tens of mT (25 and 45 mT respectively) [65, 66]; whereas this experiment has demonstrated that H_U can be further increased by making the bars even narrower ($\mu_0 H_U = -270$ mT in the 80 nm-wide bar shown in Figure 5.4d).

5.3.4 FMR signatures in devices of different sizes

CIT-FMR is also performed on each device using different excitation frequencies. As shown by Equation 3.5, ΔH (half width at half maximum) can be decomposed into a frequency-independent, inhomogeneously-broadened part ($\Delta H_{\mathrm{inhomo}}$) and a frequency-dependent, damping-related part ($\alpha\omega/\gamma$) [74]. In Figure 5.4f, the FMR linewidths in (Ga,Mn)(As,P) samples of different bar sizes are compared.

It is found that $\Delta H_{\mathrm{inhomo}}$ is smallest in the 80 nm-wide bar (2.5 mT), and largest in the 500 nm-wide bar (10 mT). Since $\Delta H_{\mathrm{inhomo}}$ is caused by strain gradients within the samples, it could indicate that the 80 nm-wide device has the least variation in internal strain, whereas the 500 nm-wide bar has the strongest. This is consistent with the magnetic anisotropy measured in these devices (Figure 5.4a–c). In addition, the Gilbert damping constant is observed to change inversely with sample width, from $\alpha = 0.023$ in the

[1]Note that the sign of H_U simply indicates the direction of its easy axis.

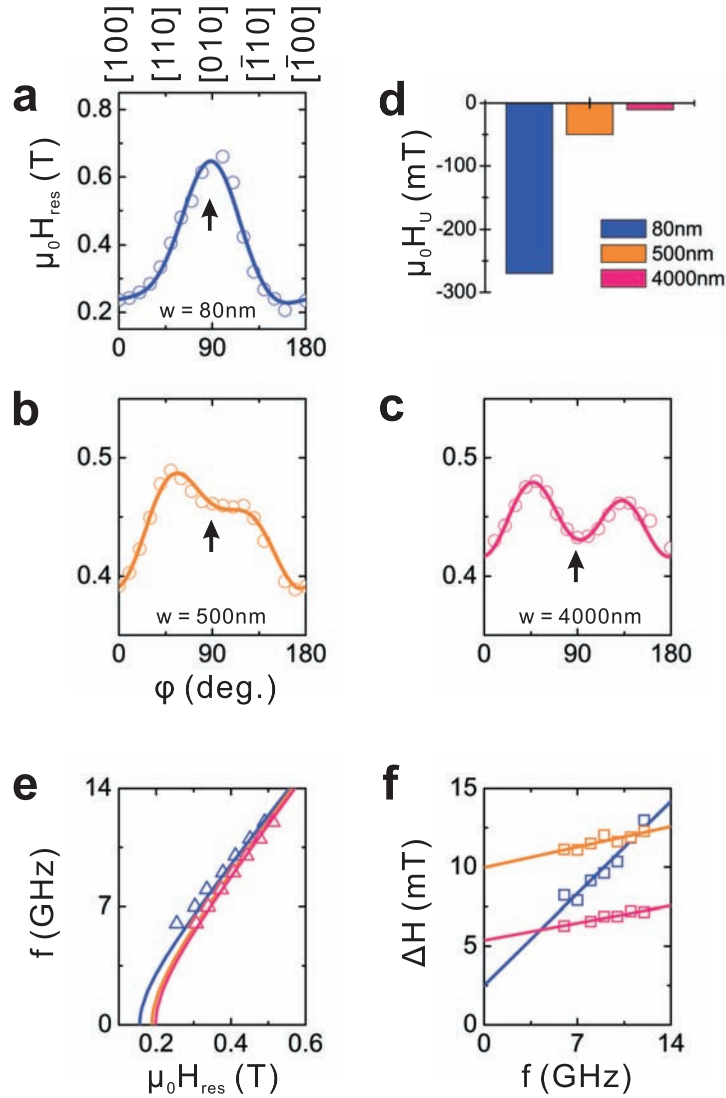

Figure 5.4: Evolution of the magnetic properties with device size. **a − c,** The resonance field $H_{\mathrm{res}}(\varphi)$ measured in three (Ga,Mn)(As,P) stripes with widths of 80, 500 and 4000 nm (length:width ratio = 10:1) respectively (all device are patterned along the [010] direction). The circles are measured data, and the solid lines are fittings. The black arrows mark the orientations of the bars. **d,** Comparison of the strain-relaxation-induced anisotropy H_U in the three devices. **e,** Frequency-dependence of the resonance field H_{res} measured in the three devices (triangles). The solid lines are fitted results to Equation 2.20. **f,** Frequency-dependence of the FMR linewidth ΔH (squares). The data are fitted to straight lines to calculate $\Delta H_{\mathrm{inhomo}}$ and α, see Equation 3.5.

80 nm-wide bar, to $\alpha = 0.005$ (500 nm-wide), and to $\alpha = 0.004$ (4000 nm-wide). This is possibly related to the quasiparticle lifetime becoming shorter in narrower samples due to increased scattering.

5.3.5 Effects of growth-strain on H_U

To further investigate the effect of the growth-induced strain on H_U, additional devices patterned from (Ga,Mn)(As,P) epilayers with 10% and 0% phosphorus are compared, which are under tensile- and compressive-strain respectively[1]. In particular, two 500 nm-wide bars are compared, both are fabricated along the [010] orientation.

Figure 5.5a shows the anisotropy profile measured on the (Ga,Mn)As micro-bar. It exhibits strong uniaxial anisotropy H_U due to lithography-induced strain-relaxation, with the easy axis coincide with the [010]-bar direction. This is in agreement with earlier studies on (Ga,Mn)As devices using SQUID, magnetotransport and FMR techniques [26, 65–67]. To the contrary, for H_U in the phosphorus-doped device patterned from tensile-strained (Ga,Mn)(As,P), the easy axis is aligned perpendicular to the direction of the bar (Figure 5.5b), consistent with observations on the 80 nm-wide bars reported earlier (Figure 5.3c). This is further illustrated in Figure 5.5c by comparing the in-plane anisotropy fields: The intrinsic magnetic anisotropy $H_{4\parallel}$ and $H_{2\parallel}$ are similar in magnitude between the two devices, and have the same sign; whereas the strain-relaxation-induced anisotropy H_U changes sign, indicating that the strain relaxes in the opposite sense between the two bars. This clearly establishes the reverse effect of growth-strain (compressive vs tensile) on the patterning-induced anisotropy H_U, as illustrated schematically in Figure 5.5d.

5.3.6 Lithography-control over the magnetisation

Finally, it is shown that the strong perpendicular anisotropy of the unpatterned (Ga,Mn)(As,P) epilayer (10% P) can be largely reduced by litho-

[1] The wafer with 0% P is the same 25 nm-thick ($Ga_{0.94}$,$Mn_{0.06}$)As film used in the previous two Chapters.

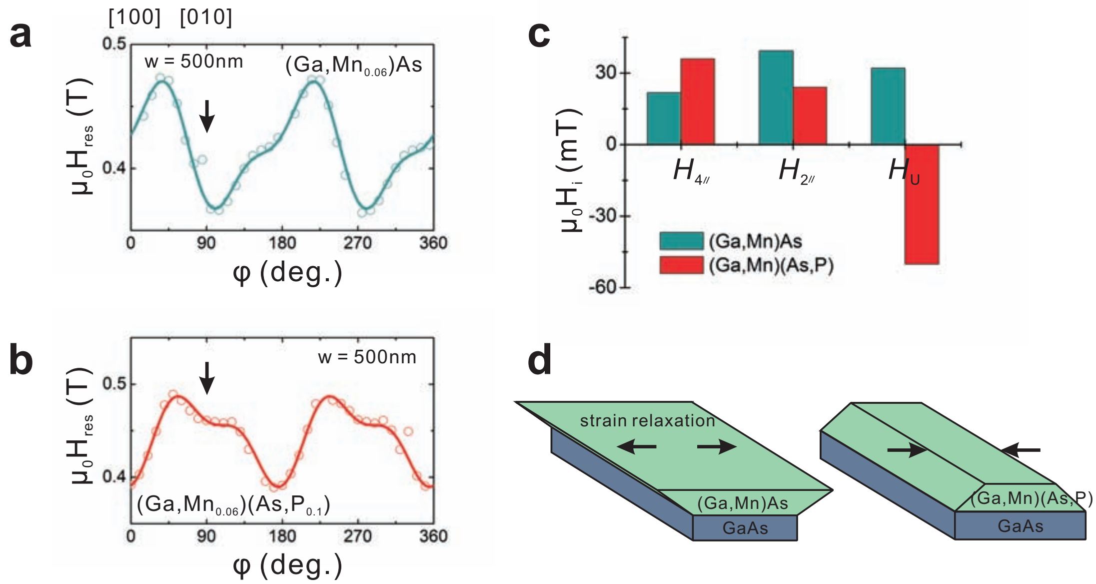

Figure 5.5: Comparison of H_U in the (Ga,Mn)As and (Ga,Mn)(As,P) devices (both are 500 nm-wide and patterned along the [010] direction). **a,** $H_{\mathrm{res}}(\varphi)$ measured from an in-plane rotational scan on the (Ga,Mn)As micro-bar. The circles are experimental data, and the solid line is the fitted results. **b,** $H_{\mathrm{res}}(\varphi)$ measured on the (Ga,Mn)(As,P) nanodevice. **c,** The in-plane magnetic anisotropy terms H_i in the two samples. **d,** Schematic of strain-relaxation in the (Ga,Mn)As and (Ga,Mn)(As,P) nanostructures.

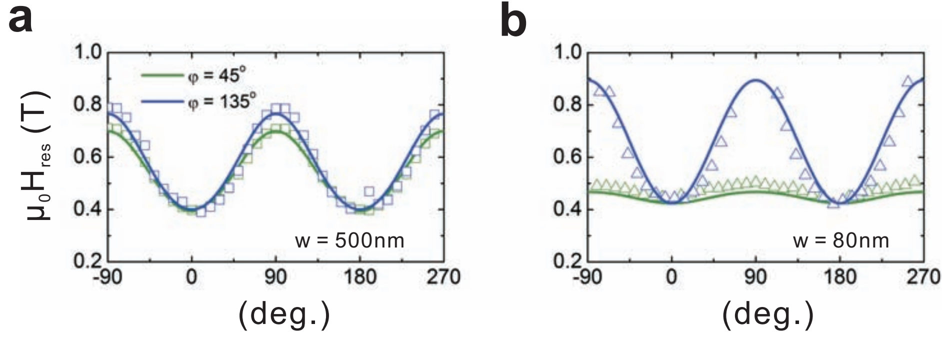

Figure 5.6: Out-of-plane rotational scans on (Ga,Mn)(As,P) devices patterned along the $[1\bar{1}0]$ direction. **a,** Rotational scans of θ on a 500 nm-wide bar at $\varphi = 45^{\circ}$ (green squares) and $\varphi = 135^{\circ}$ (blue squares). The solid lines are fitted results according to Equation 3.2. **b,** Same scans of θ on a 80 nm-wide bar.

graphic patterning, so that a second easy in-plane axis occurs in the 80 nm-wide bars. Figure 5.6 compares the results from out-of-plane rotational scans of $\mathbf{H}_0$ (i.e. rotating θ at fixed φ) in a 500 nm and a 80 nm-wide $[1\bar{1}0]$ bar respectively. Two scans are performed on each device: One is for comparing the magnetic anisotropy in the [110]–[001] plane (i.e. $\theta = 90^{\circ}$ and $\varphi = 45^{\circ}$, cf. Figure 5.2d), whereas the other scan allows comparison of the magnetic anisotropy in the $[1\bar{1}0]$–[001] plane ($\theta = 90^{\circ}$ and $\varphi = 135^{\circ}$). The magnetisation is driven at a microwave frequency of 17 GHz.

For the 500 nm-wide bar (Figure 5.6a), $H_{\mathrm{res}}(\theta)$ implies that both in-plane directions (in-plane easy and hard axes) are significantly harder than the perpendicular-to-plane direction, leading to an overall out-of-plane easy axis. This is consistent with the tensile-strained nature of the bulk $(Ga_{0.94},Mn_{0.06})(As_{0.9},P_{0.1})$ epilayer.

For the 80 nm-wide bar (Figure 5.6b), the global hard axis along the $[1\bar{1}0]$ orientation ($\theta = 90^{\circ}$, $\varphi = 135^{\circ}$) becomes harder compared to the wider 500 nm bar. The resonance field H_{res} along the [110] direction ($\theta = 90^{\circ}$, $\varphi = 45^{\circ}$), however, is now comparable to the field along [001], indicating that the [110] orientation becomes similarly easy as the perpendicular [001] orientation and only a weak uniaxial anisotropy in the [110]–[001] plane remains on top

of the intrinsic cubic anisotropy. This indicates that the strain-relaxation in the in-plane bar orientation is mostly relaxed as it is the case for the perpendicular [001]-direction.

5.4 Conclusions and outlook

To summarise, the strong spin-orbit coupling and exchange interaction in the diluted magnetic semiconductor (Ga,Mn)(As,P) enables the application of current-induced torque driven ferromagnetic resonance (CIT-FMR). Using this technique the magnetic anisotropy in individual micron- and nanoscale (Ga,Mn)(As,P) devices has been investigated, and the effects of strain-relaxation on the anisotropy in these samples have been examined.

It is important to point out the simplicity of the devices. The microwave magnetic field and the detection technique originate from the material properties, so only a 2-terminal nano-bar (a resistor) is required, enabling simple and rapid fabrication. The CIT-FMR technique is also applicable to other ferromagnetic material systems. Candidates include other magnetic semiconductors but also metal thin films in which the spin-orbit interaction has the potential to play a technological role. CoPt thin films are an important material for future study due to the recent observation of a strong current-induced field with Rashba symmetry [58].

5.5 Appendix – Magnetic anisotropy control with PMMA (preliminary results)

Introduction The magnetic anisotropy in (Ga,Mn)As and (Ga,Mn)(As,P) epilayers is directly linked to the strain on the materials, and it can be manipulated by either adding additional strain via a piezoelectric transducer [5–8], or by releasing the strain via lithographic processes (as demonstrated by the experiments in this Chapter). On the other hand, since the measurements are always performed at cryogenic temperatures, it is conceivable that if a material with a different thermal contraction coefficient is attached to the ferromagnetic device, strain is induced during cooling and possibly alter the magnetic anisotropy in the sample.

The initial experimental results on the manipulation of magnetic anisotropy in (Ga,Mn)(As,P) microstructures by thermal contraction are presented in this Section. The polymer PMMA[1] (polymethyl methacrylate) has been shown to possess large thermal expansion coefficient[2] and is therefore chosen for this experiment. It is applied by simply dropping on top of a sample and is then solidified in an oven at 80°C for 2 h. The device is then cooled down to 6 K and its magnetic properties are investigated using CIT-FMR.

A total number of 6 devices have been tested. 2 micro-bars broke during the cooling procedure[3], which demonstrates the strong thermal contraction of PMMA. Consistent observations have been made on the 4 devices that have survived the initial cooling process, and representative results from two samples are discussed. Their characteristics are listed in Table 5.2.

Ferromagnetic resonance curves Figure 5.7a shows a typical photovoltage spectrum measured across Device A by sweeping $\mathbf{H}_0$ at a fixed frequency of 10 GHz. Two peaks can be clearly observed. Fittings to Equation 2.25

[1] The PMMA used for the experiment is diluted with anisole to 6% concentration (A6) and has molecular weight of 950k.

[2] The linear thermal expansion coefficient of PMMA is measured to be 80×10^{-6} K^{-1} at 300 K [146], whereas for GaAs it is 5.8×10^{-6} K^{-1} at 300 K [147].

[3] Two of the working devices also broke when they were cooled down for a second time.

Device Name	Condition	Dimension
A ($\parallel$ [100])	Annealed	0.5 μm $\times$ 10 μm
B ($\parallel$ [010])	Annealed	4 μm $\times$ 40 μm

Table 5.2: The two $(Ga_{0.94},Mn_{0.06})(As_{0.9},P_{0.1})$ micro-bars discussed in this Section.

reveals that one peak centres at 760 mT with linewidth $\Delta H = 28$ mT, and in addition, there is a second, broader peak which centres at 450 mT with linewidth $\Delta H = 42$ mT.

Similar broad, low-field peaks have been previously reported in FMR experiments on bulk (Ga,Mn)As films, and are attributed to microwave magneto-conductivity changes in the sample [74]. In order to further investigate their properties, field sweeps at different microwave frequencies are performed, as shown in Figure 5.7b. The data reveal that the resonance positions H_{res} for the narrow peaks increase with increasing frequency, in agreement with the magnetic resonance condition (Equation 2.20). The broad peaks, on the other hand, shift to lower fields at higher excitation frequencies, which implies that their origins are not FMR-related (possibly due to Joule heating caused by the microwave current), and are not discussed in this Section.

Change in magnetic anisotropy The change in magnetic anisotropy due to the thermal contraction of PMMA is the focus of this study. Figure 5.8 compares measurement data from in-plane rotational scans on Device A with and without PMMA. With the PMMA coating, the φ-dependence of H_{res} displays a pronounced twofold symmetry, which clearly indicates strong uniaxial anisotropy with easy axis along the [100] direction, i.e. along the direction of the micro-bar (Figure 5.8a and 5.8b). This can be described by introducing the uniaxial anisotropy term H_U.

This is in stark contrast to the magnetic anisotropy of the device without the PMMA coating. As displayed in Figure 5.8c and 5.8d as well as in

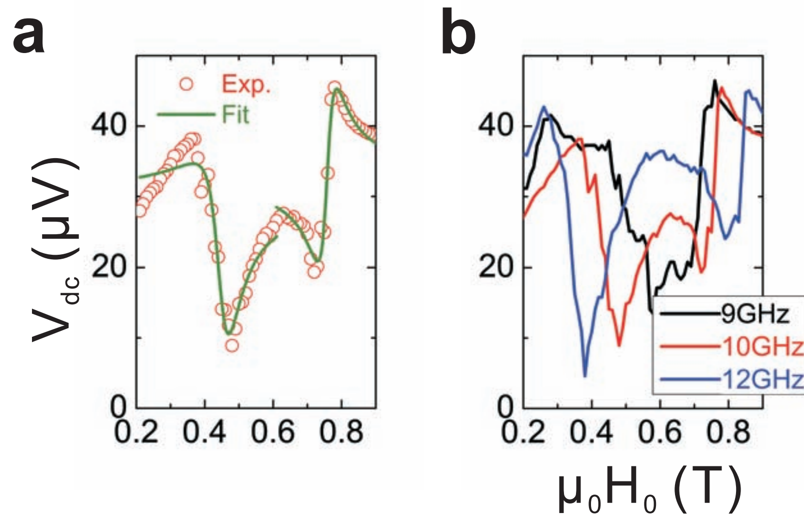

Figure 5.7: Ferromagnetic resonance signals on Device A with PMMA coating. **a,** The photovoltage measured using a 10 GHz current. The red circles are experimental data, and the green lines are fittings to individual peaks according to Equation 2.25. **b,** V_{dc} taken at different driving frequencies of 9, 10 and 12 GHz. The curves have been scaled for comparison.

the main Chapter, the additional uniaxial anisotropy H_U caused by strain-relaxation in this device has an easy axis perpendicular to the bar, i.e. in the [010] direction, due to the tensile-strain present in the (Ga,Mn)(As,P) epilayer.

With regard to the magnitude of H_U in the two conditions, Figure 5.8b implies that H_U becomes the dominant anisotropy term in the PMMA-coated device, similar to that observed in the 80 nm-wide bars (see Figure 5.2). Whereas Figure 5.8d shows a superposition of twofold and fourfold symmetry (due to H_U and $H_{4\parallel}$ respectively), which is consistent with observations made on other 500 nm-wide bars patterned on (Ga,Mn)(As,P) and also on (Ga,Mn)As epilayers (Figure 5.5). This immense difference in the magnitude of H_U is more established when the anisotropy constants are directly compared in Figure 5.8e: Under the strain induced by the thermal contraction of PMMA, $\mu_0 H_U$ is found to rise from 30 mT to −241 mT in Device A (note that the sign of $\mu_0 H_U$ represents the direction of its easy axis). The sign change in the biaxial anisotropy $H_{4\parallel}$ is possibly an artefact because the fitting procedure is not precise enough to reproduce the correct values of the biaxial anisotropy when the effective anisotropy is dominated strongly by the strain-induced uniaxial contribution.

The change in sign of H_U in nanoscale Device A suggests that the tensile-strain-relaxation of the uncovered device is compensated and superimposed by the strain executed by the PMMA when it is under thermal contraction, which has an apparent effect of elongating the lattice constant perpendicular to the bar. This process is illustrated schematically in Figure 5.8f.

Finally, the effect of PMMA contraction on the magnetic anisotropy in wider bars (Device B) is investigated. As Figure 5.9b shows, the magnetic anisotropy in the original device exhibits a superposition of twofold and fourfold symmetries, caused by the intrinsic biaxial and uniaxial anisotropy terms $H_{4\parallel}$ and $H_{2\parallel}$, and a small strain-relaxation-induced uniaxial term $\mu_0 H_U = -10.4$ mT. When PMMA is added, CIT-FMR measurements reveal that while the intrinsic terms stays relatively unchanged, the additional uniaxial anisotropy $\mu_0 H_U$ is reversed (33.5 mT) due to the strain generated by different thermal contractions of PMMA and (Ga,Mn)(As,P) (Figure 5.9a).

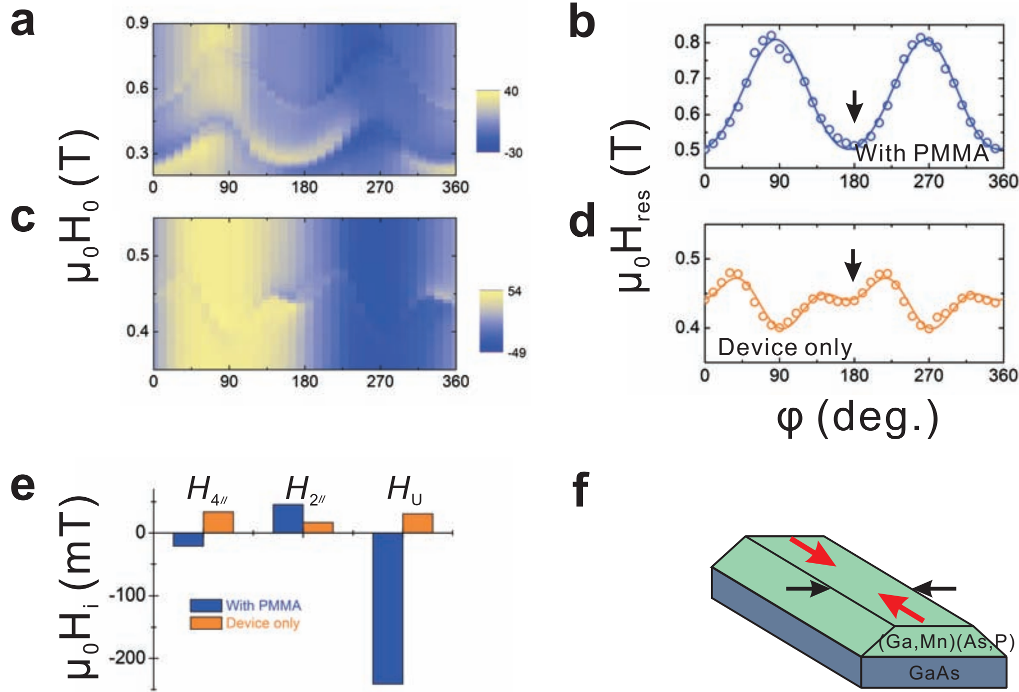

Figure 5.8: Comparison of the change in magnetic anisotropy in Device A before and after PMMA has been applied. **a,** Photovoltage spectra from in-plane rotational scans of $\mathbf{H}_0$ on the PMMA-coated device. A 10 GHz microwave current is used. Both the broad and narrow peaks are found to be φ-dependent. **b,** The resonance field H_{res} for the PMMA-coated device (blue circles), and the blue line is the fitted curve. The black arrow marks the direction of the micro-bar. **c – d,** Magnetic anisotropy profile on the same device before PMMA is applied (orange circles). **e,** Comparison of the in-plane anisotropy constants H_i in the two conditions. **f,** Schematic of the strain induced on the micro-bar due to the thermal contraction of PMMA. Black arrows: direction of strain-relaxation in patterned bars; red arrows: possible direction of strain applied by PMMA contraction.

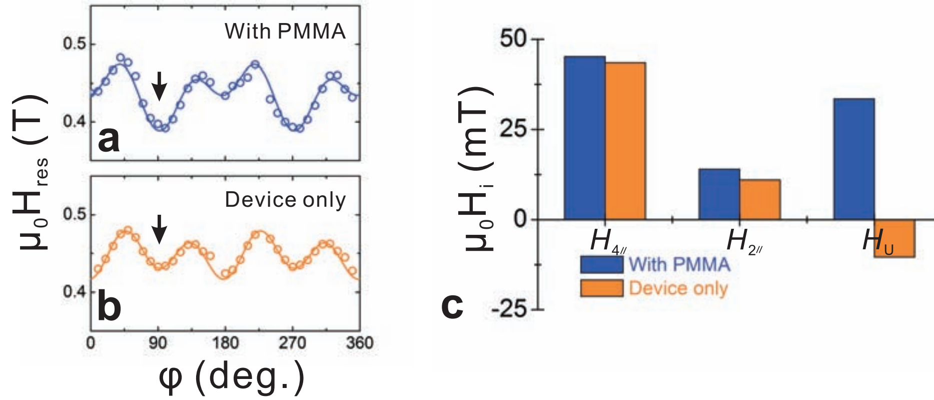

Figure 5.9: Comparison of the change in magnetic anisotropy of Device B with and without PMMA. **a,** The resonance field H_{res} for the PMMA-coated device (blue circles), detected using a 10 GHz current. The black arrow marks the direction of the micro-bar. **b,** The magnetic anisotropy profile on the same device before PMMA has been applied (orange circles). **c,** Comparison of the in-plane anisotropy fields H_i for Device B in the two conditions.

The deduced anisotropy fields H_i for Device B in the two conditions are compared in Figure 5.9c, where the sign change in H_U is easily visible. However, the size of H_U is much smaller in this sample than that in Device A.

An out-of-plane rotational scan carried out on Device B reveals that the sample still possesses an overall perpendicular-to-plane easy axis, hence the microdevice is still under tensile-strain. However, no FMR signal was observed when measuring the narrower Device A, therefore it is unclear at this stage whether the strain generated by the contraction of PMMA could lead to an additional in-plane easy axis in the narrow bars.

In order to understand the effect of PMMA contraction on the magnetic anisotropy, numerical simulations are needed to map the profile of the strain applied on the devices. This is however not straightforward for the current samples due to the non-uniformity of the PMMA coating. Future experiments on devices covered with lithographically-patterned PMMA layers should provide more insights into the polymer's role in defining the magnetic anisotropy.

Summary and outlook In this Section, preliminary results using an in-situ control of anisotropy method on (Ga,Mn)(As,P) micro-bars are presented. The large thermal expansion coefficient of the polymer PMMA has been employed to strain the ferromagnetic samples and hence alter their magnetic properties; and it has been established that this strain could lead to additional uniaxial anisotropy in the microdevices, which becomes dominant in nanometre-wide devices and overcomes the strain-relaxation-induced anisotropy in these samples.

However, in order to fully understand this effect, further experiments should be performed in the following areas:

- PMMA in this study has been applied onto the device rather arbitrarily, and the thickness of the polymer coating is unknown. Thus future experiments should be systematically carried out on samples with controlled parameters, such as using PMMA with different thickness, concentration and even molecular weight.

- Devices patterned on both (Ga,Mn)As and (Ga,Mn)(As,P) layers should be measured.

- More importantly, it has been observed both in (Ga,Mn)As and (Ga,Mn)(As,P) micro-bars that the current-induced torque due to the linear Dresselhaus spin-orbit coupling diminishes in smaller devices due to pattering-induced strain-relaxation (Section 4.3.4). Therefore it is also intriguing to investigate the impact on CIT when additional strain is introduced to the system via PMMA contraction. This could even lead to ferromagnetic microdevices with tunable spin-orbit interaction.

- Finally, other materials can also be used to generate strain on the ferromagnetic devices. Potential candidates include many metals, which have thermal expansion coefficients usually a few times that of GaAs. A sample with a thinned substrate can be glued on top of a metal sheet, and the difference in thermal contraction between GaAs and the metal during cooling can therefore generate strain on the ferromagnet.

The CIT-FMR method, established in this Thesis, provides a reliable platform for the magnetic anisotropy and spin-orbit coupling in individual ferromagnetic devices to be investigated.

Chapter 6

Closing remarks

The theoretical formulation of spin-transfer torque (STT) [17, 18], and subsequent experimental observations on its role in magnetisation reversal and magnetic dynamics [19], have allowed the magnetisation to be directly controlled by an electric current and opens a new range of applications, including magnetic memory devices and high-frequency oscillators. Spin-transfer torque occurs in non-collinear ferromagnetic systems with relatively complex device structures.

On the other hand, the current-induced torque (CIT) in uniform ferromagnets has so far only been observed in magnetisation reversal experiments [39, 58, 59]. The experiments described in this Thesis have expanded the understanding of CIT in magnetic semiconductors, including its role in magnetisation dynamics, its magnitude and orientation in diluted magnetic semiconductors (Ga,Mn)As and (Ga,Mn)(As,P), and its relation to internal and external parameters such as conductivity and strain. Furthermore, a new class of device-scale ferromagnetic resonance (FMR) technique is established, named CIT-FMR in this Thesis, which has the advantage of simple device structure and scalability, and can be transferred to characterise the magnetic properties and CIT in a wide range of ferromagnet systems.

Future experimental directions The CIT-FMR technique established in this Thesis has provided a platform for investigating both the current-induced torque (via vector magnetometry) and the magnetic anisotropy (via

ferromagnetic resonance) in individual submicron devices. The experiments in this Thesis have focused on the magnetic semiconductors (Ga,Mn)As and (Ga,Mn)(As,P), but this technique can be equally applied to study ferromagnetic metal thin films at room temperature, with candidates including Fe/GaAs and CoPt systems.

Since the linear Dresselhaus spin-orbit interaction is strain-related, a whole family of experimental investigations regarding the control of CIT via strain can be initiated. In (Ga,Mn)As systems, the effect of strain on the magnetic anisotropy has been extensively studied, using techniques such as lattice mismatch (by varying doping levels and impurity contents) [1, 77, 92, 95], mechanical stress (piezoelectric transducer) [5–8], and patterning-induced strain-relaxation [26, 65–67, 115]. In this Thesis, the first step towards understanding the impact of strain-relaxation on CIT has been reported; however, it will also be interesting to study the behaviour of CIT under the stress from a piezoelectric transducer. Being able to engineer the magnitude and orientation of CIT, both on magnetic semiconductors and ferromagnetic metals, could have important technological implications.

In addition, since structure inversion asymmetry (SIA) can give rise to Rashba spin-orbit coupling, it is interesting to examine the result of symmetry breaking caused by an external electric field in the crystal (e.g. via electrical gating). Previous experiments have focused on the changes in anisotropy by gating the magnetic semiconductor materials [10, 12], but it is of equal importance to investigate if CIT can be manipulated in such way.

A final class of experiments are related to magnetisation switching and thus the memory functionality of future spintronic devices. According to the LLG equation that governs the dynamics of magnetic motion, it is expected that a fast pulse $\mathbf{H}_{\text{pulse}}$ applied perpendicular to $\mathbf{M}$ could generate a torque $-\gamma(\mathbf{M} \times \mathbf{H}_{\text{pulse}})$ and induce magnetisation precession. Magnetisation switching caused by this precessional motion therefore promises high energy efficiency with ultrafast reversal time [148]. This "precessional switching" experiment has been performed on thin film metal systems using a real field pulse [148–154], but it would be equally interesting to apply this principle on magnetic semiconductors using CIT. Ultimately, the aim is to drive fast

precessional switching in magnetic metal films using CIT, and hence realise room-temperature, all-electrical magnetic memory units.

Appendix A

Derivation of the FMR lineshape

In this Section, the expressions for the FMR signal (Equations 2.25 – 2.29 in Section 2.4.3) is derived by solving the LLG equation (Equation 2.14) and considering the frequency mixing effect. The derivations are based on (Ga,Mn)As and (Ga,Mn)(As,P) epilayers, but can be extended to other ferromagnetic metal systems by using a different expression for the magnetic anisotropy[1].

The total voltage across a device is given by Ohm's law:

$$V(t) = I(t) \cdot R(t) \tag{A.1}$$

Here $I(t) = I\cos(\omega t)$ is the ac current within the sample, and $R(t)$ is the time-dependent longitudinal resistance.

According to Equation 2.6, the longitudinal resistance of the sample is given as:

$$R_{xx} = R_{\perp} - \Delta R \cos^2 \vartheta \tag{A.2}$$

where $R_{\perp}$ is the resistance when $\mathbf{M} \perp \mathbf{I}$, and $\Delta R > 0$ is the AMR coefficient ($\Delta R = R_{\perp} - R_{\parallel}$).

[1]The dominant magnetic anisotropy in ferromagnetic metal systems is the shape anisotropy, whereas in magnetic semiconductors such as (Ga,Mn)As and (Ga,Mn)(As,P), the magnetocrystalline anisotropy energies are more pronounced.

In FMR experiments, the magnetic moments precess under the driving torque of an ac magnetic field, resulting in a time-varying angle:

$$\vartheta(t) = \vartheta + \vartheta_c \cos(\omega t - \psi) \tag{A.3}$$

where ϑ_c describes the deviation of $\mathbf{M}$ from its axis of rotation (referred to as the "cone angle" of the precession), and ψ is the phase difference between the resistance and the ac current. An expression for the time-varying resistance $R(t)$ can thus be obtained by combing Equations A.2 and A.3. In the case of small cone angle precession, the expression can be simplified by expanding $\cos^2 \vartheta(t)$ up to first order:

$$R(t) \approx R_{\perp} - \Delta R \left[\cos^2 \vartheta - 2\vartheta_c \cos\vartheta \sin\vartheta \cos(\omega t - \psi)\right] \tag{A.4}$$

Combining Equations A.1 and A.4, it is found that the total voltage $V(t)$ comprises terms at frequencies ω and 2ω, and a time-independent (dc) term V_{dc}, which is the focus of this derivation.

To find out the expression for ϑ_c, the magnetisation components in the plane of rotation need to be determined. The geometry used for the FMR experiments is defined in Figure A.1. Since the applied magnetic field $\mathbf{H}_0$ is much larger than the anisotropy of the ferromagnet (measured to be a few tens of mT), the magnetisation vector $\mathbf{M}$ stays parallel to $\mathbf{H}_0$. A second coordinate system $x' - y'$ is defined with respect to $\mathbf{M}$. In this new system, $\mathbf{H}_0 = (H_0, 0, 0)$, and $\mathbf{M} = (M_s, m_{y'}e^{i\omega t}, m_z e^{i\omega t})$ in the case of small angle precession.

The dynamics of the damped magnetic motion is described phenomenologically by the Landau-Lifshitz-Gilbert (LLG) equation:

$$\frac{\partial \mathbf{M}}{\partial t} = -\gamma\mu_0 \mathbf{M} \times (\mathbf{H}_{\mathrm{eff}} + \mathbf{h}_{\mathrm{mw}}) + \frac{\alpha}{M_s}\left(\mathbf{M} \times \frac{\partial \mathbf{M}}{\partial t}\right) \tag{A.5}$$

here the first term is the field torque and the second term is the Gilbert damping. γ is the gyromagnetic ratio and α is the phenomenological Gilbert damping constant. $\mathbf{H}_{\mathrm{eff}}$ is the effective magnetic field in the vicinity of the magnetisation. It is a vector sum of the dc magnetic field $\mathbf{H}_0$, the demagnetisation field $\mathbf{H}_{\mathrm{demag}}$ and the anisotropy field of the material $\mathbf{H}_{\mathrm{ani}}$. $\mathbf{h}_{\mathrm{mw}}$ is

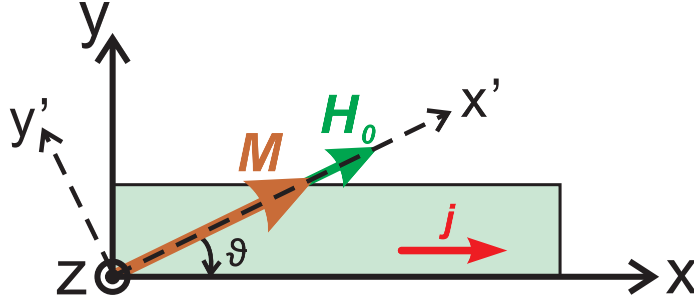

Figure A.1: The coordinate systems used in the derivation.

the microwave frequency magnetic field which drives the magnetic moments; in the $x' - y'$ system, it has the form:

$$\mathbf{h}_{\mathrm{mw}} = \begin{pmatrix} h_x \cos\vartheta - h_y \sin\vartheta \\ h_x \sin\vartheta + h_y \cos\vartheta \\ h_z \end{pmatrix} e^{i\omega t} \tag{A.6}$$

Solving Equation (A.5) and discarding high-order terms, the following set of linearised equations are obtained [68]:

$$\frac{i\omega}{\gamma} m_{y'} + \left(\frac{i\alpha\omega}{\gamma} + H_0 + H_1\right) m_z = M_s h_z \tag{A.7}$$

$$\left(\frac{i\alpha\omega}{\gamma} + H_0 + H_2\right) m_{y'} - \frac{i\omega}{\gamma} m_z = M_s (h_x \sin\vartheta + h_y \cos\vartheta) \tag{A.8}$$

where

$$H_1 = M_s - H_{2\perp} + H_{2\parallel} \cos^2\left(\varphi + \frac{\pi}{4}\right) + \frac{1}{4} H_{4\parallel}(3 + \cos 4\varphi) \tag{A.9}$$

$$H_2 = H_{4\parallel} \cos 4\varphi - H_{2\parallel} \sin 2\varphi \tag{A.10}$$

are terms containing the demagnetisation and anisotropy fields of the (Ga,Mn)As epilayers.

In (Ga,Mn)As films, due to the strong in-plane anisotropy, the precessional motion of the magnetisation is highly elliptical, with the maximum deviation from its equilibrium position occurring for **M** in-plane with the sample. For small angle precession, the maximum cone angle is $\vartheta_c = m_{y'}/M_s$.

Its value can be obtained by solving Equation (A.7) and (A.8):

$$\vartheta_c = -\frac{ih_z\gamma}{\omega} - \frac{[i(H_0+H_1)-\Delta H]\,[\gamma h_z(H_0+H_2+i\Delta H)-i\omega(h_x\sin\vartheta+h_y\cos\vartheta)]}{\omega\,[-(H_0+H_1+i\Delta H)(H_0+H_2+i\Delta H)+\omega^2/\gamma^2]} \tag{A.11}$$

Here $\Delta H = \alpha\omega/\gamma$ defines the resonance linewidth (half width at half maximum). The complex expression of Equation (A.11) arises from the complex susceptibility χ.

Combining Equation (A.1), (A.4) and (A.11), a general expression for the dc photovoltage is obtained:

$$V_{\mathrm{dc}} = -\frac{1}{2}I\Delta R\sin(2\vartheta)\left\{\frac{i\gamma h_z}{\omega} + \frac{1}{\omega\,[-(H_0+H_1+i\Delta H)(H_0+H_2+i\Delta H)+\omega^2/\gamma^2]}\Big[i(H_0+H_1)-\Delta H\Big]\Big[\gamma h_z(H_0+H_2+i\Delta H) - i\omega(h_x\sin\vartheta+h_y\cos\vartheta)\Big]\right\} \tag{A.12}$$

In conventional FMR experiments, the frequency of the driving field ω is kept constant, and the external field $\mathbf{H}_0$ is swept. To determine the lineshape of the photovoltage near resonance, consider the profile of V_{dc} at a small deviation δH from H_{res}, i.e.

$$\delta H = |H_0 - H_{\mathrm{res}}| \tag{A.13}$$

For uniform precession of $\mathbf{M}$ in a material with small damping ($\alpha \ll 1$), $\Delta H \ll H_{\mathrm{res}}$. Also since only small perturbations near the resonance is considered, $\delta H \ll H_{\mathrm{res}}$. Substituting Equation (A.13) into (A.12) and only keeping terms linear in δH and ΔH, the following simplified expression is obtained:

$$V_{\mathrm{dc}} = -\frac{1}{2}I\Delta R\sin(2\vartheta)\left\{\frac{i\gamma h_z}{\omega} - \frac{1}{\omega(2H_0+H_1+H_2)(\delta H+i\Delta H)}\Big[\omega(h_x\sin\vartheta+h_y\cos\vartheta)(\delta H+H_0+H_1+i\Delta H) + \gamma h_z\Big(i\delta H(2H_0+H_1+H_2)+i(H_0+H_1)(H_0+H_2) - \Delta H(2H_0+H_1+H_2)\Big)\Big]\right\} \tag{A.14}$$

The in-phase (real) component of V_{dc} has the form (keeping only terms linear in α):

$$\mathrm{Re}\{V_{\mathrm{dc}}\} = V_{\mathrm{sym}} \frac{\Delta H^2}{(H_0 - H_{\mathrm{res}})^2 + \Delta H^2} + V_{\mathrm{asy}} \frac{\Delta H (H_0 - \Delta H)}{(H_0 - H_{\mathrm{res}})^2 + \Delta H^2} \tag{A.15}$$

with angle-dependent amplitudes

$$V_{\mathrm{sym}}(\vartheta) = \frac{I \Delta R}{2} A_{\mathrm{sym}} \sin(2\vartheta) h_z \tag{A.16}$$

$$V_{\mathrm{asy}}(\vartheta) = \frac{I \Delta R}{2} A_{\mathrm{asy}} \sin(2\vartheta)(h_x \sin\vartheta + h_y \cos\vartheta) \tag{A.17}$$

The terms A_{sym} and A_{asy} are the scalar amplitudes of the magnetic susceptibility ($A_i = \chi_i / M_s$):

$$A_{\mathrm{sym}} = \frac{\gamma (H_{\mathrm{res}} + H_1)(H_{\mathrm{res}} + H_2)}{\omega \Delta H (2H_{\mathrm{res}} + H_1 + H_2)} \tag{A.18}$$

$$A_{\mathrm{asy}} = \frac{(H_{\mathrm{res}} + H_1)}{\Delta H (2H_{\mathrm{res}} + H_1 + H_2)} \tag{A.19}$$

It is noticed that the saturation magnetisation M_s does not enter the expression of V_{dc} explicitly. This is a major convenience as M_s cannot be directly deduced from FMR experiments (since M_s and $H_{2\perp}$ always appear together), and other measurements such as SQUID and VSM are required to determined its value. The terms A_{sym} and A_{asy} are also angle-dependent, as they depend on the magnetic anisotropy of the device.

On the other hand, the 90$^{\mathrm{o}}$ out-of-phase (imaginary) component of V_{dc} consists of two Lorentzian components with the following amplitudes:

$$V'_{\mathrm{sym}}(\vartheta) = -\frac{I \Delta R}{2} A_{\mathrm{asy}} \sin(2\vartheta)(h_x \sin\vartheta + h_y \cos\vartheta) \tag{A.20}$$

$$V'_{\mathrm{asy}}(\vartheta) = \frac{I \Delta R}{2} A_{\mathrm{sym}} \sin(2\vartheta) h_z \tag{A.21}$$

This implies that if there is any phase difference ψ between the current and the oscillating resistance, the angular dependence of V_{asy} is partially mapped onto V_{sym} and vice versa. This is demonstrated in Section 4.5.1.

Appendix B

Measurement apparatus

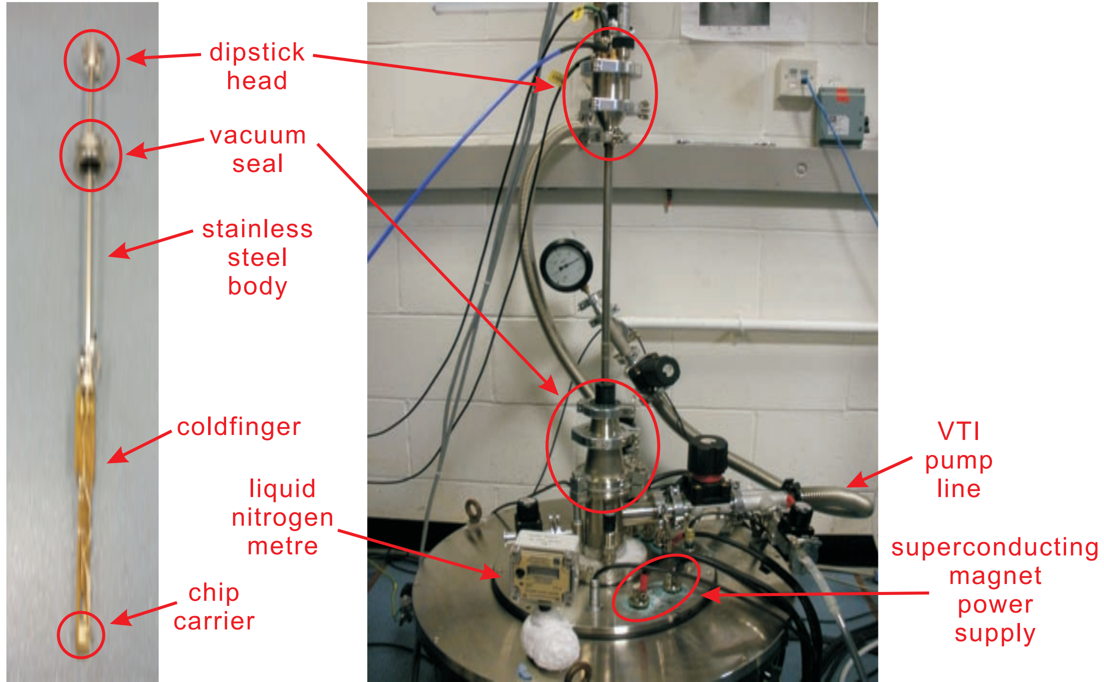

Figure B.1: **Left:** The dipstick used in the FMR experiments. The dc wires (copper and constantan, both purchased from *CMR-Direct*) and coaxial cables (purchased from *Oxford Instruments*) go through the hollow stainless steel body of the dipstick, and connect to the sample carrier (custom made by *PCB Train*, see also Figure 3.2a) which is loaded at the end of the coldfinger (made with oxygen-free copper by the *Cavendish Workshop*). **Right:** The dipstick when loaded into the variable-temperature cryostat (manufactured by *Cryogenics Limited*).

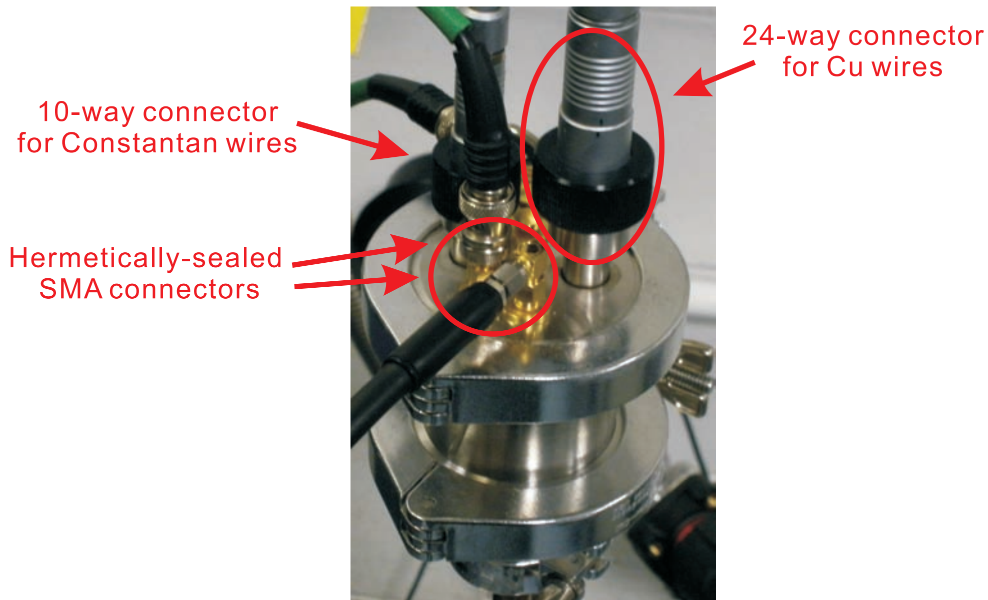

Figure B.2: An enlarged photo of the top of the dipstick. It consists of a NW-50 flange and various vacuum components (all purchased from *Nor-Cal Products, Inc.*). The flange hosts one 24-way dc connector which links the copper wires, and serves to power any electronic component installed on the coldfinger, such as radio-frequency couplers, amplifier, temperature sensors (purchased from *Lakeshore Cryotronics*) and Hall sensors (also from *Lakeshore Cryotronics*). There is also a 10-way dc connectors linking the constantan wires, and it allows measurement of the photovoltage (both connectors are purchased from *Oxford Instruments*). Besides the dc connectors, the flange also hosts 3 hermetically-sealed SMA connectors (purchased from *CMR-Direct*).

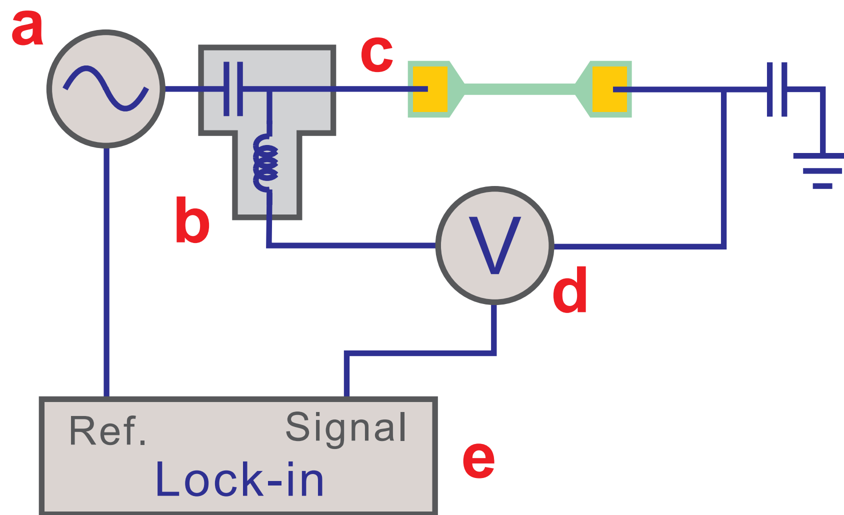

Figure B.3: The apparatus used in the FMR experiments. **a,** Signal generator (2 → 20 GHz) from *Anritsu*, model MG3692A. **b,** High-frequency bias-tee (0.1 → 40 GHz) from *Anritsu*, model K250. **c,** High-frequency flexible coaxial cable (0 → 18 GHz) from *Mini-Circuits*, model CBL3SMQ-SM+. **d,** Low-noise preamplifier from *Stanford Research Systems*, model SR560. **e,** Lock-in amplifier from *Stanford Research Systems*, model SR830.

Appendix C

Lithography recipes for the fabrication of microdevices

Design 1 – Devices with on-chip waveguide

Wafer cleansing: First with acetone for 5 min, then with IPA for 5 min (applying ultrasound in both steps)

Mesa

- Spinning of resist: PMMA (A6, 950mw) for 1 min at 4000 rpm
- Pre-bake for 90 s at 180°C on a thermal hot plate
- E-beam exposure: 650 C/cm^2
- Resist development: 50 s at 20°C in diluted MIBK solution (MIBK:IPA = 1:3)
- Rinse in IPA and blow dry with N_2 gas
- Oxygen plasma for 30 s
- Reactive ion etching: mixture of $SiCl_4$ and Ar gas for 140 s (etch rate: $\sim$ 10 nm/min for $(Ga_{0.88},Mn_{0.12})As$)

Metal contacts and waveguide

- Spinning of resist: PMMA (A6, 950mw) for 1 min at 4000 rpm
- Pre-bake for 90 s at 180°C on a thermal hot plate
- E-beam exposure: 650 C/cm^2
- Resist development: 50 s at 20°C in diluted MIBK solution (MIBK:IPA = 1:3)
- Rinse in IPA and blow dry with N_2 gas
- Prepare for evaporation: Oxygen plasma for 30 s, wash in diluted HCl solution (HCl(32%):H_2O = 1:10) for 30 s, rinse in DI water
- Evaporation: Cr: 20 nm at 4.2 Å/s, Au: 200 nm at 2.2 Å/s
- Lift-off: 2 h in acetone. Once successful, rinse in IPA and blow dry with N_2 gas

Design 2 – CIT-FMR devices

Wafer cleansing: First with acetone for 5 min, then with IPA for 5 min (applying ultrasound in both steps)

Mesa

- Spinning of resist: PMMA (A6, 950mw) for 1 min at 4000 rpm
- Pre-bake for 90 s at 180°C on a thermal hot plate
- E-beam exposure: 650 C/cm^2
- Resist development: 50 s at 20°C in diluted MIBK solution (MIBK:IPA = 1:3)
- Rinse in IPA and blow dry with N_2 gas
- Oxygen plasma for 30 s
- Reactive ion etching: mixture of $SiCl_4$ and Ar gas for 140 s (etch rate: $\sim$ 10 nm/min for $(Ga_{0.88},Mn_{0.12})As$)

Metal contacts

- Spinning of resist: UV-III for 30 s at 5000 rpm
- Pre-bake for 60 s at 155°C on a thermal hot plate
- UV exposure for 120 s
- Post-bake for 60 s at 155°C on a thermal hot plate
- Resist development: 30 s at 20°C in CD-26 developer
- Rinse in DI water and blow dry with N_2 gas
- Prepare for evaporation: Oxygen plasma for 30 s, wash in diluted HCl solution (HCl(32%):H_2O = 1:10) for 30 s, rinse in DI water
- Evaporation: Cr: 20 nm at 4.2 Å/s, Au: 200 nm at 2.2 Å/s
- Lift-off: 2 h in acetone. Once successful, rinse in IPA and blow dry with N_2 gas

References

[1] H. Ohno, *Science* **281**, 951 (1998). 1, 2, 3, 11, 13, 17, 19, 129

[2] S. A. Wolf, *et al.*, *Science* **294**, 1488 (2001). 1

[3] A. Haury, *et al.*, *Phys. Rev. Lett.* **79** (1997). 3

[4] H. Ohno, *et al.*, *Appl. Phys. Lett.* **69**, 363 (1996). 3

[5] A. W. Rushforth, *et al.*, *Phys. Rev. B* **78**, 085314 (2008). 3, 20, 107, 120, 129

[6] S. T. B. Goennenwein, *et al.*, *Phys. Status Solidi (RRL)* **2**, 96 (2008).

[7] C. Bihler, *et al.*, *Phys. Rev. B* **78**, 045203 (2008). 20, 21

[8] M. Overby, A. Chernyshova, L. P. Rokhinson, X. Liu, J. K. Furdyna, *Appl. Phys. Lett.* **92**, 192501 (2008). 3, 20, 107, 120, 129

[9] D. Chiba, F. Matsukura, H. Ohno, *Appl. Phys. Lett.* **89**, 162505 (2006). 3, 21, 106, 107

[10] D. Chiba, *et al.*, *Nature* **455**, 515 (2008). 21, 27, 55, 104, 105, 106, 129

[11] K. Olejník, *et al.*, *Phys. Rev. B* **78**, 054403 (2008). 14, 21

[12] M. H. S. Owen, *et al.*, *New J. Phys.* **11**, 023008 (2009). 3, 21, 104, 106, 107, 129

[13] J. Qi, *et al.*, *Appl. Phys. Lett.* **91**, 112506 (2007). 3

[14] E. Rozkotová, *et al.*, *Appl. Phys. Lett.* **93**, 232505 (2008).

[15] E. Rozkotová, *et al.*, *Appl. Phys. Lett.* **92**, 122507 (2008).

[16] E. Rozkotová, *et al.*, *IEEE Trans. Magn.* **44**, 2674 (2008). 3

[17] J. C. Slonczewski, *J. Magn. Magn. Mater.* **159**, L1 (1996). 4, 65, 128

[18] L. Berger, *Phys. Rev. B* **54**, 9353 (1996). 128

[19] D. Ralph, M. Stiles, *J. Magn. Magn. Mater.* **320**, 1190 (2008). 4, 65, 128

[20] E. B. Myers, D. C. Ralph, J. A. Katine, R. N. Louie, R. A. Buhrman, *Science* **285**, 867 (1999). 4

[21] F. J. Albert, J. A. Katine, R. A. Buhrman, D. C. Ralph, *Appl. Phys. Lett.* **77**, 3809 (2000).

[22] J. A. Katine, F. J. Albert, R. A. Buhrman, E. B. Myers, D. C. Ralph, *Phys. Rev. Lett.* **84**, 3149 (2000).

[23] S. I. Kiselev, *et al.*, *Nature* **425**, 380 (2003). 4, 8, 80

[24] M. Yamanouchi, D. Chiba, F. Matsukura, H. Ohno, *Nature* **428**, 539 (2004). 4, 106

[25] M. Yamanouchi, *et al.*, *Science* **317**, 1726 (2007).

[26] J. Wunderlich, *et al.*, *Phys. Rev. B* **76**, 054424 (2007). 9, 10, 11, 23, 56, 71, 75, 95, 107, 112, 116, 129

[27] M. Hayashi, *et al.*, *Phys. Rev. Lett.* **98**, 037204 (2007). 4

[28] J. Åkerman, *Science* **308**, 508 (2005). 4

[29] Y. Huai, *AAPPS Bulletin* **18**, 33 (2008). 4

[30] M. Hayashi, L. Thomas, R. Moriya, C. Rettner, S. S. P. Parkin, *Science* **320**, 209 (2008). 4

[31] S. S. P. Parkin, M. Hayashi, L. Thomas, *Science* **320**, 190 (2008). 4

[32] S. I. Kiselev, *et al.*, *Phys. Rev. B* **72**, 064430 (2005). 4, 8, 80

[33] J. C. Sankey, *et al.*, *Phys. Rev. B* **72**, 224427 (2005). 4, 80

[34] A. A. Tulapurkar, *et al.*, *Nature* **438**, 339 (2005). 4, 9, 10, 35, 36, 80, 85

[35] J. C. Sankey, *et al.*, *Phys. Rev. Lett.* **96**, 227601 (2006). 4, 8, 9, 35, 36, 37, 80, 85

[36] J. C. Sankey, Microwave-frequency characterization of spin transfer and individual nanomagnets, Ph.D. thesis, Cornell University (2007). 5, 85

[37] A. Manchon, S. Zhang, *Phys. Rev. B* **78**, 212405 (2008). 4

[38] A. Manchon, S. Zhang, *Phys. Rev. B* **79**, 094422 (2009). 38, 66

[39] A. Chernyshov, *et al.*, *Nature Phys.* **5**, 656 (2009). 7, 8, 38, 74, 128

[40] I. Garate, A. H. MacDonald, *Phys. Rev. B* **88**, 134403 (2009). 4, 66, 74, 76

[41] Y. K. Kato, R. C. Myers, A. C. Gossard, D. D. Awschalom, *Phys. Rev. Lett.* **93**, 176601 (2004). 6

[42] A. Y. Silov, *et al.*, *Appl. Phys. Lett.* **85**, 5929 (2004). 66

[43] V. Sih, *et al.*, *Nature Phys.* **1**, 31 (2005). 6

[44] G. Dresselhaus, *Phys. Rev.* **100**, 580 (1955). 6, 39, 73

[45] Y. A. Bychkov, E. I. Rashba, *J. Phys. C: Solid State Phys.* **17**, 6039 (1984). 6, 40, 73

[46] M. I. Dyakonov, V. I. Perel, *Phys. Lett. A* **35**, 459 (1971). 6

[47] S. Gopalan, J. K. Furdyna, S. Rodriguez, *Phys. Rev. B* **32**, 903 (1985).

[48] G. C. La Rocca, N. Kim, S. Rodriguez, *Phys. Rev. B* **38**, 7595 (1988). 39, 40

[49] J. Inoue, G. E. W. Bauer, L. W. Molenkamp, *Phys. Rev. B* **67**, 033104 (2003). 6, 66

[50] Y. K. Kato, D. D. Awschalom, *J. Phys. Soc. Jpn.* **77**, 031006 (2008). 6, 8, 38, 39, 40, 75

[51] Z. Wilamowski, W. Jantsch, H. Malissa, U. Rössler, *Phys. Rev. B* **66**, 195315 (2002).

[52] G. Salis, *et al.*, *Physica E* **16**, 99 (2003).

[53] Y. Kato, R. C. Myers, A. C. Gossard, D. D. Awschalom, *Nature* **427**, 50 (2004).

[54] L. Meier, *et al.*, *Nature Phys.* **3**, 650 (2007). 6, 8, 41

[55] Y. K. Kato, R. C. Myers, A. C. Gossard, D. D. Awschalom, *Appl. Phys. Lett.* **87**, 022503 (2005). 6

[56] B. M. Norman, *et al.*, *Phys. Rev. B* **82**, 081304(R) (2010). 6

[57] Z. Wilamowski, H. Malissa, F. Schäffler, W. Jantsch, *Phys. Rev. Lett.* **98**, 187203 (2007). 6, 82

[58] I. M. Miron, *et al.*, *Nature Mater.* **9**, 230 (2010). 6, 7, 119, 128

[59] U. H. Pi, *et al.*, *Appl. Phys. Lett.* **97**, 162507 (2010). 6, 7, 128

[60] A. D. Caviglia, *et al.*, *Phys. Rev. Lett.* **104**, 126803 (2010). 6

[61] T. Jungwirth, J. Sinova, J. Mašek, J. Kučera, A. H. MacDonald, *Rev. Mod. Phys.* **78**, 809 (2006). 7, 13, 14, 74, 76

[62] J. N. Kupferschmidt, S. Adam, P. W. Brouwer, *Phys. Rev. B* **74**, 134416 (2006). 8

[63] J. C. Sankey, *et al.*, *Nature Phys.* **4**, 67 (2008). 8, 9, 10, 80, 85

[64] M. Endo, F. Matsukura, H. Ohno, *Appl. Phys. Lett.* **97**, 222501 (2010). 8

[65] S. Hümpfner, *et al.*, *Appl. Phys. Lett.* **90**, 102102 (2007). 9, 10, 11, 23, 55, 56, 62, 64, 71, 95, 107, 114, 116, 129

[66] J. Wenisch, *et al.*, *Phys. Rev. Lett.* **99**, 077201 (2007). 10, 23, 62, 112, 114

[67] F. Hoffmann, *et al.*, *Phys. Rev. B* **80**, 054417 (2009). 9, 10, 11, 23, 33, 35, 42, 56, 62, 64, 71, 95, 107, 114, 116, 129

[68] B. Heinrich, J. F. Cochran, *Adv. Phys.* **42**, 523 (1993). 9, 133

[69] M. Farle, *Rep. Prog. Phys.* **61**, 755 (1998). 34

[70] J. A. C. Bland, B. Heinrich, *Ultrathin Magnetic Structures* (Springer), iii edn. 9

[71] M. Rubinstein, *et al.*, *J. Magn. Magn. Mater.* **250**, 164 (2002). 9, 42

[72] Y. Sasaki, *et al.*, *J. Appl. Phys.* **91**, 7484 (2002).

[73] X. Liu, Y. Sasaki, J. K. Furdyna, *Phys. Rev. B* **67**, 205204 (2003). 34, 58, 98

[74] X. Liu, J. K. Furdyna, *J. Phys.: Cond. Matt.* **18**, R245 (2006). 33, 34, 53, 55, 58, 91, 98, 99, 111, 114, 121

[75] C. Bihler, *et al.*, *Appl. Phys. Lett.* **89**, 012507 (2006).

[76] K. Khazen, *et al.*, *Phys. Rev. B* **77**, 165204 (2008). 42, 59

[77] M. Cubukcu, *et al.*, *Phys. Rev. B* **81**, 041202(R) (2010). 9, 10, 19, 75, 76, 106, 107, 129

[78] K. Khazen, Ferromagnetic resonance investigation of GaMnAs nanometric layers, Ph.D. thesis, Université Paris VI C Pierre et Marie Curie (2008). 9, 35, 85

[79] S. T. B. Goennenwein, *et al.*, *Appl. Phys. Lett.* **90**, 162507 (2007). 9, 10, 35, 36

[80] N. Mecking, Y. S. Gui, C.-M. Hu, *Phys. Rev. B* **76**, 224430 (2007). 9, 52, 82, 85

[81] X. Hui, *et al.*, *Appl. Phys. Lett.* **93**, 232502 (2008). 10, 35, 36, 85

[82] L. H. Bai, *et al.*, *Appl. Phys. Lett.* **92**, 032504 (2008). 9

[83] M. V. Costache, S. M. Watts, M. Sladkov, C. H. van der Wal, B. J. van Wees, *Appl. Phys. Lett.* **89**, 232115 (2006). 9, 10, 35, 36, 42, 52, 85

[84] M. V. Costache, M. Sladkov, C. H. van der Wal, B. J. van Wees, *Appl. Phys. Lett.* **89**, 192506 (2006). 10, 42, 82

[85] Y. S. Gui, N. Mecking, A. Wirthmann, L. H. Bai, C.-M. Hu, *Appl. Phys. Lett.* **91**, 082503 (2007). 50, 82

[86] A. Yamaguchi, *et al.*, *Phys. Rev. B* **78**, 104401 (2008).

[87] A. Wirthmann, *et al.*, *Appl. Phys. Lett.* **92**, 232106 (2008). 9, 10, 35, 36, 53

[88] G. Boero, *et al.*, *Appl. Phys. Lett.* **87**, 152503 (2005). 10, 35

[89] I. Lee, *et al.*, *Nature* **466**, 845 (2010). 10

[90] P. R. Stone, J. W. Beeman, K. M. Yu, O. D. Dubon, *Physics B* **401** (2007). 10, 106

[91] P. R. Stone, *et al.*, *Phys. Rev. Lett.* **101**, 087203 (2008).

[92] A. W. Rushforth, *et al.*, *J. Appl. Phys.* **104**, 073908 (2008). 16, 17, 19, 76, 107, 108, 129

[93] A. Lemaître, *et al.*, *Appl. Phys. Lett.* **93**, 021123 (2008).

[94] A. Casiraghi, *et al.*, *Appl. Phys. Lett.* **97**, 122504 (2010). 10, 19, 107

[95] A. Shen, *et al.*, *J. Cryst. Growth* **175–176**, 1069 (1997). 11, 12, 19, 75, 106, 129

[96] H. Ohno, *J. Magn. Magn. Mater.* **200**, 110 (1999). 13

[97] A. V. Esch, *et al.*, *Phys. Rev. B* **56**, 13103 (1997). 14

[98] T. Hayashi, Y. Hashimoto, S. Katsumoto, Y. Iye, *Appl. Phys. Lett.* **78**, 1691 (2001). 14

[99] S. J. Potashnik, *et al.*, *Appl. Phys. Lett.* **79**, 1495 (2001). 15

[100] S. J. Potashnik, *et al.*, *Phys. Rev. B* **66**, 012408 (2002). 14, 15

[101] M. Wang, *et al.*, *Appl. Phys. Lett.* **93**, 132103 (2008). 14

[102] V. Novák, *et al.*, *Phys. Rev. Lett.* **101**, 077201 (2008). 15, 92

[103] R. C. O'Handley, *Modern Magnetic Materials* (John Wiley & Sons, Inc., 2000). 17, 18

[104] M. T. Johnson, P. J. H. Bloemen, F. J. A. den Broeder, J. J. de Vries, *Rep. Prog. Phys.* **59**, 1409 (1996). 17

[105] S. Blundell, *Magnetism in Condensed Matter* (Oxford University Press, 2001). 18

[106] W. Scholz, Micromagnetic simulation of thermally activated switching in fine particles, Ph.D. thesis, Technischen Universität Wien (1999). 18

[107] C. Gould, K. Pappert, G. Schmidt, L. W. Molenkamp, *Advanced Materials* **19**, 323 (2007). 19, 29, 30

[108] K. Pappert, *et al.*, *Appl. Phys. Lett.* **90**, 062109 (2007). 19

[109] K.-Y. Wang, *et al.*, *Phys. Rev. Lett.* **95**, 217204 (2005). 19

[110] M. Sawicki, *et al.*, *Phys. Rev. B* **71**, 121302(R) (2005). 20, 55, 75, 99

[111] U. Welp, V. K. Vlasko-Vlasov, X. Liu, J. K. Furdyna, T. Wojtowicz, *Phys. Rev. Lett.* **90**, 167206 (2003). 20

[112] H. Ohno, *et al.*, *Nature* **408**, 944 (2000). 21, 22

[113] E. D. Ranieri, Strain-induced effects on the magnetotransport properties of GaMnAs diluted magnetic semiconductors, Ph.D. thesis, University of Cambridge (2009). 21

[114] D. Chiba, M. Yamanouchi, F. M. H. Ohno, *Science* **301**, 943 (2003). 21

[115] J. Zemen, J. Kučera, K. Olejník, T. Jungwirth, *Phys. Rev. B* **80**, 155203 (2009). 23, 75, 76, 80, 95, 129

[116] K. Y. Wang, *et al.*, *Phys. Rev. B* **72**, 085201 (2005). 25, 26, 27

[117] F. Matsukura, M. Sawicki, T. Dietl, D. Chiba, H. Ohno, *Physica E: Low-dimensional Systems and Nanostructures* **21**, 1032 (2004). 25, 29

[118] H. X. Tang, R. K. Kawakami, D. D. Awschalom, M. L. Roukes, *Phys. Rev. Lett.* **90**, 107201 (2003). 25, 27, 28

[119] T. Jungwirth, M. Abolfath, J. Sinova, J. Kučera, A. H. MacDonald, *Appl. Phys. Lett.* **81**, 4029 (2002). 25

[120] A. Rushforth, *et al.*, *Phys. Rev. Lett.* **99**, 147207 (2007). 25, 27

[121] A. Rushforth, *et al.*, *J. Magn. Magn. Mater.* **321**, 1001 (2009). 27

[122] E. D. Ranieri, *et al.*, *New J. Phys.* **10**, 065003 (2008). 27

[123] F. Matsukura, H. Ohno, A. Shen, Y. Sugawara, *Phys. Rev. B* **57**, 2037 (1998). 29

[124] T. L. Gilbert, *IEEE Trans. Magn.* **40**, 3443 (2004). 32

[125] J. Smit, H. G. Beljers, *Phillips Research Reports* **10**, 113 (1955). 34

[126] H. Suhl, *Phys. Rev.* **97**, 555 (1955). 34

[127] R. Moriya, *et al.*, *Nature Phys.* **4**, 368 (2008). 36

[128] F. G. Pikus, G. E. Pikus, *Phys. Rev. B* **51**, 16928 (1995). 40

[129] G. L. Bir, G. E. Pikus, *Symmetry and strain-induced effects in semiconductors* (Wiley in New York, 1974). 40, 74

[130] Y. Kato, Ph.D. thesis, University of California, Santa Barbara (2005). 40

[131] R. N. Simons, *Coplanar Waveguide Circuits, Components and Systems* (John Wiley & Sons, Inc., 2001). 43

[132] J. Sinova, *et al.*, *Phys. Rev. B* **69**, 085209 (2004). 53, 69

[133] Y. Tserkovnyak, G. A. Fiete, B. I. Halperin, *Appl. Phys. Lett.* **84**, 5234 (2004). 53, 69

[134] V. Edelstein, *Solid State Commun.* **73**, 233 (1990). 66

[135] M. Silver, W. Batty, A. Ghiti, E. P. O'Reilly, *Phys. Rev. B* **46**, 6781 (1992). 74, 75

[136] J. M. Luttinger, W. Kohn, *Phys. Rev.* **97**, 869 (1955). 74

[137] I. Vurgaftman, J. R. Meyer, L. R. Ram-Mohan, *J. Appl. Phys.* **89**, 5815 (2001). 75

[138] I. Kuryliszyn-Kudelska, *et al.*, *J. Appl. Phys.* **95**, 603 (2004). 99

[139] I. Stolichnov, *et al.*, *Nature Mater.* **7**, 464 (2008). 104

[140] P. Chow, Investigation of magnetic anisotropy in (Ga,Mn)As microstructure using spin-orbit interaction, Master's thesis, University of Cambridge (2010). 105

[141] T. Dietl, H. Ohno, F. Matsukura, *Phys. Rev. B* **63**, 195205 (2001). 106

[142] D. Chiba, M. Yamanouchi, F. Matsukura, T. Dietl, H. Ohno, *Phys. Rev. Lett.* **96**, 096602 (2006). 106

[143] M. Yamanouchi, D. Chiba, F. Matsukura, T. Dietl, H. Ohno, *Phys. Rev. Lett.* **96**, 096601 (2006). 106

[144] K. Y. Wang, *et al.*, *J. Appl. Phys.* **101**, 106101 (2007). 107

[145] A. Dourlat, *et al.*, *J. Appl. Phys.* **102**, 023913 (2007). 107

[146] K. G. Lyon, G. L. Salinger, C. A. Swenson, *Phys. Rev. B* **19**, 4231 (1979). 120

[147] T. Soma, J. Satoh, H. Matsuo, *Solid State Commun.* **42**, 889 (1982). 120

[148] H. W. Schumacher, *et al.*, *Phys. Rev. Lett.* **90**, 017201 (2003). 129

[149] C. H. Back, *et al.*, *Phys. Rev. Lett.* **81**, 3251 (1998).

[150] C. H. Back, *et al.*, *Science* **285**, 864 (1999).

[151] M. Bauer, J. Fassbender, B. Hillebrands, R. L. Stamps, *Phys. Rev. B* **61**, 3410 (2000).

[152] Y. Acremann, C. H. Back, M. Buess, D. Pescia, V. Pokrovsky, *Appl. Phys. Lett.* **79**, 2228 (2001).

[153] T. Gerrits, H. A. M. van den Berg, J. Hohlfeld, L. Bär, T. Rasing, *Nature* **418**, 509 (2002).

[154] G. Woltersdorf, C. H. Back, *Phys. Rev. Lett.* **99**, 227207 (2007). 129